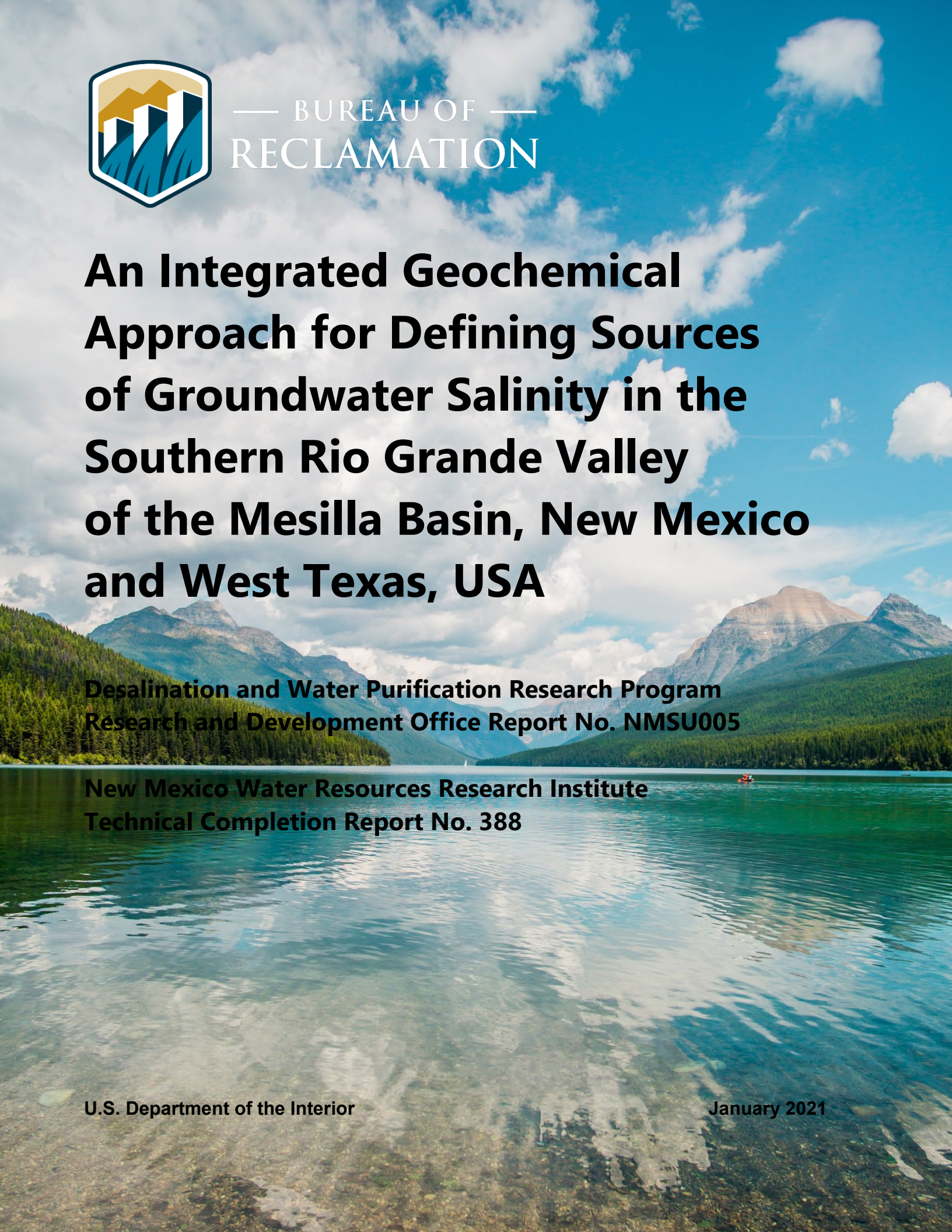

BUREAU OF RECLAMATION

An Integrated Geochemical Approach for Defining Sources of Groundwater Salinity in the Southern Rio Grande Valley of the Mesilla Basin, New Mexico and West Texas, USA

Desalination and Water Purification Research Program
Research and Development Office Report No. NMSU005

New Mexico Water Resources Research Institute
Technical Completion Report No. 388

U.S. Department of the Interior **January 2021**

REPORT DOCUMENTATION PAGE			Form Approved OMB No. 0704-0188
The public reporting burden for this collection of information is estimated to average 1 hour per response, including the time for reviewing instructions, searching existing data sources, gathering and maintaining the data needed, and completing and reviewing the collection of information. Send comments regarding this burden estimate or any other aspect of this collection of information, including suggestions for reducing the burden, to Department of Defense, Washington Headquarters Services, Directorate for Information Operations and Reports (0704-0188), 1215 Jefferson Davis Highway, Suite 1204, Arlington, VA 22202-4302. Respondents should be aware that notwithstanding any other provision of law, no person shall be subject to any penalty for failing to comply with a collection of information if it does not display a currently valid OMB control number. PLEASE DO NOT RETURN YOUR FORM TO THE ABOVE ADDRESS.			
1. REPORT DATE *(DD-MM-YYYY)* January 2021	2. REPORT TYPE Final		3. DATES COVERED *(From - To)* May 2017 – December 2019
4. TITLE AND SUBTITLE An Integrated Geochemical Approach for Defining Sources of Groundwater Salinity in the Southern Rio Grande Valley of the Mesilla Basin, New Mexico and West Texas, USA			5a. CONTRACT NUMBER Agreement No. R16AC00002 5b. GRANT NUMBER 5c. PROGRAM ELEMENT NUMBER
6. AUTHOR(S) Christopher Kubicki Kenneth C. Carroll James C. Witcher Andrew Robertson			5d. PROJECT NUMBER 5e. TASK NUMBER 5f. WORK UNIT NUMBER
7. PERFORMING ORGANIZATION NAME(S) AND ADDRESS(ES) New Mexico State University PO Box 30003, MSC 3Q, Skeen N336 Las Cruces, NM 88003-8003			8. PERFORMING ORGANIZATION REPORT NUMBER
9. SPONSORING/MONITORING AGENCY NAME(S) AND ADDRESS(ES) Bureau of Reclamation U.S. Department of the Interior Denver Federal Center PO Box 25007, Denver, CO 80225-0007			10. SPONSOR/MONITOR'S ACRONYM(S) Reclamation 11. SPONSOR/MONITOR'S REPORT NUMBER(S) DWPR Report No. NMSU005
12. DISTRIBUTION/AVAILABILITY STATEMENT Available from https://www.usbr.gov/research/dwpr/DWPR_Reports.html			
13. SUPPLEMENTARY NOTES			
14. ABSTRACT A significantly elevated groundwater salinity zone was identified in the southern part of the Mesilla Valley. This investigation characterized the occurrence, spatial extent, and source of the plume of elevated groundwater salinity using a wide range of geochemical and geophysical data and methods.			
15. SUBJECT TERMS Age Dating, Aqueous Geochemistry, Argon Isotope, Evaporite Minerals, Groundwater, Krypton Isotope, Mesilla Basin, Recharge, Rio Grande, Rio Grande Rift, Salinity, Sulfur Isotopes, Temperature Logs, Water Isotopes			
16. SECURITY CLASSIFICATION OF:		17. LIMITATION OF ABSTRACT	18. NUMBER OF PAGES 19a. NAME OF RESPONSIBLE PERSON Katherine (Katie) Guerra
a. REPORT U	b. ABSTRACT U	THIS PAGE U	19b. TELEPHONE NUMBER *(Include area code)* 303-445-2013

Standard Form 298 (Rev. 8/98)
Prescribed by ANSI Std. Z39.18

Desalination and Water Purification Research Program
Report No. NMSU005

New Mexico Water Resources Research Institute
Technical Completion Report No. 388

An Integrated Geochemical Approach for Defining Sources of Groundwater Salinity in the Southern Rio Grande Valley of the Mesilla Basin, New Mexico and West Texas, USA

Prepared for the Bureau of Reclamation Under Agreement No. R16AC00002

by

Christopher Kubicki, New Mexico State University
Kenneth C. Carroll, New Mexico State University
James C. Witcher, Witcher and Associates, Inc.
Andrew Robertson, U.S. Geological Survey

New Mexico State University
Las Cruces, New Mexico

Mission Statements

The Department of the Interior (DOI) conserves and manages the Nation's natural resources and cultural heritage for the benefit and enjoyment of the American people, provides scientific and other information about natural resources and natural hazards to address societal challenges and create opportunities for the American people, and honors the Nation's trust responsibilities or special commitments to American Indians, Alaska Natives, and affiliated island communities to help them prosper.

The mission of the Bureau of Reclamation is to manage, develop, and protect water and related resources in an environmentally and economically sound manner in the interest of the American public.

Disclaimer

The views, analysis, recommendations, and conclusions in this report do not represent official or unofficial policies or opinions of the Bureau of Reclamation but do represent the views of the U.S. Geological Survey. Mention of trade names or commercial products does not constitute their endorsement by the United States Government.

Acknowledgments

The Desalination and Water Purification Research and Development Program, Bureau of Reclamation, sponsored this research from a cooperative agreement between the Bureau of Reclamation (BOR) and New Mexico State University (#R16AC00002, Center for the Development and Use of Alternative Water Supplies).

We appreciate additional support through the U.S.-Mexico Transboundary Aquifer Assessment Act (Public Law 109-448). Support through isotopic analysis from the University of Bern is also greatly appreciated. We also thank Elephant Butte Irrigation District, Public Service Company of New Mexico (PNM), and Las Cruces Utilities for well access. We would also like to thank Shari Kelley, Frank Ramos, Virgil Lueth, Laura Crossey, Jeffrey Pepin, Barbara Hunter, and John Hawley for their contributions.

Acronyms and Abbreviations

ATTA	Atom Trap Trace Analysis
BLS	Below Land Surface (elevation)
DOI	Department of the Interior
GMWL	Global Meteoric Water Line
IBWC	International Boundary and Water Commission
ICP-OES	Inductively Coupled Plasma-Optical Emission Spectrometer
ILR	Isometric Log Ratio
INEGI	Instituto Nacional de Estadística y Geografía
JMASCJ	Ciudad Juárez Junta Municipal de Agua y Saneamiento
LLC	Low-level counting
μ^-	Muon
$\nu\mu$	Muon neutrino
NM WRRI	New Mexico Water Resources Research Institute
pMc	Percent modern carbon
SI	Saturation indices
TDS	Total dissolved solids
TU	Tritium units
USGS	U.S. Geological Survey
VCDT	Vienna Cañon Diablo Troilite
XRD	X-ray diffraction
Ar	Argon
^{39}Ar	Argon-39 is a radioisotope of argon
$BaSO_4$	Barium sulfate
^{14}C	Carbon-14 or radiocarbon, is a radioactive isotope of carbon
Ca^{2+}	Calcium
$CaCO_3$	Calcite
$CaSO_4$	Gypsum
CH_4	Methane
Cl^-	Chloride
$\delta^{13}C$	Ratio of stable isotopes ^{13}C: ^{12}C, reported in parts per thousand (per mil, ‰)
δD	Ratio of deuterium (or hydrogen-2, ^2H, D) and ^1H
$\delta^{18}O$	Ratio of stable isotopes oxygen-18 (^{18}O) and oxygen-16 (^{16}O)
$\delta^{34}S$	Ratio of two stable isotopes of sulfur, ^{34}S:^{32}S
^3H	Tritium or hydrogen-3 is radioactive isotope of hydrogen
HCO_3^-	Bicarbonate
H_2SO_4	Sulfuric acid
^3He	Helium-3 is a light, stable isotope of helium
^4He	Helium-4 is a stable isotope of helium
K^+	Potassium
Kr	Krypton
^{81}Kr	Krypton-81 is a radioisotope of krypton
^{85}Kr	Krypton-85 is a radioisotope of krypton
Mg^{2+}	Magnesium
Na^+	Sodium

NaCl	Halite
Ne	Neon
R	$^{3}He/^{4}He$ signature of groundwater
Ra	$^{3}He/^{4}He$ fraction of the atmosphere
SiO_2	Silica dioxide
SO_4^{2-}	Sulfate
Th	Thorium
U	Uranium
Xe	Xenon

Measurements

°C	Degree Celsius
m	Meter
m^2	Square meter
mg/L	Milligrams per liter
m/day	Meter per day
µS/cm	Microsiemens/centimeter
µg/L	Micrograms per liter
°	Angle (degrees)
‰	Per mil
ccSTP/g(H2O)	Gas cubic centimeter at standard temperature and pressure dissolved in 1g liquid water
µS/cm	Microsiemens per centimeter
pMC	Percent modern carbon (or pM as percent modern)
pCi/L	Picocuries per liter
dpm/ccKr	Number of ^{85}Kr decays per minute per mL (STP) of Kr gas
ccSTP/g(H2O)	Cubic centimeters standard temperature and pressure per gram

Metric Conversions

Unit	**Metric equivalent**
1 gallon	3.785 liters
1 gallon per minute	3.785 liters per minute
1 gallon per square foot of membrane area per day	40.74 liters per square meter per day
1 inch	2.54 centimeters
1 million gallons per day	3,785 cubic meters per day
1 pound per square inch	6.895 kilopascals
1 square foot	0.093 square meters
°F (temperature measurement)	(°F–32) × 0.556 = °C
1 °F (temperature change or difference)	0.556 °C

Contents

Figures

Tables

Executive Summary

Salinization of aquifers in arid regions is a growing issue due to increased water use as a result of population growth and increasing agricultural demands (Szynkiewicz et al., 2011). Spatial variability in sources of groundwater salinity may exist due to stratigraphic, geochemical, and hydrologic processes even in an integrated and relatively homogeneous aquifer system. For this reason, methods are needed to determine salinity sources, groundwater flow, and transport of salts in alluvial/fluvial groundwater basins.

Geochemical tracers analyzed from groundwater samples were used to determine the sources of salt contributing to groundwater salinity in the Mesilla Valley of the Mesilla basin located in southern New Mexico and west Texas. Results from southern Mesilla Valley groundwaters show a localized area, plume, of saline groundwater (10,000 to 29,700 mg/L total dissolved solids) near Sunland Park, New Mexico.

Results from this work help to construct a conceptual model of groundwater flow and the source of salinity in the Mesilla basin. Analysis of $\delta^{18}O$ and δD isotopes from groundwater samples support previous research that effectively shows groundwater in the Mesilla Valley has been recharged primarily from the Rio Grande. North of Sunland Park, New Mexico, lower groundwater salinity is associated with a spatial transition from sedimentary to volcanic rock underlying the alluvial aquifer, increasing alluvial sediment thickness, and $\delta^{34}S$ signatures of groundwater (+2.28 to +5.76‰), indicating a sulfate source that could not originate from Paleozoic bedrock. These results indicate a reduced influence of upward groundwater flow from sedimentary bedrock and increased dilution of brackish groundwater within the lower salinity alluvial aquifer in the central and northern Mesilla Valley.

Results for major ion analysis indicate a general shift from HCO_3^- recharge waters in the northern Mesilla Valley groundwater toward Cl^- and SO_4^{2-} waters in the southern Mesilla Valley. The transition in water types occurs from north to south and along the groundwater flow path, indicating increased influence from halite and gypsum dissolution and/or cation exchange in southern groundwaters. Evidence presented herein shows that groundwater salinity in the Mesilla Valley is increasingly derived from evaporite mineral dissolution and/or cation exchange as water flows southward. The $\delta^{34}S$ signatures of groundwater from the southern Mesilla Valley within the area of high salinity (+12.36 to +12.46‰) are comparable to $\delta^{34}S$ signatures of Upper Paleozoic gypsum (+12.5‰), indicating prolonged contact between groundwater and underlying Paleozoic bedrock. Greater than atmospheric concentrations of ^{39}Ar (132 to 134% pM) and high ^{4}He (10-6 to 10-7 ccSTP/g(H_2O) in groundwater samples collected from the plume confirm a substantial fraction of the groundwater is old (>1,000 years). This study illustrates how nested well clusters and geochemical tracers can be used to identify salinity sources and processes in geochemical investigations.

1. Introduction

Salinization of aquifers in arid regions is a growing issue due to increased water use as a result of population growth and increasing agricultural demands (Szynkiewicz et al., 2011). Studies of salinization typically address the location of high salinity areas, changes in salinity through time and space, and the sources of salinity identified using isotopic and geochemical tracers (Moyer et al., 2013). Increasing salinity is generally attributed to solute additions from anthropogenic or lithologic sources and/or evaporative processes in arid environments (Hogan et al., 2007). While temporal increases in groundwater salinity are easily observable, characterizing the sources of salinity and the spatial distribution of such sources across an aquifer system proves more difficult (Szynkiewicz et al., 2015; Teeple, 2017). Issues arise due to: (1) data gaps caused by the irregular distribution of wells tapping into an aquifer and (2) difficulty discerning among the sources of groundwater salinity, which often have similar geochemical signatures (Land, 2016; Witcher et al., 2004). Geophysical approaches, which attempt to map salinity in groundwater with electrical resistivity or electro-magnetic methods in areas where groundwater data are unavailable, often fail to differentiate between high salinity groundwater and high electrical conductivity subsurface materials such as clay and evaporites (Teeple, 2017), or may be unsuitable due to electrical interference in highly developed urban areas. Uncertainty over groundwater salinity sources, the distribution of salt in groundwater, and groundwater flow/transfer processes can complicate mitigation efforts to prevent continued salinization of useable and available groundwater and surface water (CH2MHill, 2013). In addition, mixing among groundwater, geothermal waters, and surface water, can lead to further uncertainty when attempting to quantify the sources of salt in groundwater (Hogan et al., 2007; Moyer et al., 2013; Szynkiewicz et al., 2011; Witcher et al., 2004).

Commonly, lithological chemical analysis is not done in conjunction with geochemical investigations of groundwater (e.g., Hiebing et al., 2018; King and Hawley, 1975; King et al., 1971; Leggat et al., 1962; Teeple, 2017; Williams et al., 2013; 2015; Wilson et al., 1981). As a result, the mass transfer of salt between lithology and groundwater is poorly defined. Assumptions regarding groundwater-rock interactions tend to dictate conclusions regarding dissolution of minerals, mixing, and groundwater flow paths of high salinity groundwater. In order to properly assess and possibly minimize further salinization of valuable arid water resources and to validate groundwater salinization processes, the characterization of salt in groundwater and lithology is necessary.

In this investigation the sources of salinity and mixing of groundwaters in the Mesilla Valley (Fig. 1), New Mexico, were determined by evaluating the $\delta^{34}S$ isotopes, major cation and anion data, and stable hydrogen and oxygen isotope data for water ($\delta^{18}O$, δD) in groundwater samples. In addition, an analysis for $\delta^{34}S$ isotopes from various rock formations, x-ray diffraction (XRD) of well cuttings, and previously published research on the Mesilla basin stratigraphy were used to formulate a more comprehensive understanding of the relation between salt dissolution and groundwater flow. Plausible dissolution scenarios between salinity sources and groundwater were evaluated using age-dating isotopes (^{85}Kr, ^{81}Kr, ^{39}Ar, ^{3}H, ^{3}He, ^{4}He, and ^{14}C), geochemical modeling, and temperature logs.

2. Problem

Anomalously high-salinity groundwaters have been identified near Paso del Norte at the southern end of the Mesilla Valley (CH2MHill, 2013; Teeple, 2017; Fig. 1). Most wells in the southern Mesilla Valley are completed within the shallow alluvial aquifer, resulting in data gaps throughout the deeper components of the groundwater flow system (Land, 2016). Consequently, the source(s), flow path(s), and mixing relationships of high-salinity groundwater near the Paso del Norte is not well understood. Recharge to and from the Rio Grande has resulted in additional uncertainty when assessing flow paths and sources of these high salinity groundwaters. Data from a series of wells constructed in a north to south orientation in the Mesilla Valley allow for the documentation and evaluation of water quality, flow path(s), and source(s) of salinity of waters located beneath the Rio Grande. This data set has provided a unique opportunity to document groundwater salinization processes near the Rio Grande in the Mesilla basin from north to south along the primary flow direction.

3. Previous Studies

Sources of groundwater salinity in the southern Mesilla Valley have been examined using geochemical tracers (CH2MHill, 2013; Hiebing et al., 2018; Szynkiewicz et al., 2011; Teeple, 2017; Witcher et al., 2004) and geophysics (Teeple, 2017). Major salinity sources have been attributed to irrigation (Sheng, 2013), evaporite mineral dissolution in the lower and middle Santa Fe Group (Hiebing et al., 2018), and shallow evaporite brines (Szynkiewicz et al., 2015). Others have suggested that topographically driven groundwater flow, a concept originally described by Toth (1963), is responsible for the higher salinity groundwater located near the Paso del Norte (Hawley and Kennedy, 2004; Hogan et al., 2007; Moore et al., 2007; Phillips et al., 2003; Witcher et al., 2004). In this hypothesis, deep regional groundwater flow sweeps up or accumulates ions and increases in temperature along its flow path until it is forced into the shallow Rio Grande fluvial aquifer at the topographically lowest point. An additional source of salinity in this hypothesis, is inputs from outflow of structurally controlled geothermal systems that provide recharge to Mesilla basin groundwater (Witcher et al., 2004). The Paso del Norte area has been reported to be a discharge location for groundwater in the Mesilla basin alluvial aquifer (Hawley and Kennedy, 2004; Teeple, 2017; Witcher et al., 2004). Topographically driven groundwater flow has also been shown to be representative of groundwater flow in other Rio Grande Rift basins where terminal bedrock constrictions force deep groundwater upward toward the surface and the Rio Grande (Phillips et al., 2003; Moore et al., 2008; Williams et al., 2013). Previous research is unclear as to whether fluid migration through rift-bounding faults (Williams et al., 2013) or basin aquifers dominate the salinity input process (Phillips et al., 2003). Tracers commonly utilized for groundwater age dating (tritium (half-life of 12.3 years; Clark and Fritz, 1997) and carbon-14 [^{14}C] (half-life of 5,568 years; Plummer and others, 1994)) within the Mesilla basin have been unable to characterize flow paths due to short half-lives (tritium) or the dissolution of carbonates that can alter the ^{14}C concentrations (^{14}C; Teeple, 2017).

Noble gas radioisotopes can provide complementary chronometric and geochemical source and mixing information to groundwater investigations (Yokochi et al., 2013). Because noble gases are inert, corrections for geochemical processes are generally not necessary (Clark and Fritz, 1997). The low abundance and solubility of the radioisotopes of krypton and argon have required impractical sampling volumes in the past. However, with the advent of low-level analysis techniques such as Atom Trap Trace Analysis (ATTA; Chen et al., 1999) and Low-Level Counting (LLC; Oeschger and Wahlen, 1975), the noble gas isotopes krypton-81 (^{81}Kr (half-life of 229,000 years)), krypton-85 (^{85}Kr (half-life of 10.8 years)), and argon-39 (^{39}Ar (half-life of 269 years)) (Yokochi et al., 2013) have become practical tracers for age-dating groundwater. The isotope ^{39}Ar is particularly valuable, as the argon system is the only isotopic system that will effectively bridge the groundwater-age gap in the very important intermediate range of 50 to 1,000 years. Additionally, approaches such as the use of sulfur isotopes for distinguishing between anthropogenic and geological sources of SO_4^{2-} have been effective in identifying sources of salt in other geochemical investigations (Szynkiewcz et al., 2011; Miao et al., 2013). SO_4^{2-} is a major contributor of salt from both geological sources (e.g., gypsum ($CaSO_4$)) and fertilizers (e.g., H_2SO_4) found in irrigation waters (Szynkiewcz et al., 2011). To supplement aqueous geochemical data, we compared previously collected stable sulfate isotopes ($^{34}S/^{32}S$) of dissolved sulfate collected in 2007 by Szynkiewcz and others (2011) to $\delta^{34}S$ of gypsum samples collected in this study.

4. Geologic and Hydrogeologic Setting

This investigation defined regions or portions of the Mesilla Valley for comparison of groundwater chemistry characteristics, and groundwater wells within these regions were segregated into north, central, and southern region groups. North wells are located within the Mesilla Valley north of Vado, New Mexico. Central wells are located in the Mesilla Valley between Anthony, New Mexico and Vado, New Mexico. Wells located to the south of Anthony, New Mexico, in the Mesilla Valley are identified as southern wells. Wells located outside the Mesilla Valley are labeled according to their geographical location (Fig. 1). For example, the Afton Power Plant well is located on the West Mesa of the Mesilla basin, and Well 68 is located in the Jornada del Muerto basin (Fig. 1). Additional references are made to the ISC-4 plume, an area of high salinity groundwater around the ISC-4 well cluster near the Paso del Norte. References to the "alluvial aquifer" are used for the Santa Fe Group aquifer system and inset Rio Grande fluvial aquifer within the Mesilla Valley when discussing both aquifers as a composite or single integrated aquifer system.

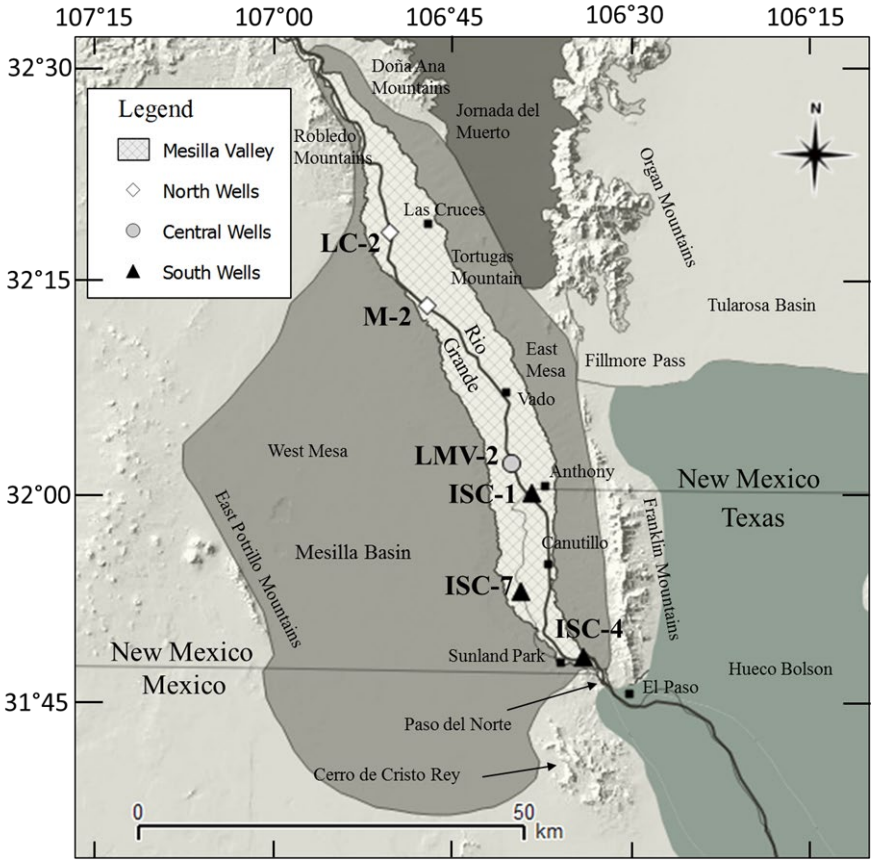

Figure 1. Study area showing sampling locations and alluvial aquifers (coloration indicates boundaries of aquifers). Mesilla Valley alluvial aquifer groundwater flow is generally from north to south.

The floodplain of the present-day Rio Grande and its inset fluvial sediments in the Mesilla Valley are hydrologically connected to the Santa Fe Group aquifer system in the surrounding Mesilla basin. Deposition of the Santa Fe Group in the Mesilla basin is defined by the local structure of the Rio Grande rift. The Mesilla basin is located in the Rio Grande rift, which extends from central Colorado across central New Mexico into west Texas and northern Chihuahua, Mexico (Hawley et al., 2001; Seager and Morgan 1979). Like other Rio Grande rift basins, the Mesilla basin trends from north to south, and the mountains flanking the east and west sides, act as structural and hydrologic boundaries (Collins and Raney 2000; Kelley and Matheny, 1983; Seager and Mack, 1994; Hawley and Kennedy, 2004). Major structural components include large sub-basins to the east, southwest, and northwest, a deeply buried mid-basin uplift, and a south-central basin that extends into northern Mexico west of the Cerro de Cristo Rey uplift (Hawley and Lozinsky, 1992). High-angle normal faults block out the various subbasins and uplifts (Hawley and Kennedy, 2004). Faulting of the Mesilla basin began during the Oligocene and continues into the present (Seager et al.,1987; Seager 1995; Hawley and Kennedy, 2004). This deformation, along with valley entrenchment and aggradation due to changes in streamflow during the glacial-interglacial cycles, have played an important role in sedimentation processes within the Mesilla basin (Hawley and Lozinsky, 1992; Witcher et al., 2004).

Tertiary to Quaternary sands and gravels of the Santa Fe Group form the primary basin-fill aquifer of the Mesilla basin (King et al., 1971, Wilson et al., 1981, Frenzel and Kaehler 1992, Hawley and Kennedy 2004). The basin-fill aquifer is generally semi-confined, but in some locations unconfined (Nickerson and Myers, 1993). Hawley and Kennedy (2004) informally subdivide the Santa Fe Group into the lower, middle, and upper hydrostratigraphic units or aquifers, which consist of up to 762 m of alluvial and fluvial sediments overlying bedrock (defined as basal rock formations with low permeability; Hawley and Kennedy, 2004). Groundwater production potential and hydraulic conductivity generally decrease with depth within subdivisions of the Santa Fe Group (Hawley et al., 2001). Most lithofacies in the upper Santa Fe Group have horizontal hydraulic conductivities between 5 and 30 m/day. In comparison, lower Santa Fe Group lithofacies have horizontal hydraulic conductivities of less than 1 m/day (Hawley et al., 2001). Flow is generally horizontal within the Santa Fe Group due to low vertical hydraulic conductivities (ranging from less than 0.1 m/day to 1 m/day; Frenzel and Kaehler, 1992). Santa Fe Group hydrostratigraphic subdivisions approximately correspond with transitions between formally designated formations and depth. For example, the Camp Rice Formation is considered the predominant lithofacies of the upper Santa Fe Group, the Fort Hancock Formation and Rincon Valley Formations are the predominant lithofacies of the middle Santa Fe Group, and the Hayner Ranch Formation is the main lithofacies of the lower Santa Fe Group (Seager et al., 1987; Hawley et al., 2001; Hawley and Kennedy, 2004; Witcher et al., 2004).

Late Pleistocene to Holocene inset Rio Grande deposits, 15 m to 38 m in thickness, form a smaller fluvial aquifer that overlies the Santa Fe Group within the Mesilla Valley (Hawley 1975; Wilson et al., 1981). High energy fluvial systems during the last Pleistocene glacial episodes caused valley entrenchment (Hawley and Kennedy, 2004). Subsequent backfilling by the Rio

Grande and its arroyo tributaries during the present late Quaternary interglacial episode resulted in deposition of the shallow fluvial aquifer beneath the valley flood plain (Hawley and Kennedy, 2004). The inset Rio Grande fluvial aquifer is largely unconfined and recharged by the Rio Grande and underlying Santa Fe Group (Nickerson and Myers, 1993).

Rock formations deposited before deposition of the Santa Fe Group define boundaries of the alluvial aquifer system but may transmit water through deep regional flow paths (Hawley and Kennedy, 2004). Generally, low permeability Eocene and Oligocene volcanic and volcaniclastic rocks underlie the Santa Fe Group throughout the central and northern Mesilla basin. Near the town of Canutillo, Texas, Tertiary volcanic and volcaniclastic rocks are missing and Santa Fe Group sediments overlie Eocene-Paleocene sedimentary rocks, sandstones, mudstones and conglomerates (Hawley, 2020, Fig. 21). An additional transition is observed just south of Canutillo, Texas where Santa Fe Group sediments rest unconformably on Cretaceous limestone, shales, and sandstones (Hawley, 2020, Fig. 21). The Cretaceous formations rise to the land surface, effectively pinching out the Santa Fe Group just south of Sunland Park, New Mexico (Hawley, 2020, Fig.21). Several andesite intrusions rupture Cretaceous units in the southern Mesilla Valley. The largest of these andesite intrusions is Cerro de Cristo Rey (Lovejoy, 1976; Lucas et al., 2010). A smaller andesite intrusion sits near Sunland Park, New Mexico (Hawley, 2020, Fig. 21). Andesite intrusions and Cretaceous units may be highly fractured and provide possible conduits for upward leakage of deep regional flow (Witcher et al., 2004).

Groundwater within the alluvial aquifer of the Mesilla basin primarily flows from northwest to south-southeast where it is discharged at the Paso del Norte into the Rio Grande (Hawley et al., 2001; Teeple, 2017). Increased Rio Grande salinity near the Paso del Norte indicates higher salinity groundwater at the Paso del Norte is discharged into the river where Cretaceous bedrock rises to the land surface (Hogan et al., 2007). Groundwater elevation contour maps indicate some flow may originate from the "Zona Hidrogeológica de Conejos-Médanos" area in northern Mexico and flow northwest into the southern Mesilla Valley (Hawley and Kennedy, 2004; IBWC, 2011; INEGI 2012).

Groundwater geochemically evolves between recharge and discharge in the Mesilla basin (Witcher et al., 2004). Recharge to the Mesilla basin aquifer system primarily occurs in the Mesilla Valley along losing reaches of the Rio Grande and irrigation canals, with smaller contributions of water from mountain front recharge (Frenzel and Kaehler, 1992; Teeple, 2017; Witcher et al., 2004). In mountain front recharge areas, total dissolved solids (TDS) is low (<250 mg/L) and characterized by the dominant ions of Ca^{2+}, Mg^{2+}, and HCO_3^- (Witcher et al., 2004). Recharge from the reach of the Rio Grande within the study area has a slightly greater TDS (400-1,200 mg/L) and retains a $Na^+/Cl^-/SO_4^{2-}$ water type (Moyer et al., 2013). Evaporative processes and upwelling of geothermal water can lead to elevated concentrations of dissolved solids (>2,000 mg/L) along agricultural drains; recharge from these drains often leads to elevated concentrations of dissolved ions in the shallow subsurface (CH2MHill, 2013; Witcher et al., 2004).

Once surface water has infiltrated, water-rock interactions and/or mixing may change the chemical composition of the water (Faure, 1986). Evaporative minerals halite, gypsum, and

anhydrite are present in sediments within the alluvial aquifer and contribute Na^+, Cl^-, SO_4^{2-}, and Ca^{2+} into solution (Witcher et al., 2004). When halite dissolves, Na^+ and Cl^- are released in a 1:1 manner. Generally, southern Mesilla basin groundwaters are enriched in Na^+ compared to Cl^-, suggesting additional processes are contributing Na^+. Cation exchange and/or dissolution of feldspars are possible sources for the addition of Na^+ to groundwater (Plummer et al., 2004; Teeple, 2017; Witcher, et al., 2004). Elevated concentrations of Cl^-, K^+, and SiO_2 are often associated with geothermal water, although elevated concentrations of these ions are also reported in waters in contact with evaporite mineral deposits (Witcher et al., 2004). Waters with elevated concentrations of trace ions are observed in the southern Mesilla basin, near the East Potrillo Mountains, and along the Mesilla Valley fault zone near Tortugas Mountain (Anderholm, 1992; Doremus and Michelsen 2008; Witcher et al., 2004). It should be noted that cold water dissolution of feldspars may also add K^+ and SiO_2 into solution (Witcher et al., 2004).

5. Methods and Approach

Groundwater samples were collected from nested wells, that is, wells that are characterized by negligible lateral distance between boreholes, and with substantial vertical variation between screen elevations, near the Rio Grande in the Mesilla Valley. Water levels were also measured at these wells to obtain insight into hydrogeochemical and hydraulic head changes vertically in the subsurface at each cluster of wells. Comparisons between the isotopic and geochemical composition of Mesilla Valley groundwaters in these well clusters provide a basis for identifying and interpreting flow paths, mixing, and salinity variations. Known sources of salinity (rock formations, surface water, other groundwater) were used to characterize sources, flow paths, and mixing relationships of these high salinity groundwaters. Several samples were collected from wells located outside the Mesilla Valley, one on the West Mesa, and another in the Jornada del Muerto basin to supplement data interpretation (Fig. 1).

A suite of groundwater constituents was measured from groundwater discharge pumped from selected wells (Fig. 1; Table 1.; Appendix A). Field sampling techniques were completed in accordance with the methodology described in the USGS field manual (U.S. Geological Survey, variously dated; Appendix C.). All data collected by the U.S. Geological Survey are available in the National Water Information System (U.S. Geological Survey, 2019) using the site identification numbers provided in table 5 in Appendix A. Dissolved gas samples were also collected from select wells and analyzed for radionuclides ^{39}Ar, ^{85}Kr, and ^{81}Kr (Fig. 1; Table 1.; Appendix C).

The USGS PHREEQC speciation program version 3.3.12 (Parkhurst and Appelo, 2013) was used to by staff and students at New Mexico State University to calculate the allowed speciation and saturation indices of minerals for water solutions. This information allowed us to interpret water-rock interactions along groundwater flow paths. Results were compared to geochemical analysis techniques including Piper diagrams (Piper, 1944) and isometric log ratios (Engle and Rowan, 2012). These results were used to determine sources of groundwater salinity and/or salinization processes within well clusters throughout the Mesilla Valley.

X-ray diffraction (XRD) analyses of gypsum and halite were used to evaluate the presence of evaporite minerals near the screened intervals of two well nests (Appendix C.). Two samples were selected from well cuttings of a central Mesilla Valley borehole (LMV-2), and five samples were selected from well cuttings from a southern Mesilla Valley well (ISC-4B). Other minerals were also identified, but not quantified.

In order to identify sources of dissolved sulfate in groundwater, the ratio of the two most common sulfur isotopes, reported as $\delta^{34}S$, was determined from samples of gypsum from the Miocene Rincon Valley Formation, the Cretaceous Mesilla Valley Shale, and Paleozoic deposits exposed in the present-day playa, Lake Lucero. These gypsum samples represent several hydrogeological units within the Mesilla basin: basin fill from the Santa Fe Group (the Miocene Rincon Valley Formation), Cretaceous shales, sandstones, and limestones (Mesilla Valley Shale),

dissolved sulfate in Mesilla basin groundwaters and surface waters initially collected to investigate anthropogenic sources of dissolved sulfate within the Rio Grande (Szynkiewcz et al., 2011).

The vertical component of local groundwater flow within well groupings was analyzed using temperature logs, because a vertically flowing groundwater component may systematically change the conductive temperature gradient via convective heat transport (Bredehoeft and Papadopulos, 1965). These changes in the natural temperature gradient can be observed and quantified to determine velocities of vertical groundwater flow, such as upflow (discharge) or as downflow (recharge). Temperature profiles were measured from the deepest well within the various well clusters to determine the vertical direction of flow (Appendix B). Detailed methods and data analysis techniques are reported in Appendix C.

Table 1. Table listing sample constituents and analytical methods.

Parameter	**Analytical Method**
Major Ions	Inductively coupled plasma optical emission spectrophotometry (ICP-OES), Fishman and Friedman (1989) and Ion-exchange chromatography, Fishman (1993)
Trace Ions	ICP-OES, Fishman and Friedman (1989), and inductively coupled plasma-mass spectrometry, Garbarino (1999), and Garbarino et al. (2006)
δD	Dual-inlet isotope-ratio mass spectrometry, Révész et al. (2008A)
$\delta^{18}O$	Dual-inlet isotope-ratio mass spectrometry, Révész et al. (2008B)
$\delta^{13}C$	Accelerator Mass spectroscopy, National Ocean Sciences Accelerator Mass Spectrometry Facility (2019)
^{14}C	Accelerator Mass spectroscopy, National Ocean Sciences Accelerator Mass Spectrometry Facility (2019)
^{3}H	Gas proportional counting, Östlund et al. (1969) and Östlund et al. (1974)
Uranium Isotopes (238U, 234U, 235U)	Section on Alpha Spectrometry (Tucker and Workman, 2013)
Noble Gas Concentrations (Kr, Xe, N_2, ^{4}He, Ne, Ar)	Mass spectroscopy, Hunt (2015)
Noble Gas Isotope Ratios ($^{3}He/^{4}He$, $^{20}Ne/^{22}Ne$, $^{40}Ar/^{36}Ar$, $^{86}Kr/^{84}Kr$, $^{130}Xe/^{132}Xe$)	Mass spectroscopy, Hunt (2015)
^{85}Kr	Atom Trap Trace Analysis (ATTA; Argonne National Lab) reported in Jiang et al. (2012) and Zappala (2017). Low-Level Counting (LLC; University of Bern) reported in Du et al. (2003)
^{81}Kr	ATTA in Jiang et al. (2012) and Zappala (2017).
^{39}Ar	LLC in Loosli (1983)
$\delta^{34}S$ of Gypsum	Preparation of $BaSO_4$, Szynkiewicz et al. (2011). Analysis of $BaSO_4$ by isotope ratio mass spectrometry, Kelly et al. (2018)
X-Ray Diffraction	Medville (2018)

6. Results

6.1 Sources of Recharge

Groundwater recharge is characterized by using the measured ratio of stable isotopes of oxygen, $\delta^{18}O$, and deuterium, δD in groundwater samples, and comparing these values with the Global Meteoric Water Line (GMWL; Craig, 1961) and the Rio Grande Evaporation Line (RGEL; Phillips et al., 2003). The RGEL relationship indicates evaporation processes due to pooling of water behind the Elephant Butte and Caballo Dams, evapotranspiration in the floodplain and return flows of drainage canals; and a warmer and dryer Holocene climate, resulting in a heavy $\delta^{18}O$ isotopic signature of the modern Rio Grande (Phillips et al.,2003; Teeple, 2017; Witcher et al., 2004; Fig. 2). Nearly all the groundwater samples from the Mesilla Valley fall along the RGEL and indicate that infiltration of river water is the predominant source of recharge for groundwater. Wells screened at depths between 0 and 45 m below land surface elevation (BLS) have substantially heavier $\delta^{18}O$ (-7.7 to -8.47) than wells screened below 122 m (-11.29 to -11.83). The heavier signature of $\delta^{18}O$ from wells screened between 0 and 45 m implies more recent recharge from the Rio Grande in the shallow wells. Wells screened below 122 m have lighter δD and $\delta^{18}O$ and plot between -12.5 and -10.5 $\delta^{18}O$, indicating the aquifer at depths greater than 122 m BLS has a large component of recharge from the Rio Grande dating back to the cooler periods of the Pleistocene (Teeple, 2017). Wells screened between 45-122 m have intermediate signatures (-7.69 to –11.96 $\delta^{18}O$) and may indicate mixing between old and young groundwaters. Teeple (2017) noted that precipitation in Santa Fe, New Mexico; El Paso Texas; and Ciudad Juárez, Chihuahua plot along the GMWL. Samples from wells ISC-7B and ISC-4A plot closer to the GMWL, which may indicate a recharge component of local storm or arroyo runoff.

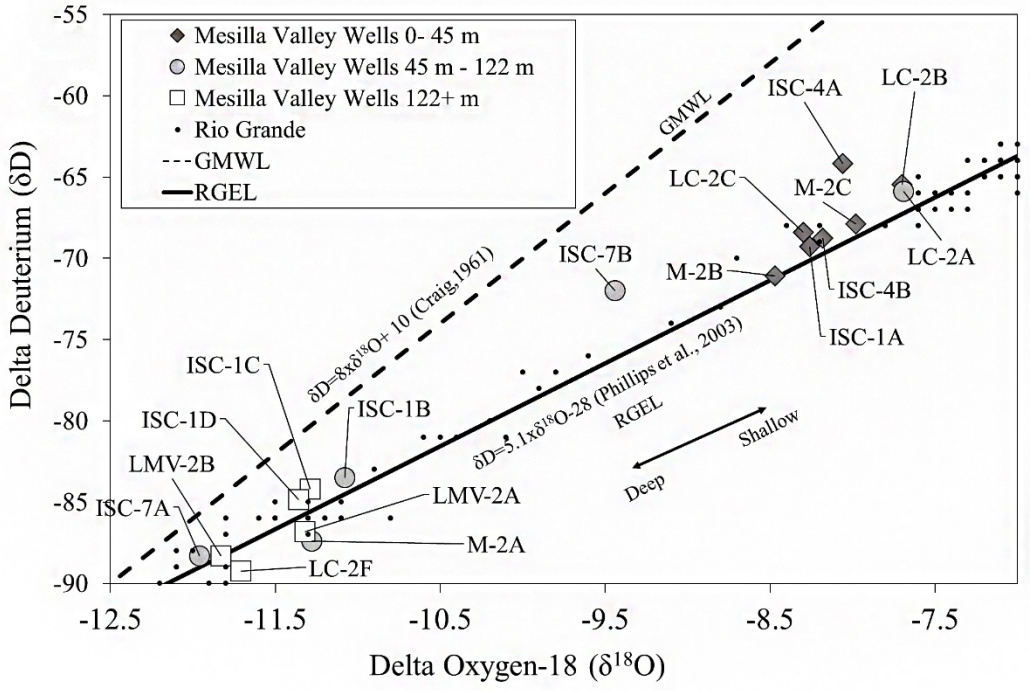

Figure 2. $\delta^{18}O$ versus δD diagram showing the stable isotope composition of groundwater in the Mesilla Valley and samples collected from the Rio Grande by Phillips et al. (2003).

6.2 Sources of Groundwater Salinity

Isometric log ratios (ILR; See Appendix C. for a short discussion on ILR) for the molar compositions of Ca^{2+}, Cl^-, Na^+, and SO_4^{2-} (Fig. 3) show southern Mesilla Valley groundwaters trend toward evaporite mineral equilibrium with increasing salinity and cation exchange. In northern Mesilla Valley groundwaters, there is a similar shift toward evaporite mineral equilibrium in higher TDS groundwater, but the overall TDS of northern Mesilla Valley waters is much lower (average is 530 mg/L) compared with the southern Mesilla Valley water (average is 6,800 mg/L). Most groundwater samples are enriched in Na^+ relative to Cl^-, as shown by a positive ILR balance on the X-axis in Fig. 3. Substantial increases in Na^+ are often associated with dissolution of silicate minerals, calcite dissolution, and/or cation-exchange (Teeple, 2017; Witcher et al., 2004). Such processes may be occurring within groundwaters screened at ISC-7A, which plots farthest to the right (Fig. 3).

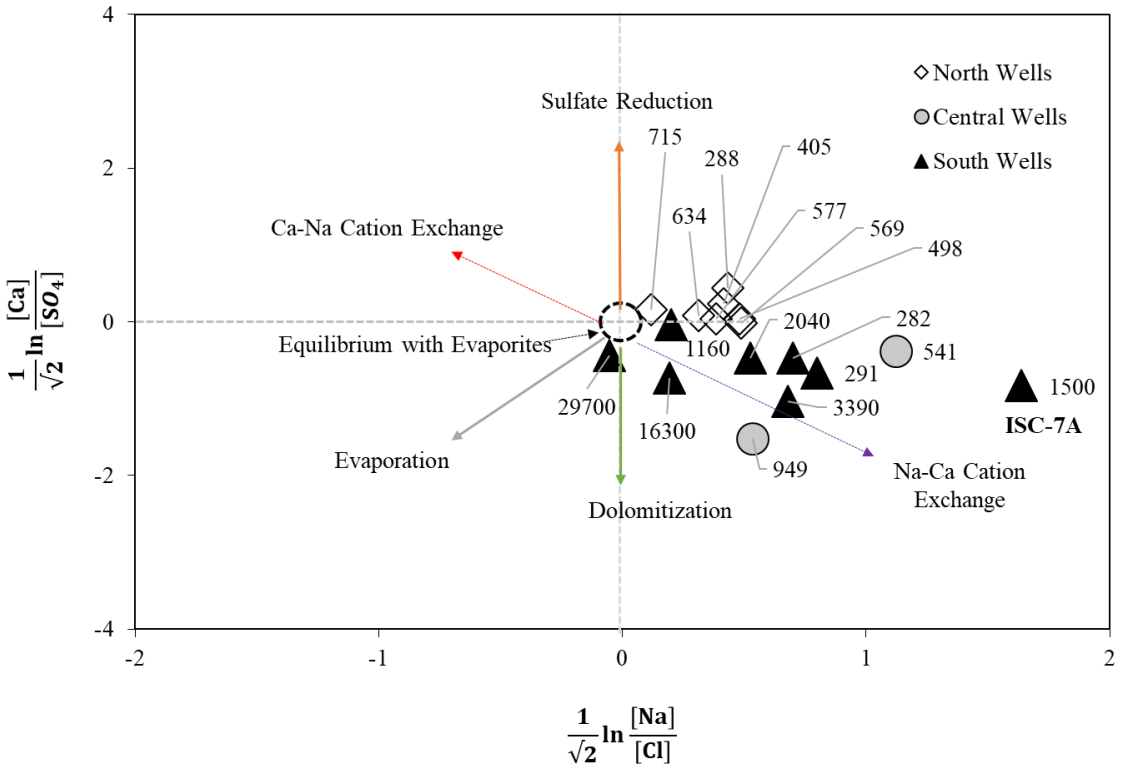

Figure 3. Isometric log ratio (ILR) diagram showing the molar compositions of Ca^{2+}, Cl^-, Na^+, and SO_4^{2-} (Engle and Rowan, 2012). Increasing proximity toward the center of the diagram indicates groundwater equilibrium with evaporite minerals. The points are labeled with the concentrations of total dissolved solids (TDS) in mg/L.

Southern and central Mesilla Valley groundwaters are enriched in SO_4^{2-} in relation to Ca^{2+} as shown by the negative ILR balance of the Y-axis in Figure 3. Witcher and others (2004) noted the enrichment of SO_4^{2-} in relation to Ca^{2+} is probably caused by the common ion effect, where dissolution of gypsum results in the precipitation of calcite ($CaCO_3$), removing excess Ca^{2+} from

solution. Dissolution of gypsum in southern Mesilla Valley waters may result in the precipitation of calcite. Saturation indices presented later in the paper, support the common ion effect. The saturation indices calculated for most groundwaters throughout the Mesilla Valley are oversaturated with respect to calcite (Table 2) and undersaturated with gypsum.An ILR plot of the molar compositions of Ca^{2+}, Cl^-, Na^+, and Br (Fig. 4) shows similar results as Figure 3. Southern Mesilla Valley groundwaters are enriched in Na^+ and Cl^- relative to Br shown by a positive ILR balance on the X-axis (Fig. 4). Substantial enrichments in Na^+ and Cl^- in relation to Br indicate contribution from halite dissolution (Engle and Rowan, 2012; Figure 4.). Northern Mesilla Valley waters are less enriched in Na^+ and Cl^- in relation to Br in comparison to southern wells, indicating less influence from evaporite mineral dissolution (Fig. 4). As noted by Davis and others (1998), Br ions are too large to fit within the crystal lattice of halite; consequently, dissolution of halite will not contribute Br into solution (Davis et al., 1998).

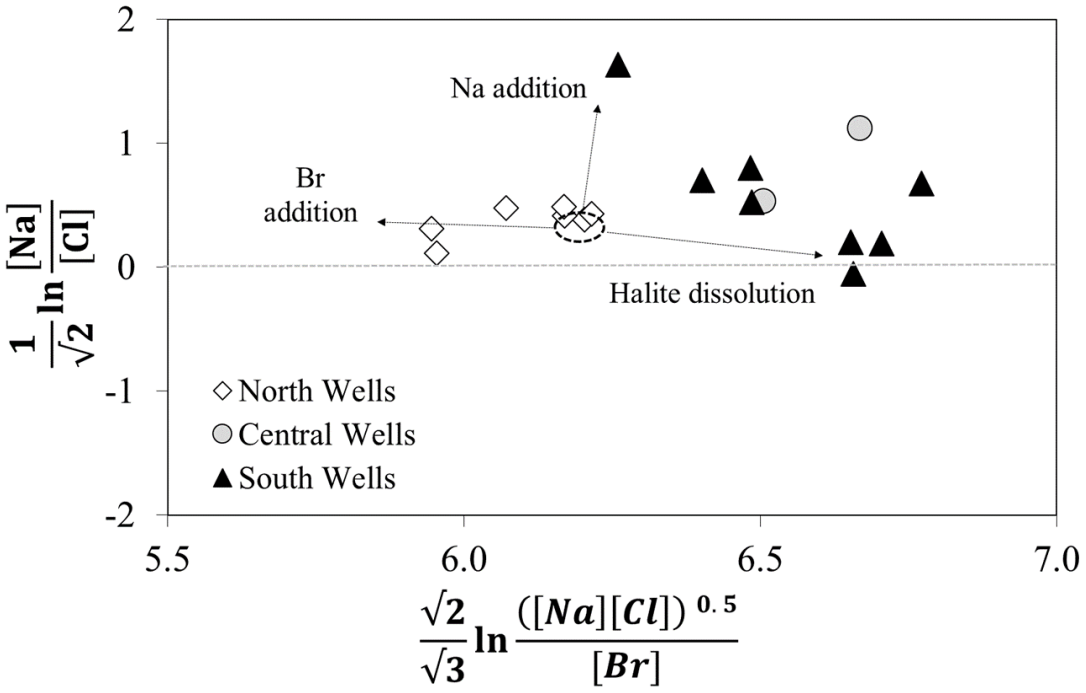

Figure 4. Isometric log ratio (ILR) diagrams (Engle and Rowan, 2012) illustrating halite dissolution in southern Mesilla Valley groundwaters. Northern Mesilla Valley groundwaters are less influenced by halite than southern Mesilla Valley groundwaters, shown by lower ILR balance values on the X-axis.

A Piper diagram (Fig. 5) shows similar results as Figures 3 and 4, with southern and central Mesilla Valley groundwaters exhibiting $Na^+/Cl^-/SO_4^{2-}$ dominant water types, likely an indicator of gypsum and halite dissolution. Northern Mesilla Valley groundwaters have a $Ca^{2+}/Na^+/HCO_3^-/Cl^-$ water type. Mixing between water types is apparent in the cation triangle of the Piper diagram where water type shifts linearly from Ca^{2+} dominant waters in northern Mesilla Valley groundwaters toward Na^+ dominant water in the central and southern Mesilla Valley. Results for

anions in the Piper diagram are more ambiguous, although there appears to be a general shift from HCO_3^- waters in the northern Mesilla Valley groundwater toward Cl^-/SO_4^{2-} waters in the southern Mesilla Valley. The transition in water types occurs from north to south and along the groundwater flow path, indicating increased influence from halite and gypsum dissolution and/or cation exchange in southern groundwaters.

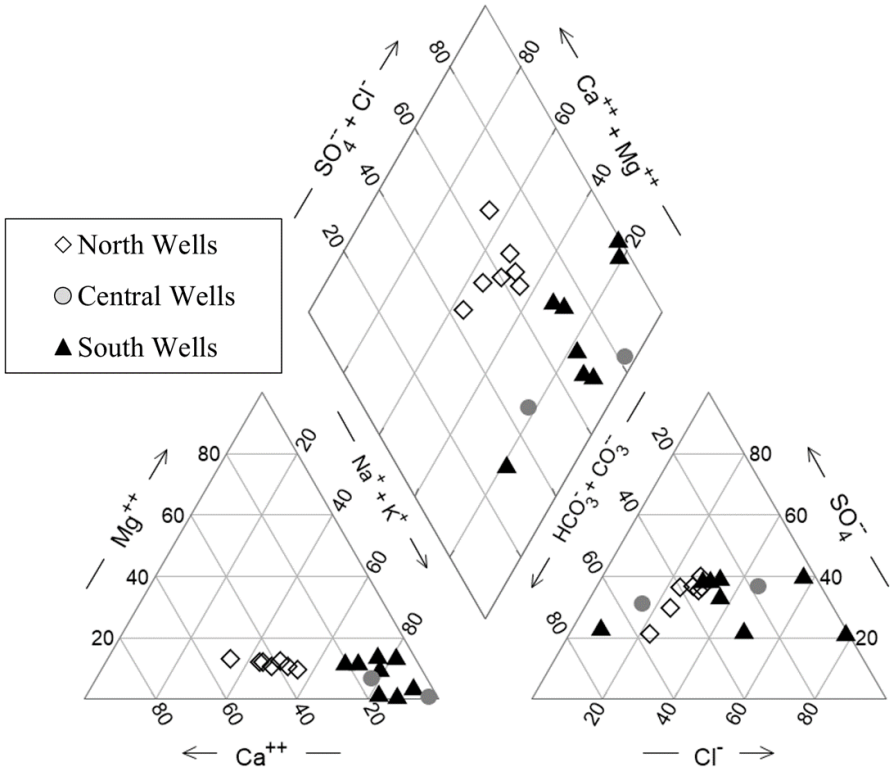

Figure 5. Piper diagram showing percent of total ions, in milliequivalents per liter, in Mesilla Valley groundwaters. Open diamonds indicate northern wells, gray circles indicate central wells, and black triangles indicate southern wells.

Mineral saturation indices (SI) show equilibrium with gypsum in southern Mesilla Valley groundwater near wells ISC-4A and ISC-4B (SI of 0 and 0.06), and undersaturation of gypsum (SI less than 0) for central and northern Mesilla Valley groundwater (Table 2). Southern Mesilla Valley wells are generally closer to equilibrium with halite (less negative SI) than central or northern Mesilla Valley wells. There is a large range of halite saturation indexes of southern Mesilla Valley waters (-7.03 to -2.74); however, ISC-4A and ISC-4B have less negative SI indicating that they are closer to equilibrium with halite (-3.4 and -2.74).). Evidence presented herein shows that groundwater salinity in the Mesilla Valley is increasingly derived from evaporite mineral dissolution and/or cation exchange as water flows southward. All water samples, except for ISC-1C and ISC-1D, were oversaturated with calcite suggesting precipitation of calcite is and/or has been occurring throughout the Mesilla Valley.

Table 2. Table showing saturation indices (SI) of evaporite minerals and calcite in Mesilla Valley groundwater (well order is from north to south). An SI value near zero represents equilibrium, negative indices represent undersaturation, and positive indices represent oversaturation.

Well ID	Gypsum	Halite	Anhydrite	Calcite
LC-2A	-1.35	-6.51	-1.59	0.11
LC-2B	-1.47	-6.56	-1.70	0.15
LC-2C	-1.55	-6.81	-1.77	0.14
LC-2F	-2.08	-7.32	-2.31	0.02
M-2A	-1.70	-6.98	-1.95	0.31
M-2B	-1.15	-6.57	-1.39	0.26
M-2C	-1.49	-6.58	-1.73	0.30
LMV-2A	-1.94	-6.72	-2.17	0.26
LMV-2B	-2.26	-5.70	-2.49	0.10
ISC-1A	-0.97	-5.32	-1.20	0.46
ISC-1B	-1.44	-5.62	-1.66	0.17
ISC-1C	-2.34	-7.03	-2.56	-0.08
ISC-1D	-2.44	-6.97	-2.67	-0.05
ISC-7A	-1.84	-6.08	-2.06	0.03
ISC-7B	-1.23	-4.78	-1.43	0.05
ISC-4A	0.00	-3.40	-0.22	0.58
ISC-4B	0.06	-2.74	-0.16	0.43

PHREEQC equilibrium phases show that when halite is fully dissolved in fresh water (i.e., TDS of 0 mg/L, pH of 7, and temperature of 25°C) specific conductance is 451,000 µS/cm. When gypsum is fully dissolved in fresh water, specific conductance is 2,160 µS/cm. Approximate conversions from specific conductance to TDS can be calculated for groundwater in the Mesilla basin using the equation TDS = specific conductance*0.66 (Witcher et al., 2004). Results from this equation indicate gypsum equilibrium occurs near 1,426 mg/L Ca^{2+} plus SO_4^{2-} and halite equilibrium occurs near 297,665 mg/L Na^+ plus Cl^-.

6.3 Spatial Distribution and Sources of Evaporite Minerals in the Subsurface

X-ray diffraction (XRD) analysis of well cuttings from ISC-4B and LMV-2 only tested positive for gypsum in the deepest 6 m of ISC-4B (Fig. 6). These well cuttings are from a light greenish-gray Cretaceous silty shale at 46.77 m to 54.86 m depth. These results confirm that gypsum occurs in Cretaceous bedrock in the southern Mesilla Valley. It is unclear from XRD analysis alone whether gypsum deposits in the Cretaceous shale originate from primary deposition or secondary minerals filling fractures and bedding planes.

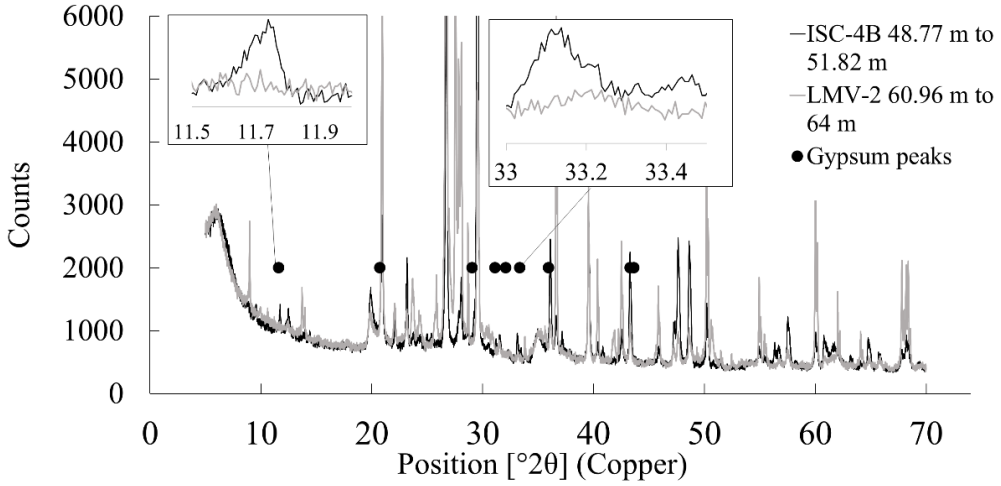

Figure 6. X-ray diffraction (XRD) results from cuttings collected during drilling of ISC-4B and LMV-2. Gypsum was identified in the well cuttings for ISC-4B (black), but was not identified in well cuttings for LMV-2 (light grey). Peaks for calcite, quartz, albite, illite, and clinochlore were also present, but not labeled in the figure. Gypsum peaks noted by black dots.

Gypsum $\delta^{34}S$ values from regional stratigraphic units vary greatly and allow identification of possible groundwater salinity endmembers. Reported gypsum $\delta^{34}S$ values are -24.1 for the Cretaceous Mesilla Valley Shale, +7.9 for the Miocene playa deposits of the Rincon Valley Formation (Hawley 2020, Fig. 18), and +12.5 for the modern Lake Lucero playa in the Tularosa basin (Appendix A; Table 10.). The distinctly negative $\delta^{34}S$ signature observed in the Mesilla Valley Shale is common for many non-magmatic sulfide minerals and sulfate that has formed from oxidation of these sulfides (Kirkland, 1982; Szynkiewicz et al., 2011; Szynkiewicz et al., 2012). Black shale within the upper Mesilla Valley Shale (Member C in Lucas et al., 2010) is rich in organic matter and probably formed in a poorly oxygenated marine environment, an ideal setting for the formation of pyrite (Lucas et al., 2010). When pyrite is oxidized, sulfuric acid is formed and may react with calcite to form gypsum with a depleted $\delta^{34}S$ signature (Kirkland, 1982). Sulfuric acid may also form when microbes interact with organosulfur compounds, which may then interact with calcite to form gypsum; such a process has been hypothesized to be the cause of depleted $\delta^{34}S$ in gypsum deposits in Carlsbad Caverns, New Mexico (Hill, 2000; Kirkland, 1982).

Additionally, pyrite is a common accessory mineral in igneous intrusions. Pyrite may be present as a trace mineral in andesite intrusions located near Sunland Park, New Mexico and at Cerro de Cristo Rey in Mexico. Pyrite in the andesite intrusions could have interacted with meteoric water resulting in oxidization and release of sulfate. However, magmatic sulfur in pyrite generally shows a narrow range $\delta^{34}S$ just above the standard Vienna Cañon Diablo Troilite (0‰ VCDT; Clark and Fritz, 1997).

The $\delta^{34}S$ signature of Lake Lucero playa gypsum matched the Permian anhydrite/gypsum sampled from the Yeso and San Andres Formations in the nearby southern Sacramento and San

Andres Mountains, New Mexico (+12.3‰ to +13.4‰) and gypsum sand of the White Sands dune field, New Mexico (+12.1 to +13.9‰; Szynkiewicz et al., 2010; Szynkiewicz et al., 2012). Similarities in $\delta^{34}S$ of gypsum from the Permian/Pennsylvanian throughout southern New Mexico, central New Mexico, and west Texas indicate the $\delta^{34}S$ of Permian/Pennsylvanian formations in the Mesilla basin would also have similar $\delta^{34}S$ signatures (Kirkland, 1982; Seager, 1981; Szynkiewicz et al., 2012; Szynkiewicz et al., 2010). Szynkiewicz and others (2010) showed a range of +10.9 to +15.1‰ for $\delta^{34}S$ in 23 samples of Permian gypsum/anhydrite deposits throughout southern and central New Mexico. These results are in good agreement with $\delta^{34}S$ of seawater during the Permian Period, which ranged from +9.5 to +12.5‰ (Kirkland et al., 2000). Although no samples were collected from Permian/Pennsylvanian sediments in the Mesilla basin, a likely formation of matching $\delta^{34}S$ signatures would be the gypsum deposits of the Pennsylvanian Panther Seep Formation in the Franklin Mountains (Kottlowski et al., 1956, Seager 1981). A $\delta^{34}S$ signature of the Miocene Rincon Valley Formation (+7.9‰) was lower than $\delta^{34}S$ signatures observed in Permian/Pennsylvanian age formations, and indicates gypsum from Rincon Valley playa deposits may originate primarily from the deeper older Permian/Pennsylvanian aged formations that had mixed with a smaller component of a lighter endmember.

6.4 Groundwater Flow Paths and Mixing of High Salinity Groundwater

In this section groundwater sulfate $\delta^{34}S$ is compared to the potential contributing gypsum $\delta^{34}S$ signatures presented in the previous section in order to present possible groundwater flow paths and mixing. A mixing line developed for sulfate $\delta^{34}S$ and TDS for potential gypsum endmembers, indicates mixing between the alluvial aquifer and upper Paleozoic sourced water in the southern Mesilla Valley groundwater (Fig. 7). Based on $\delta^{34}S$ signatures, a substantial component of groundwater SO_4^{2-} in the ISC-1 wells (+2.28 to +5.76‰ $\delta^{34}S$ signatures) is recharged from the Rio Grande (-1.6 to +0.9 ‰) or Mesilla Valley drainage canals with a fertilizer component (-2.1 to +1.6‰; Szynkiewcz et al., 2011). ISC-7 groundwater samples have slightly higher $\delta^{34}S$ signatures (+8.01 to +9.52‰) than the Rincon Valley Formation (+7.9‰) and indicate some influences from deeper Paleozoic units. Groundwater samples from the ISC-4 wells have $\delta^{34}S$ values (+12.36 to +12.46‰) similar to the reported Paleozoic $\delta^{34}S$ sulfate (Kirkland, 1982; Szynkiewcz et al., 2010; Szynkiewcz et al., 2011; Szynkiewcz et al., 2012).

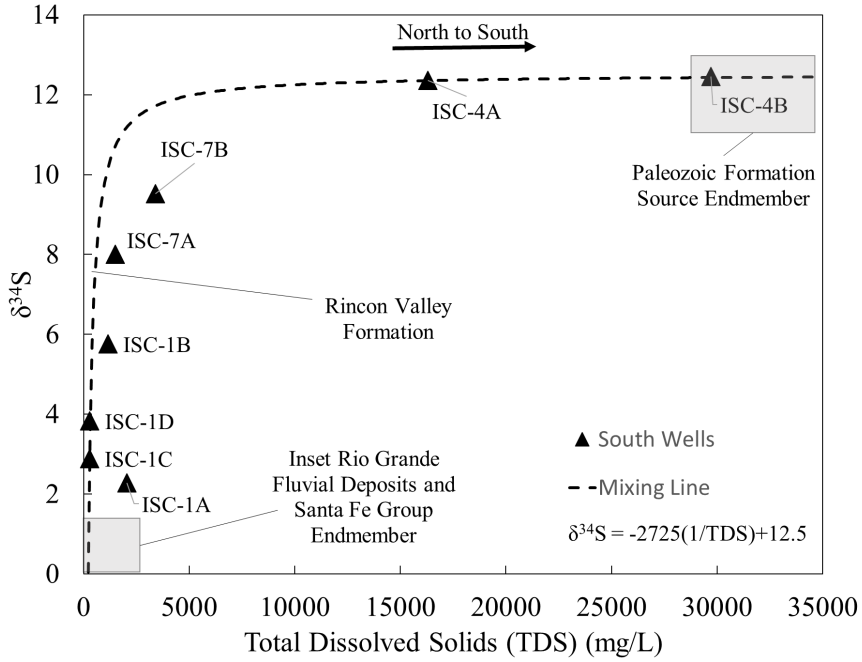

Figure 7. Diagram comparing groundwater $\delta^{34}S$ (data from Szynkiewcz et al., 2011) to TDS. A binary mixing line between the inset Rio Grande fluvial aquifer and Santa Fe Group Endmember and a possible Paleozoic formation endmember is presented (dashed line). Inset Rio Grande fluvial aquifer and Santa Fe Group Endmember refer to the $\delta^{34}S$ of the Rio Grande and Mesilla Valley irrigation canals, predominant sources of recharge to the alluvial aquifer.

Anoxic environments such as wetland, riparian areas, and oxbow lakes existed in the Mesilla Valley prior to agricultural development (Hawley et al., 2001; Lee, 1907; Witcher et al., 2004). Sulfate reduction occurs in such environments, and can decrease $\delta^{34}S$ by about 7‰. Such processes are thought to be negligible in groundwater in this study area due to the lack of soil

organic matter necessary for reduction to occur (Szynkiewicz et al., 2011). Additionally, ILR balances do not indicate sulfate reduction is occurring in any of the sampled groundwaters (Fig. 3). A similar binary mixing relationship between alluvial aquifer groundwater and Paleozoic bedrock derived water can also be observed using trace ions (Fig. 8). Trace ions Li^+ and K^+ appear to increase southward within the Mesilla Valley: the highest concentrations are observed in the ISC-4 well cluster followed by ISC-1 wells and ISC-7 wells. (Potassium is usually considered a major ion, but it is considered to be a trace ion here). Both Li^+ and K^+ can be geothermal indicators (Witcher et al., 2004). High concentrations of these ions in the southern Mesilla Valley support the hypothesis that a regional flow path is discharging into the alluvial aquifer (higher temperatures are associated with deeper flow paths).

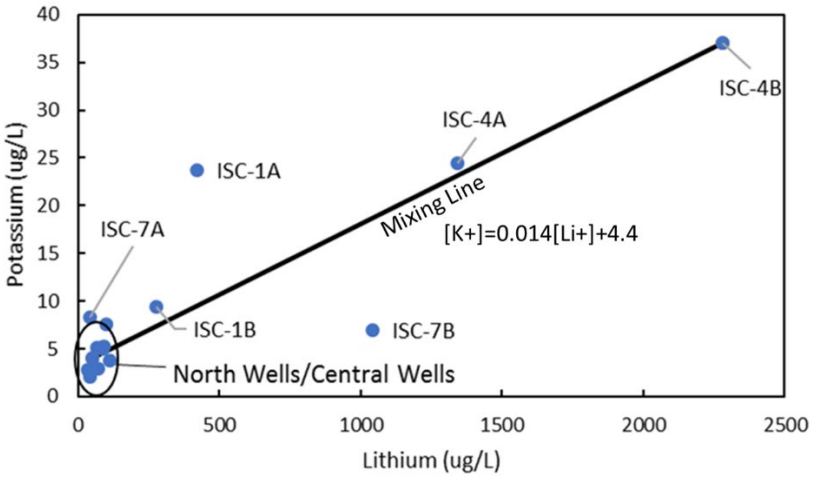

Figure 8. Diagram showing Li^+ concentrations compared to K^+ concentrations in Mesilla Valley groundwater. Mixing is shown between north and south Mesilla Valley groundwater.

Groundwater salinity increases with decreasing thickness of the Santa Fe Group in the southern Mesilla Valley, and a substantial salinity increase is coincident with the Santa Fe Group subcrop from volcanic to sedimentary rock (Fig. 9; modified from Hawley and Kennedy, 2004, Pl. 5c). A cross-section with well locations shows notable faults and transitions in Santa Fe Group subcrop lithology (Fig. 9). This also corresponds to the high salinity groundwater with sulfate $\delta^{34}S$ compositions that match Paleozoic $\delta^{34}S$ sulfate, but not Cretaceous $\delta^{34}S$ sulfate. The andesite intrusions shown in the Figure 9 cross-section in proximity of ISC-4 may provide a vertical pathway across the Cretaceous units through fractures within the andesite or in fractures along the contact between the andesite and the unintruded Cretaceous units (Hawley and Kennedy, 2004, Pl. 5c). Fault zones can also provide vertical permeability to allow flow across the Cretaceous confining units.

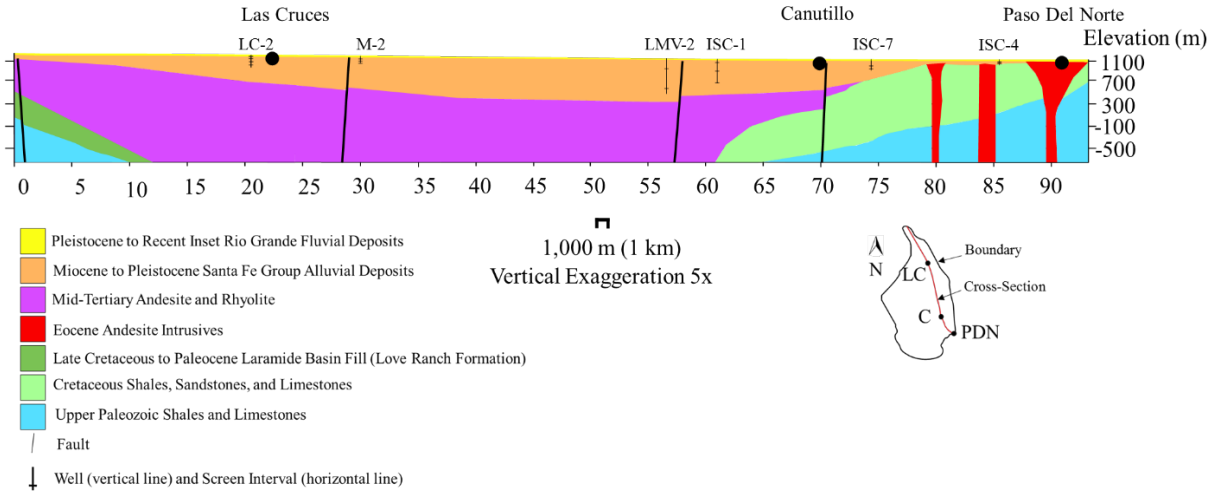

Figure 9. Geologic north-south (left-right) cross-section of the Mesilla Valley showing interpolated well locations and screen depths. Acronyms shown on inset location map represent towns shown on the cross-section: Las Cruces, New Mexico (LC), Canutillo, Texas (C), and the Paso del Norte, Texas (PDN; modified from Hawley and Kennedy, 2004, Plate 5c).

A notably thicker alluvial aquifer, relative to the thin alluvial aquifer of the southern Mesilla Valley, overlies the bedrock aquifer throughout most of the study area (Fig. 10). If groundwater were upwelling from bedrock units throughout the Mesilla Valley, the thick alluvial aquifer located throughout much of the northern and central Mesilla Valley would dilute high salinity groundwater derived from bedrock. Regional flow systems described by Hawley and Kennedy (2004) indicate vertical groundwater flow from bedrock occurs at the southern end of the Mesilla Valley within sedimentary units, and along faults in northern and central volcanic units. The Santa Fe Group subcrop north of Canutillo, Texas consists of middle Tertiary (Eocene to Oligocene) volcanic rocks that do not contain substantial amounts of gypsum (Hawley and Kennedy, 2004, Hawley 2020 [Figs. 21 and 22]).

A substantial increase in TDS is observed when the distance between the well screen and the bedrock is smaller in southern Mesilla Valley groundwaters, but not near central or northern well locations. These results indicate the Cretaceous bedrock present in the southern Mesilla Valley may be an important source of salinity in groundwater (Fig. 10). A similar relation is observed when comparing TDS to alluvial thickness. Salinity does not appear to be affected by the alluvial thickness in northern groundwaters, supporting the hypothesis that the bedrock is a less important source of groundwater salinity in the northern Mesilla Valley compared to the southern Mesilla Valley (Fig. 10).

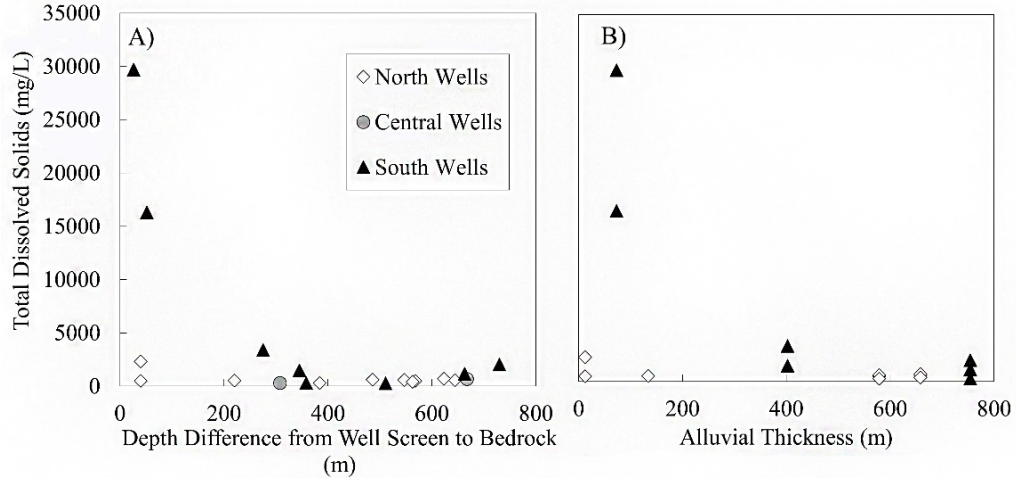

Figure 10. Diagrams comparing A) TDS to depth difference from well screen to bedrock and B) alluvial thickness of northern, central, and southern Mesilla Valley groundwater samples. Additional groundwater samples shown in Table 9 of Appendix A were used to supplement northern groundwater well data.

In addition to increasing TDS, the $\delta^{34}S$ values of the groundwater approach the Paleozoic $\delta^{34}S$ sulfate as the depth differences between well screen to the Santa Fe Group subcrop decrease in southern Mesilla Valley wells (Fig. 11). The roughly linear increase in $\delta^{34}S$ with decreasing depth difference from well screen to the Santa Fe Group subcrop supports a binary mixing model between a Santa Fe Group alluvial/Rio Grande fluvial aquifer endmember sulfate and a Paleozoic bedrock derived sulfate. Additionally, $\delta^{34}S$ increases in a near linear fashion, for wells in the south, with decreasing alluvial thickness, indicating decreases in dilution of bedrock derived groundwater from north to south in the Mesilla Valley (Fig. 11). The differences in the relationships presented in Fig. 10 and Fig. 11 are attributed to the fact that TDS includes multiple salts in addition to Ca^{2+} and SO_4^{2-}, and it is likely that Na^+ and Cl^- dominate the TDS at higher salinities because the solubility limit for halite dissolution is substantially greater than that of gypsum dissolution.

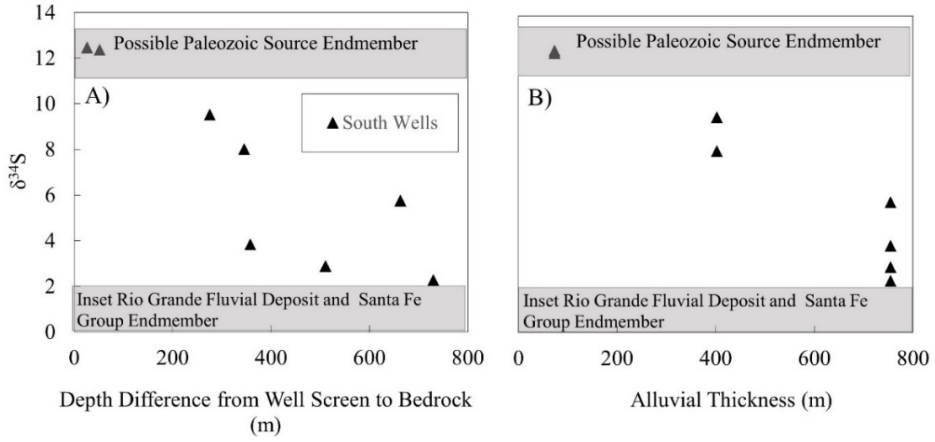

Figure 11. Diagram showing $\delta^{34}S$ (Szynkiewcz et al., 2011) compared to A) depth distance from well screen to bedrock, and B) alluvial thickness of southern Mesilla Valley groundwater samples. Data shown are also presented in Table 7 of Appendix A.

A contour plot of groundwater TDS sampled throughout the southern Mesilla Valley shows a plume of high-salinity groundwater localized around the ISC-4 well cluster (center of plume). The plume (>9,000 mg/L TDS) is ~5 km long by ~2 km wide (Fig. 12). The I-10 and the Three Sisters faults terminate near the plume. The likely increased vertical hydraulic conductivity within and immediately adjacent to the faults relative to the host lithology may provide a pathway for upward flow.

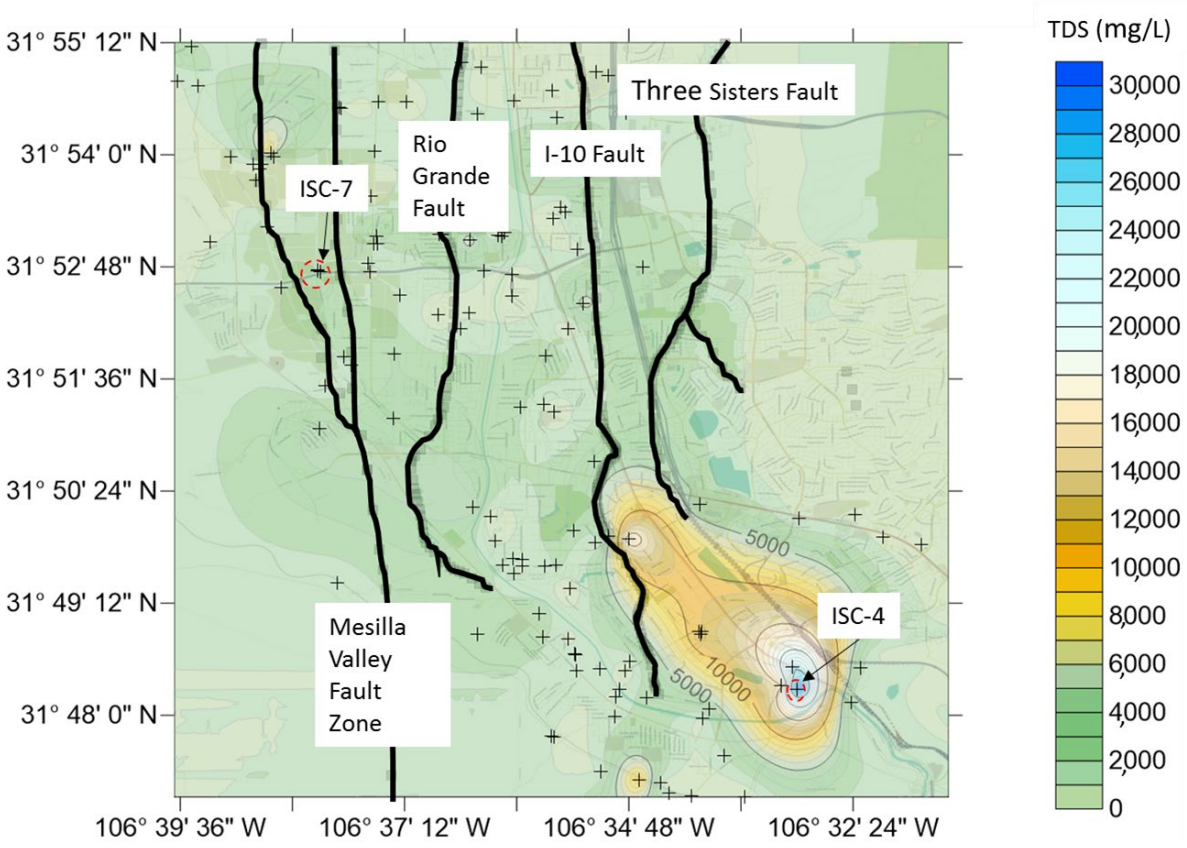

Figure 12. Total dissolved solids (TDS) contour plot showing the spatial distribution of groundwater TDS and major fault locations (Sweetkind, 2017) in the southern Mesilla Valley. TDS data and well locations (+) from Hiebing et al (2018).

If deep groundwater were flowing into the shallow Rio Grande fluvial aquifer and mixing, the high salinity plume is expected to have a thermal signature. Both ISC-4 wells sampled have temperatures several degrees cooler (21.5 °C) than thermally anomalous waters elsewhere in the Mesilla basin (>26 °C). Even so, groundwater sampled from the ISC-4 wells had elevated concentrations of the geothermal chemical indicators, Li and B, indicating a geothermal component (Witcher et al., 2004). These results indicate that deep groundwater may be upwelling upgradient of the ISC-4 well cluster and cooling as it flows laterally downgradient and south to the ISC-4 well screens. Sparse groundwater data south of the ISC-4 wells and Cerro de Cristo Rey do not effectively show where the southern boundary of the plume is located.

6.5 Vertical Direction of Flow in the ISC-4 Plume

Although thermally anomalous (>26 °C) waters were not observed in the ISC-4 wells, vertical temperature profiles may contain information related to the vertical upward or downward movement of water within the aquifer. To test this hypothesis, temperature profiles were recorded in both wells in the ISC-4 well cluster and the deepest wells of other well clusters. Appendix B shows temperature logs and their geothermal gradient for each of the well clusters sampled in the Mesilla basin with an additional profile from ISC-2A. Temperature profiles fell into several categories: (1) wells with conductive profiles (no vertical flow) indicated by a linear temperature increase with depth, (2) recharging conditions or downward flow indicated by concave upward profiles, and (3) discharging or upward flow shown by convex upward profiles. A substantial difference in thermal conductivity between clays and rock was also observed (ISC-7B; Appendix B), as shown by a decrease in geothermal gradient corresponding with a transition from clay to silty sand at ~35 m depth. Wells with recharge temperature profiles include the well cluster ISC-4 (Fig. 13) and ISC-2A (Appendix B). The recharge temperature profile indicates that shallow groundwater is moving down to deeper parts of the aquifer. This interpretation is consistent with groundwater levels measured at the wells. Advective transport of heat downward can cause the concave upward temperature profile shown in ISC-4 and ISC-2A (Reiter, 2001). However, upwelling of deep groundwater in this region was previously described in Section 6.4. This inconsistency requires further investigation, but there is a possibility of occurrence of both processes. Upward flow may be limited to the deeper regions, and downward infiltration may be limited to the shallower regions near land surface, which is supported by the available data.

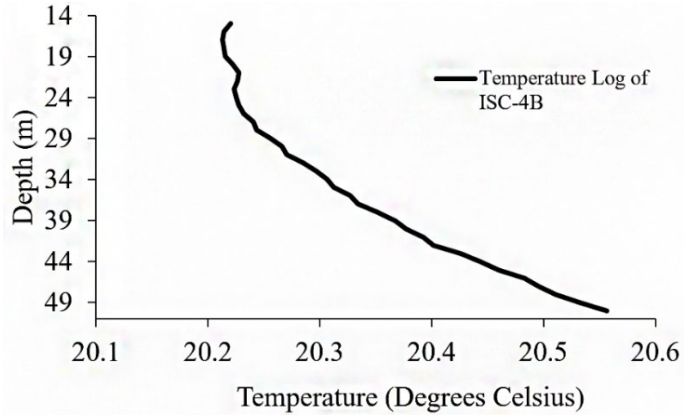

Figure 13. Temperature log of ISC-4B illustrating the temperature profile shape that is indicative of recharge from shallow sources (i.e., the concave upward shape).

6.6 Groundwater Age Results

Different groundwater age-dating tracers were generally consistent with various reported groundwater flow paths. However, groundwater sampled from wells ISC-4A and ISC-4B exhibited ^{39}Ar percent modern values greater than 100% (atmospheric ratio of $^{39}Ar/^{40}Ar$) indicating the subsurface production of ^{39}Ar (Fig. 14). This phenomenon is typically observed in sandstone aquifers, crystalline basement rocks, and occasionally sandy sediments (Ritterbusch et al., 2014; Mei et al., 2010). Subsurface production occurs due to: (1) in-situ neutron flux from nucleogenic reactions (produced by terrestrial processes), and/or (2) cosmic ray negative muon

interactions (Mei et al., 2010; Šrámek et al., 2017). Potential nucleonic sources of ^{39}Ar production within the Mesilla Valley include alluvial aquifer sands, Precambrian granite, and rhyolite of the Thunderbird Formation found in the Franklin Mountains, all of which contain higher concentrations of potassium, thorium, and uranium than surrounding host rock. For groundwater to accumulate ^{39}Ar from these nucleonic sources, prolonged contact must occur. One possibility may be that regional flow paths of ISC-4 groundwaters extend deeper into Precambrian units where ^{39}Ar production takes place.

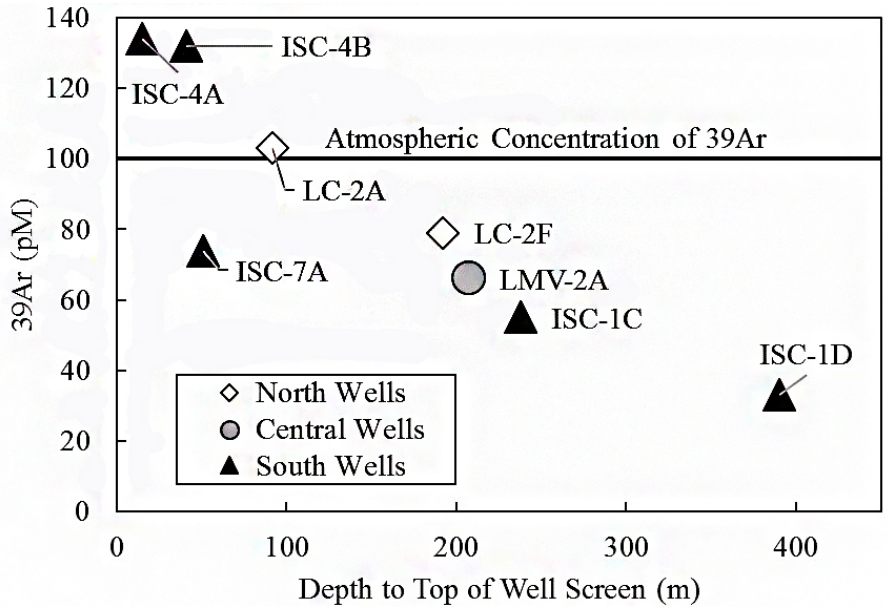

Figure 14. Diagram showing ^{39}Ar in groundwater compared to depth to top of well screen for Mesilla Valley wells.

Cosmogenic production of ^{39}Ar is also possible. Groundwater near the ISC-4A and ISC-4B well screens is close enough to the land surface that negative muon capture on ^{39}K produces ^{39}Ar (Šrámek et al., 2017).

$$\mu^- + {}^{39}K \rightarrow \nu\mu + {}^{39}Ar$$

where

μ^- is a muon

$\nu\mu$ is a muon neutrino

If muon capture were the dominant source of ^{39}Ar production in ISC-4 waters, then lower ^{39}Ar values from samples collected from other shallow wells (ISC-7A and LC-2A) cannot be readily explained. This evidence indicates in-situ neutron flux from nucleogenic reactions was the mechanism of ^{39}Ar production, and, by extension, the greater than atmospheric concentrations of ^{39}Ar indicate that old groundwater is present. A study by Mei and others (2010) concludes that uranium rich granites produce about 3×10^{-3} atoms ^{39}Ar /year per gram of rock. Loosli and others (1991) have suggested that if ^{39}Ar activities of groundwater are controlled solely by release of atoms by rocks, secular equilibrium would be reached within ~6 half-lives. With ^{39}Ar (half-life 269 years), this would occur after approximately 1,600 years. Thus, groundwater that has reached secular equilibrium with those rocks would be at least 1,600 years old.

Groundwater samples from southern, shallow wells ISC-4A, ISC-4B, and ISC-7A, all have low concentrations of tritium (<3 TU) when compared to groundwater sampled from other wells that have well screens less than 60 m (an arbitrary depth representative of the transition from high tritium concentrations to low tritium concentrations) below land surface (Fig. 15). These results indicate that older, tritium-depleted groundwaters are mixing with younger, tritium-rich recharge in the southern Mesilla Valley. In the north, groundwater sampled from LC-2A has an elevated tritium concentration when considering the well was screened below 60 m; this may indicate a preferential flow path between the Rio Grande recharge and the groundwater near the LC-2 well cluster. Groundwater elevations in the LC-2 well cluster also show a downward gradient allowing the potential for recharge from the shallow groundwater to deeper aquifers. However, the temperature profile of the same well cluster does not clearly show an expected concave upward profile indicative of recharging groundwater.

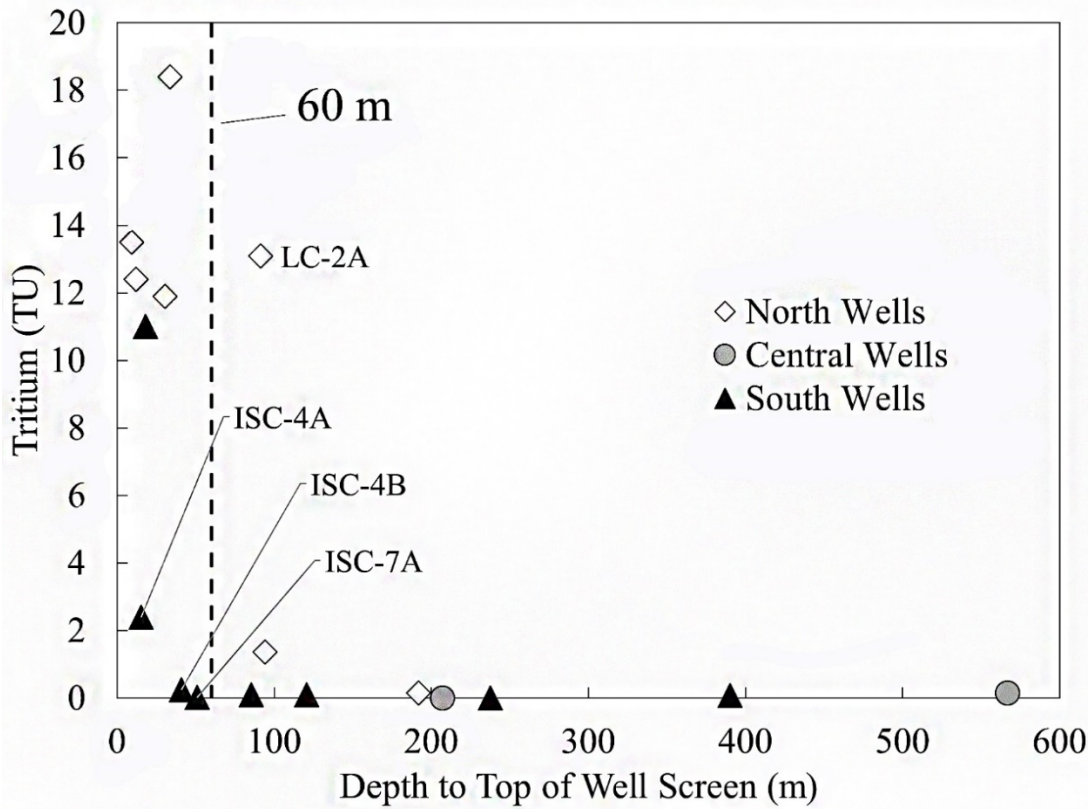

Figure 15. Diagram comparing tritium concentrations of groundwater samples versus depth below land surface to the top of well screen. The dotted line indicates depth below land surface to top of well screen of 60 m. Wells ISC-4A, ISC-4B and ISC-7A have particularly low amounts of tritium given their shallow screen depth, indicating mixing between older and younger waters. LC-2A is screened below 60 m, yet has substantial amounts of tritium, indicating greater connectivity between the Rio Grande and the LC-2A well.

As a radioisotope ^{14}C concentrations can be considered an indication of age or residence time in the aquifer. When depth to top of well screen is plotted against corrected ^{14}C concentrations (see Appendix C for short discussion of carbonate correction), "groundwater age-date gradients" between ^{14}C concentrations and depth are apparent (Fig. 16). Two different relations between ^{14}C concentrations and depth appear to be distinct when considering the groundwater salinity. The higher salinity (>1,000 mg/L TDS) samples have a large range of ^{14}C concentrations distributed over a relatively small depth range throughout the southern Mesilla Valley (solid trendline in Fig. 16), which results in large slope of ^{14}C versus depth (i.e., age-dating tracer concentration versus depth gradient). In contrast, the lower salinity samples (<1,000 mg/L TDS) exhibit a similar range ^{14}C concentrations over a smaller depth range (dashed trendline in Fig. 16). The anomalously low TDS concentrations in ISC-1D and ISC-1C, compared with other southern wells, also demonstrate a depth dependence of ^{14}C concentrations. These two differing trendlines between ^{14}C concentrations and depth are only distinguished by their salinity difference even though the majority of high salinity groundwater was located in the southern region. These results indicate these hydraulic gradients may be used to evaluate the heterogeneous flow path architecture of the aquifer and, that the high-salinity plume occurs at locations where older-age groundwater has migrated into the shallow groundwater system.

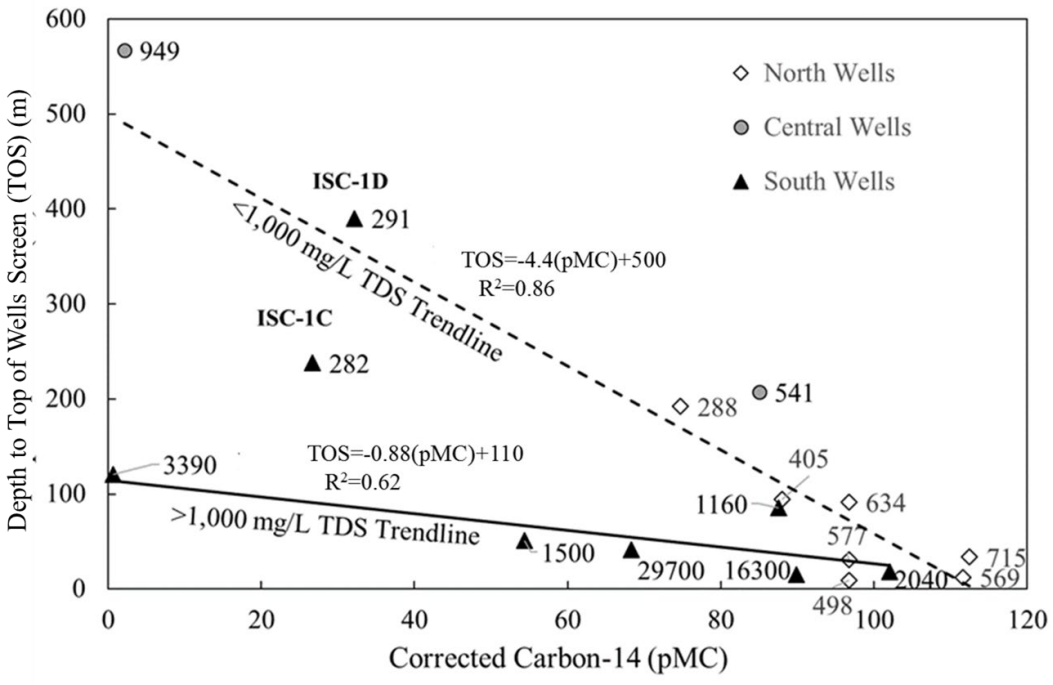

Figure 16. Diagram showing depth to top of well screen compared to corrected ^{14}C of groundwater samples throughout the Mesilla Valley. TDS values are shown next to data points. High salinity groundwaters tend to be older and are found in the southern Mesilla Valley. (pMC refers to percent modern carbon).

Similar to the relation of ^{14}C concentrations to depth (Fig. 16), salinity gradients between ^{4}He concentration and depth are observed when comparing ^{4}He with depth to top of well screen (Fig. 17). High salinity groundwaters in the southern Mesilla Valley tend to have higher concentrations of ^{4}He, indicating a component of older groundwater (>1,000 years; Kendall and McDonnell, 1998). Northern and central Mesilla Valley wells have lower concentrations of ^{4}He even at greater depths than southern wells and have lower in salinity (<1,000 mg/L). Groundwater sampled from southern wells ISC-1D and ISC-1C are both lower in salinity (<1,000 mg/L) and lack substantial concentrations of ^{4}He, which indicates the influence of older groundwater may be negligible in some southern wells.

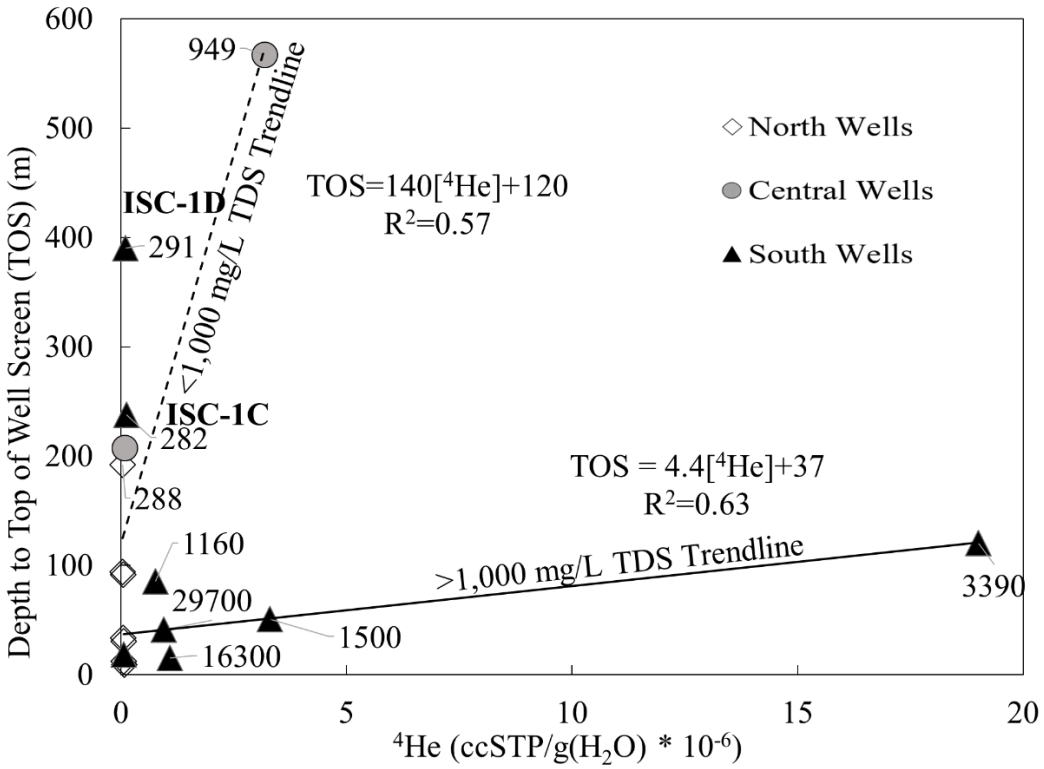

Figure 17. Diagram comparing depth to top of screen versus ^{4}He composition of groundwater samples throughout the Mesilla Valley. TDS values are shown next to data points.

Evidence from Figures 16 and 17 supports the hypothesis that high salinity groundwater is representative of old groundwater within the Mesilla Valley. As noted above, the two distinctly different age-dating tracer concentration versus depth gradients are primarily dependent on groundwater salinity ranges, which indicates that the high-salinity plume is where older-age groundwater occurs, or has migrated into, the shallow groundwater system. The presence of more than one age-dating versus depth gradient confirms the existence of heterogeneous flow path architecture within the aquifer.

Groundwater concentrations of ^{85}Kr were well below atmospheric concentrations, indicating most groundwater was recharged prior to 1950, although a modern signature can be observed in LC-2A (Table 3.; Kendall and McDonnell, 1998). Slight variation in ^{85}Kr reported values between University of Bern and Argonne National Laboratory can be attributed to variation in krypton

separation processes between the two laboratories and did not alter our groundwater age data interpretation (Jake Zappala, Argonne National Laboratory, written communication, January 3, 2019). ^{81}Kr of groundwater was equal to atmospheric ratios suggesting groundwater older than 50,000 years, the most recent detectable age for ^{81}Kr decay, was not present (Kendall and McDonnell, 1998).

Table 3. Age dating results of groundwater samples from wells throughout the Mesilla Valley.

Well Site	^{14}C, Water, Filtered, Non-Normalized (pMC)	^{14}C, modeled percent using revised Fontes/Garnier (pMC)	Tritium, Water, unfiltered (pCi/L)	^{85}Kr, U. of Bern (dpm/ccKr)	^{85}Kr, Argonne (dpm/ccKr)	^{39}Ar (pM)	^{4}He 10^{-8} ccSTP/g (H2O)
ISC-1A	102.06		11				6.77
ISC-1B	11.02	87.58	0.1				76.29
ISC-1C	8.20	26.66	-0.03	2.6	1.01	55	12.94
ISC-1D	8.41	32.18	0.08		0.63	33	10.48
ISC-4A	89.85		2.39	1.9	0.55	134	107.9
ISC-4B	68.33		0.24		0.81	132	95.1
ISC-7A	0.89	54.39	0.02	4.6	2.54	74	330.0
ISC-7B	0.09	0.60	0.1				1,900
LC-2A	96.73		13.1	52.2		103	4.64
LC-2B	96.76		11.9				5.89
LC-2C	96.71		13.5				6.91
LC-2F	74.75		0.15	0.5		79	4.14
LMV-2A	15.31	85.02	-0.15	2	0.37	66	8.86
LMV-2B	0.18	2.10	0.16				318.9
M-2A	88.04		1.37				4.34
M-2B	112.50		18.4				5.09
M-2C	111.62		12.4				5.85

$^{3}He/^{4}He$ signatures of groundwater (R) in ISC-7 wells are elevated relative to the $^{3}He/^{4}He$ fraction of the atmosphere (Ra) indicating leakage from the mantle (R/Ra ratio greater than 1; Williams et al., 2013; Fig. 18). Elevated R/Ra ratios are observed near fault zones that are sometimes associated with thermal waters in the Albuquerque basin of central New Mexico, (Williams et al., 2013), supporting a fault zone leakage in the vicinity of the ISC-7 wells. Elevated He/Ne ratios likely indicate older ages in the ISC-7 wells. He concentrations accumulate over time in the subsurface due to magmatic derived He and, more importantly, radiogenic decay of U and Th in various rock formations, while Ne does not (Kendall and McDonnell, 1998; Williams et al., 2013). In wells ISC-4A, ISC-4B, and LMV-2B, R/Ra ratios less than 1 and elevated He concentrations compared to Ne indicate prolonged contact between groundwater and rocks rich in U, Th, and K (Clark and Fritz, 1997).

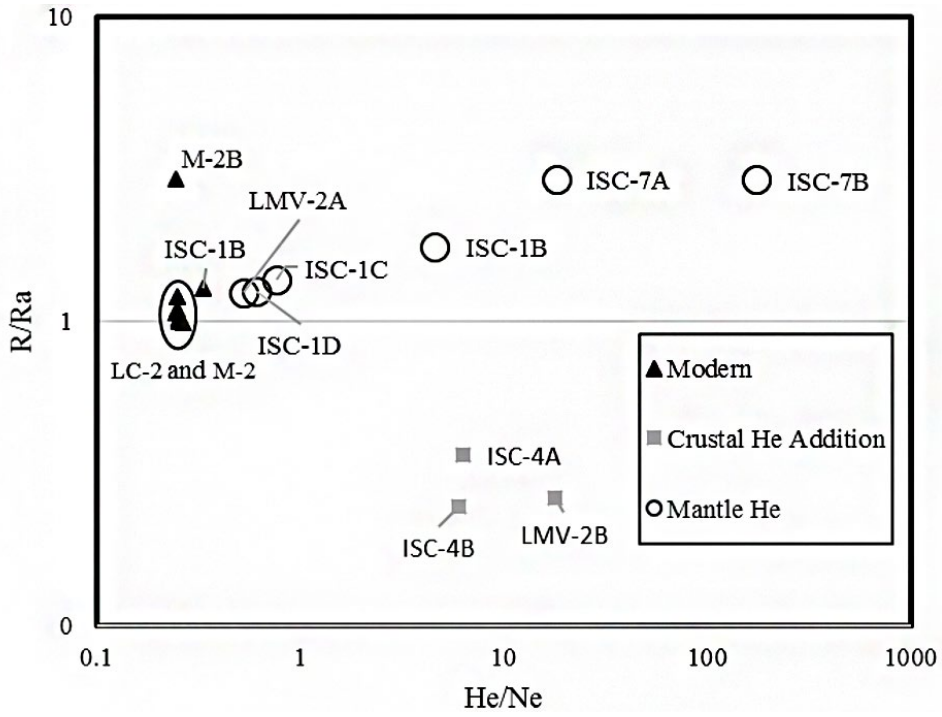

Figure 18. Diagram showing helium ratios measured at Mesilla Valley wells compared to ratios of He/Ne concentrations. In the Y-axis, R and Ra are defined as the $^{3}He/^{4}He$ signatures of the groundwater and atmosphere, respectively. Elevated $^{3}He/^{4}He$ ratios indicate connections to the mantle in ISC-7 and ISC-1 wells. Crustal decay (U, Th, and K decay within sedimentary rocks), which is the predominant source of He within the subsurface, is observed in other groundwater samples ISC-4A, ISC-4B, and LMV-2B.

7. Discussion

The high salinity groundwater of the ISC-4 area (>9,000 mg/L TDS) is highly localized to a ~5-km long by ~2-km wide plume. Several potential sources of salinity have been identified and discussed in the literature, and are outlined in Table 4. Throughout this section available data are used to hypothesis test each of these potential sources of salinity.

Table 4. Potential sources and flow paths of high salinity southern Mesilla Valley groundwater.

Source of Salinity	Mechanism of flow
[1] Evaporite minerals located in Paleozoic and Cretaceous Bedrock	Topographically driven regional flow (Hawley and Kennedy, 2004)
[2] Gypsum deposits located in Lake Palomas (Mexico)	Topographically driven regional flow (Hawley and Kennedy, 2004)
[3] Gypsum deposits located in the middle and lower Santa Fe	Topographically driven regional flow (Hogan et al., 2007; Phillips et al., 2003)
[4] Ancestral Oxbow Playa	Recharge from the Rio Grande and agricultural drains (Hiebing et al., 2018)
[5] Fertilizer from Irrigation	Recharge in flood irrigated fields (Sheng, 2013)
[6] Agricultural Drains	Recharge along agricultural drains (Witcher et al., 2004)
[7] Industrial Waste	Discharge from power plants and nearby industry into the Rio Grande (CH2MHill, 2013)
[8] Rio Grande	Recharge from the Rio Grande along losing reaches (Sheng, 2013).

Greater than atmospheric concentrations of ^{39}Ar, elevated concentrations of ^{4}He, and lower concentrations of ^{14}C and tritium relative to the shallow screen depths of the ISC-4 wells, support the hypothesis that "old" groundwater is discharging from/through underlying bedrock into the shallow alluvial aquifer in the southern Mesilla Valley. The I-10 and the Three Sisters' faults terminate within the plume indicating that several conduits for upward flow of deep groundwater may be present. An andesite intrusion, if fractured, several kilometers north of the ISC-4 well cluster may provide an additional input for deep, high salinity groundwater to flow from Paleozoic units into the shallower alluvial aquifer. Sulfate $\delta^{34}S$ values from groundwater match gypsum $\delta^{34}S$ values from underlying Paleozoic units and are substantially enriched when compared to $\delta^{34}S$ values of Cretaceous units. The gypsum was likely already equilibrated with groundwater prior to flowing through Cretaceous units (Table 4. [1]), because sulfate $\delta^{34}S$ values from groundwater differed from gypsum $\delta^{34}S$ values from Cretaceous units.

Hawley and Kennedy (2004) note that a substantial amount of paleo-recharge (pre-Holocene) may have been transported into the southern Mesilla Valley between Anthony, New Mexico and the Paso del Norte from ancestral Lake Palomas (Table 4. [2]). Research on Lake Palomas indicates that as late as the early Holocene, the floor of the Basin De Los Muertos was filled with a large lake that discharged northeast toward the Paso del Norte (Hawley and Kennedy, 2004). This northeast flow gradient may have operated until the installment of the new Ciudad Juárez Junta Municipal de Agua y Saneamiento (JMASCJ) well field in the "Zona Hidrogeológica de Conejos Médanos" of northern Mexico (CH2MHILL, 2013; Hawley and Kennedy, 2004; INEGI 2012; Alley, 2013). Although possible, it seems unlikely that Lake Palomas is the source of the high salinity groundwater at ISC-4 site because groundwater from the Conejos-Médanos aquifer of northern Mexico has an average salinity of ~2,000 mg/L, which is substantially lower than the observed TDS in the ISC-4 plume (IBWC, 2011). It is still unclear if a deeper regional flow path exists from the southwest.

Evaporite beds formed in oxbows or wetlands have been suggested to be another possible source of high salinity groundwaters observed throughout the Mesilla basin (Table 4. [4]; Hiebing, 2018). The highly localized nature of the ISC-4 plume and elevated uranium concentrations in ISC-4B (Appendix A; Table 12.) wells indicate an ancestral oxbow or wetland may be present. In this scenario, surface water within an ancestral wetland or oxbow would have evaporated, resulting in a shallow deposit of evaporite minerals. In addition to evaporite minerals, reducing conditions of the wetlands or oxbows would have led to the precipitation of uranium bearing minerals. If highly oxidized modern Rio Grande recharge were to flow though such deposits, uranium would become remobilized, leading to elevated concentrations in groundwater (Culbert and Leighton, 1988). If an oxbow were present and gypsum minerals were deposited as a result, XRD analysis would confirm the presence of gypsum throughout the Santa Fe Group of the ISC-4B well cuttings and not just in the upper layers of Cretaceous bedrock. As noted earlier, common features of highly reduced environments such as H_2S production and SO_4^{2-} reduction were not observed in the ISC-4 wells. Additionally, the presence of old groundwater found at shallow depths in the southern ISC-4 and ISC-7 well clusters could not easily be explained in this proposed scenario.

Others have attributed high salinity groundwater in the ISC-4 area to seepage from irrigation (Table 4. [5]; Sheng, 2013). This appears to be an unlikely source of groundwater salinity in the ISC-4 area because sulfate $\delta^{34}S$ values do not match $\delta^{34}S$ signatures of fertilizers, and nitrate concentrations also do not match plume of high TDS concentrations. Additionally, the TDS of the Rio Grande within the southern Mesilla Valley, which is the source of irrigation water, is ~1,000 mg/L, which is far less than the observed ~30,000 mg/L TDS in ISC-4B (CH2MHILL, 2013). It has been previously speculated that the Montoya Drain or industrial waste from the Rio Grande Power Plant may be the source of the high TDS groundwater in the ISC-4 plume (Table 4. [6,7]; CH2MHill, 2013). TDS measurements of the Montoya Drain taken during the winter between 1938 and 1990 never rose above 2,500 mg/L, indicating that these agricultural drains are not substantial sources for groundwater salinity in the ISC-4 plume (CH2MHill, 2013). Additionally, discharge from the Rio Grande Power Plant river outfall was noted to have a maximum discharge of 5,800 mg/L TDS (CH2MHill, 2013), much lower than the ~30,000 mg/L TDS in ISC-4B. Measurements of salinity in the Rio Grande near the Courchesne Bridge between 1938 and 2012 show river salinity is greatest during December with average salinity values of

~1,500 mg/L (Table 4. [8]; Witcher et al., 2004), indicating the reach of the Rio Grande adjacent to the ISC-4 plume is also not the main source of groundwater salinity to the plume.

An additional possible source of groundwater salinity within the ISC-4 plume is deep alluvial groundwater of the middle-lower Santa Fe Group that dissolves gypsum throughout a regional flow path and discharges into the shallow alluvial aquifer due to uplifted Cretaceous bedrock, which rises to the land surface at the southern end of the Mesilla Valley (Table 4. [3]). This scenario describes a topographically driven regional flow system where groundwater accumulates Ca^{2+} and SO_4^{2-} ions from gypsum interbedded in the Hayner Ranch, Fort Hancock, and Rincon Valley Formations of the middle and lower Santa Fe alluvial aquifer (Hawley and Kennedy 2004). Hiebing et al., (2018) suggested that Cl/Br ratios greater than 200, typical of geothermal waters in the region, in southern Mesilla Valley groundwaters was evidence for evaporite dissolution throughout the middle and lower Santa Fe Group. It seems plausible that the general changes in water type between the northern and central/southern Mesilla Valley may result from variations in gypsum and anhydrite deposition or presence in the middle and lower Santa Fe.

Additionally, old groundwater signatures observed in high salinity southern Mesilla Valley groundwaters could be explained by deep, old groundwater being forced to the surface by uplifted bedrock. Yet, $\delta^{34}S$ in the ISC-4 wells and ISC-7 wells are greater than $\delta^{34}S$ values in the Rincon Valley Formation, which indicates the source of salinity to southern Mesilla Valley groundwater is not in the rocks of the lower or middle Santa Fe Group. $\delta^{34}S$ and TDS also increase with decreasing depth difference between bedrock and well screens in the southern Mesilla Valley. These results indicate groundwater discharge through the Paleozoic and Cretaceous bedrock, as opposed to the Santa Fe Group rocks, is the main source of groundwater salinity to the ISC-4 plume and the southern Mesilla Valley. Further, the main source of groundwater salinity is the old groundwater being discharged from the bedrock, which is less diluted when the bedrock is closer to the well screens.

8. Conclusions and Future Research Needs

This investigation used geochemical tracers and lithological chemical analyses to improve understanding of groundwater flow, salinity sources, and flow path mixing in the Mesilla Valley. $\delta^{18}O$ and δD isotopes from groundwater samples support previous research that effectively shows groundwater in the Mesilla Valley has been recharged primarily from the Rio Grande. Geochemical modeling indicates evaporite minerals were an important source of groundwater salinity to waters throughout the Mesilla Valley. Increasing TDS in groundwater along north to south flow paths in the Mesilla Valley were correlated with increasing groundwater ages, and $\delta^{34}S$ groundwater signatures were comparable to Paleozoic units throughout southern New Mexico.

Fractured andesite intrusions and faults in the southern Mesilla Valley likely provide preferential flow paths for transport of Paleozoic-derived brackish groundwater into the shallow alluvial aquifer. A plume of high salinity groundwater near the Paso del Norte was shown to be the general location of discharge of Paleozoic sourced sulfate along a regional flow path. Underlying volcanic and volcanoclastic formations, in the central and northern Mesilla Valley, do not appear to contribute substantially to groundwater salinity in the central and northern alluvial aquifer. Instead, substantial increases in groundwater salinity in the Mesilla Valley appear to be related to proximity and connection to Paleozoic sedimentary units located in the southern Mesilla Valley. Variations in the age gradients for high salinity groundwater (>1,000 mg/L) and low salinity groundwater (<1,000 mg/L) were observed using both ^{4}He and corrected ^{14}C concentrations. These results indicate that groundwater salinity can be used as an indicator of groundwater age within the Mesilla Valley where high salinity groundwater contains an older component (>1,000 years).

Brackish water extraction for desalination and concentrate disposal is under consideration within the basin, and the results of this investigation may be used to support feasibility assessments using the characterization of the high TDS plume spatial distribution. Additionally, Paleozoic-derived brackish groundwater discharging from basement rock formations underlying the Santa Fe Group likely may have limited volumetric discharge rates relative to groundwater discharge through the Santa Fe Group (assuming basement hydraulic conductivity values are lower than those for Santa Fe Group), whereas further investigation would be required to quantify these rates.

Future research in this area could include drilling several deeper wells (screened in Cretaceous/Paleozoic bedrock) within the ISC-4 plume to improve current understanding of groundwater flow and sources of salinity. If groundwater was derived from Paleozoic units along a regional flow path, an upwelling geothermal signature would likely be observed in one or several deeper wells. Additional research may also improve current understanding of the relationship between groundwater age signatures, which are often offset from one another. Such research could improve our current understanding of the relationship between groundwater age and salinity in the Mesilla Valley, which appears to be correlated. This study illustrates how lithological analysis can be used in conjunction with water chemistry to characterize sources of salinity in a relatively homogenous aquifer system.

9. References

Alley, W.M., ed., 2013, Five-year interim report of the United States-Mexico Transboundary Aquifer Assessment Program—2007–2012: U.S. Geological Survey Open-File Report 2013–1059, 31 p.

Anderholm, S.K., 1992, Water quality and geochemistry of the Mesilla Basin, *in* Frenzel, P.F., and Kaehler, C.A., 1992, Geohydrology and simulation of ground-water flow in the Mesilla Basin, Doña Ana County, New Mexico and El Paso County, Texas: U.S. Geological Survey Professional Paper 1407–C, p. 64-73.

Anderson, M.P., 2005. Heat as a groundwater tracer: Groundwater, v. 43, no. 6, p. 951-968.

Bredehoeft, J.D., and Papadopulos, I.S., 1965, Rates of vertical groundwater movement estimated from the earth's thermal profile: Water Resources Research, v. 1, p. 325–328.

CH2MHill, 2013, Distal Mesilla conceptual site model prepared for the United States Army Corps of Engineers: Technical Report, 224 p.

Chen, C., Li, Y., Bailey, K., O'Connor, T., Young, L., and Lu, Z.-T., 1999, Ultrasensitive isotope trace analyses with a magneto-optical trap: Science, v. 286, no. 5442, p. 1139-1141.

Clark, I.D., and Fritz, Peter, 1997, Environmental Isotopes in Hydrogeology: Boca Raton, Fla., Lewis Publishers, 328 p.

Collins, E.W. and Raney, J.A., 2000, Geologic map of west Hueco Bolson, El Paso region, Texas: The University of Texas at Austin, Bureau of Economic Geology, Miscellaneous Map No. 40, scale 1:100,000.

Craig, Harmon, 1961, Isotopic variations in meteoric waters: Science, v. 133, p. 1702–1703.

Culbert, R., and Leighton, D., 1988, Young uranium: Ore Geology Reviews, v. 3, no. 1-3, p. 313-330.

Davis, S.N., Whittemore, D.O., and Fabryka-Martin, 1998, Uses of chloride/bromide ratios in studies of potable water: Groundwater v. 36, no. 2, p. 338–350.

Doremus, Dale, and Michelsen, A.M., 2008, Rio Grande salinity management—First steps towards interstate solutions, in Proceedings of the 53rd Annual New Mexico Surface Water Conference, Surface Water Opportunities in New Mexico, New Mexico Water Resources Research Institute, 8 p.

Du, X., Purtschert, R., Bailey, K., Lehmann, B.E., Lorenzo, R., Lu, Z.-T., Mueller, P., O'Connor, T.P., Sturchio, N.C., and Young, L., 2003, A new method of measuring ^{81}Kr and ^{85}Kr abundances in environmental samples: Geophysical Research Letters, v. 30, no. 20, 2068, doi:10.1029/2003GL018293.

Engle, M.A., and Rowan, E.L., 2012, Interpretation of Na–Cl–Br systematics in sedimentary basin brines: comparison of concentration, element ratio, and isometric log-ratio approaches: Mathematical Geosciences, v. 45, no. 1, p. 87-101.

Engle, M.A., Reyes, F.R., Varonka, M.S., Orem, W.H., Ma, L., Ianno, A.J., Schell, T.M., Xu, P., and Carroll, K.C., 2016, Geochemistry of formation waters from the Wolfcamp and "Cline" shales: Insights into brine origin, reservoir connectivity, and fluid flow in the Permian Basin, USA: Chemical Geology, v. 425, p. 76-92.

Faure, Gunter, 1986, Principles of Isotope Geology, Second Edition. New York, Wiley, p. 589

Fishman, M.J., 1993, Methods of analysis by the U.S. Geological Survey National Water Quality Laboratory—Determination of inorganic and organic constituents in water and fluvial sediments: U.S. Geological Survey Open-File Report 93–125, 217 p.

Fishman, M.J., and Friedman, L.C., 1989, Methods for determination of inorganic substances in water and fluvial sediments: U.S. Geological Survey Techniques of Water-Resources Investigations, book 5, chap. A1, 545 p.

Frenzel, P.F., and Kaehler, C.A., 1992, Geohydrology and simulation of groundwater flow in the Mesilla Basin, Doña Ana County, New Mexico and El Paso County, Texas: U.S. Geological Survey Professional Paper 1407–C, 114 p.

Garbarino, J.R., 1999, Methods of analysis by the U.S. Geological Survey National Water Quality Laboratory—Determination of dissolved arsenic, boron, lithium, selenium, strontium, thallium, and vanadium using inductively coupled plasma-mass spectrometry: U.S. Geological Survey Open-File Report 99–093, 31 p.

Garbarino, J.R., Kanagy, L.K., and Cree, M.E., 2006, Determination of elements in natural-water, biota, sediment and soil samples using collision/reaction cell inductively coupled plasma-mass spectrometry: U.S. Geological Survey Techniques and Methods, book 5, sec. B, chap. 1, 88 p.

Haenel, R., Rybach, L., and Stegena, L., 1988, Fundamentals of Geothermics, Handbook of Terrestrial Heat-Flow Density Determination: Springer, p. 9-57.

Hagedorn, B., 2015, Hydrochemical and ^{14}C constraints on groundwater recharge and interbasin flow in an arid watershed: Tule Desert, Nevada: Journal of Hydrology, v. 523, p. 297-308.

Han, L.-F., and Plummer, L.N., 2013, Revision of Fontes & Garnier's model for the initial ^{14}C content of dissolved inorganic carbon used in groundwater dating: Chemical Geology, v. 351, p. 105-114.

Hawley, J.W., 1975, Quaternary history of Doña Ana County region, south-central New Mexico: New Mexico Geological Society Guidebook 26, p. 139-150.

Hawley, J. W., 2020, A Hydrogeologic perspective on groundwater conservation in the northern Rio Grande basin, New Mexico, Texas, and Chihuahua—2014 Albert E. Utton Memorial Lecture, *in* Sheely, M., ed. Proceedings, 59th Annual New Mexico Water Conference, Santa Fe, NM., p. 59-85.

Hawley, J.W., Kennedy, J.F., and Creel, B.J., 2001, The Mesilla basin aquifer system of New Mexico, west Texas and Chihuahua—An overview of its hydrogeologic framework and related aspects of groundwater flow and chemistry, in Mace, R.E., and Angle, E.S., Aquifers of West Texas: Texas Water Development Board Report 356, chap. 7, p. 76–99.

Hawley, J.W., and Kennedy, J.F., 2004, Creation of a digital hydrogeologic framework model of the Mesilla Basin and southern Jornada del Muerto Basin: Las Cruces, New Mexico Water Resources Research Institute, New Mexico State University, WRRI Technical Completion Report no. 332, 105 p.

Hawley, J.W., and Lozinsky, R.P., 1992, Hydrogeologic framework of the Mesilla Basin in New Mexico and western Texas: New Mexico Bureau of Mines and Mineral Resources Open File Report 323, 55 p.

Hiebing, M., Doser, D.I., Avila, V.M., and Ma, L., 2018, Geophysical studies of fault and bedrock control on groundwater geochemistry within the southern Mesilla Basin, western Texas and southern New Mexico: Geosphere, v. 14, no. 4, p. 1912-1934.

Hill, C.A., 2000, Overview of the geologic history of cave development in the Guadalupe Mountains, New Mexico: Journal of Cave and Karst Studies, v. 62, no. 2, p. 60-71.

Hogan, J.F., Phillips, F.M., Mills, S.K., Hendrickx, J.M.H., Ruiz, Joaquin, Chelsey, J.T., and Asmerom, Yamane, 2007, Geologic origins of salinization in a semiarid river—The role of sedimentary basin brines: Geology, v. 35, p. 1063-1066.

Hunt, A.G., 2015. US Geological Survey Noble Gas Laboratory's standard operating procedures for the measurement of dissolved gas in water samples Book 5, Laboratory Analysis: U.S. Geological Survey, 21 p.

INEGI, 2012, Zona Hidrogeológica Conejos-Médanos: Instituto Nacional de Estadística y Geografía, Edificio Sede, Av. Héroe de Nacozari Sur 2301, Fraccionamiento Jardines del Parque, 20276, Aguascalientes, Aguascalientes; DR©2012, Impreso en México. www.inegi.org.mx; atencion.usuarios@inegi.org.mx

International Atomic Energy Agency, 2013, Isotopes Methods For Dating Old Groundwater: Guidebook, Vienna, 357 p.

International Boundary and Water Commission (IBWC), 2011, Hydrogeological activities in the Conejos-Medanos/Mesilla Basin Aquifer, Chihuahua Phase I: New Mexico Water Resources Research Institute, Transboundary Assessment Program Report.

Jiang, W., Bailey, K., Lu, Z.-T., Mueller, P., O'Connor, T., Cheng, C.-F., Hu, S.-M., Purtschert, R., Sturchio, N., and Sun, Y., 2012, An atom counter for measuring ^{81}Kr and ^{85}Kr in environmental samples: Geochimica et Cosmochimica Acta, v. 91, p. 1-6.

Kelley, S. A. and Matheny, J. P., 1983, Geology of Anthony quadrangle, Doña Ana County, New Mexico: New Mexico Bureau of Mines and Mineral Resources, Geologic Map 54, scale 1:24,000.

Kelley, S., Folsom, M., Keller, S., and Jiracek, G., 2016, Preliminary analysis of complex subsurface temperature variations in the Buckman well field, Santa Fe County, New Mexico, SEG Technical Program Expanded Abstracts 2016: Society of Exploration Geophysicists, p. 4941-4945.

Kelly, W., Panno, S., Hackley, K., Hadley, D., and Mannix, D., 2018, Paleohydrogeology of a Paleozoic sandstone aquifer within an intracratonic basin: Geochemical and structural controls: Journal of Hydrology, v. 565, p. 805-818.

Kendall, Carol, and McDonnell, J.J., 1998, Isotope Tracers in Catchment Hydrology: Elsevier Science B.V., Amsterdam, 839 p.

King, W., and Hawley, J., 1975, Geology and ground-water resources of the Las Cruces area: New Mexico Geological Society 26th Annual Field Conference, p. 195-204.

King, W. E., Hawley, J. W., Taylor, A. M. and Wilson, R. P., 1971, Geology and ground-water resources of central and western Doña Ana County, New Mexico: New Mexico Bureau of Mines and Mineral Resources, Hydrologic Report 1, 64 p.

Kirkland, D.W., 1982, Origin of gypsum deposits in Carlsbad Caverns, New Mexico: New Mexico Geology, v. 4, no. 2, p. 20-21.

Kirkland, D.W., Denison, R.E., and Dean, W.E., 2000, Parent brine of the Castile evaporites (Upper Permian), Texas and New Mexico: Journal of Sedimentary Research, v. 70, p. 749–761.

Kottlowski, F.E., Flower, R.H., Thompson, M.L., Foster, R.W., 1956, Stratigraphic studies of the San Andres Mountains, New Mexico, State Bureau of Mines and Mineral Resources: Memoir 1, New Mexico Institute of Mining and Technology, p. 132.

Land, L., 2016, Overview of Fresh and Brackish Water Quality in New Mexico: New Mexico Bureau of Geology, Open-file Report 583, 49 p.

Lee, W.T., 1907, Water Resources of the Rio Grande Valley in New Mexico, U.S. Geological Survey: Water Supply Paper 188, 59 p.

Leggat, E. R., Lowry, M. E. and Hood, J. W., 1962, Ground-water resources of the lower Mesilla Valley, Texas and New Mexico: Texas Water Commission, Bulletin 6203, 191 p.

Loosli, H., 1983, A dating method with ^{39}Ar: Earth and Planetary Science Letters, v. 63, no. 1, p. 51-62.

Loosli, H.H, Lehmann, B.E, and Däppen, G., 1991, 4. Dating by Radionuclides, Applied Isotope Hydrology, A case study in Northern Switzerland: Studies In Environmental Science, v. 43, Elsevier, Amsterdam, p. 153-174.

Lovejoy, E.M.P, 1976, Geology of Cerro de Cristo Rey Uplift, Chihuahua and New Mexico: New Mexico Bureau of Mines & Mineral Resources Memoir 31, 84 p.

Lucas, S.G., Krainer, K., Spielmann, J.A., and Durney, K., 2010, Cretaceous stratigraphy, paleontology, petrography, depositional environments, and cycle stratigraphy at Cerro de Cristo Rey, Doña Ana County, New Mexico: New Mexico Geology, v. 32, no. 4, p. 103-130.

Medville, D.M., 2018, Speleogenesis of caves in a Cretaceous shale: Bighorn Basin, Wyoming: Journal of Cave and Karst Studies, v. 80, no. 2, p. 66-80.

Mei, D.-M., Yin, Z.-B., Spaans, J., Koppang, M., Hime, A., Keller, C., & Gehman, V., 2010, Prediction of underground argon content for dark matter experiments: Physical Review C, v. 81, 7 p.

Miao, Z., 2013, Application of stable isotopes and geochemical analysis to characterize sulfate, nitrate, and trace element contamination of groundwater and its remediation at a former uranium mining site: Tucson, University of Arizona, M.S. thesis, 168 p.

Moore, S.J., Bassett, R.L., Liu, B., Wolf, C.P., and Doremus, D., 2008, Geochemical tracers to evaluate hydrogeologic controls on river salinization: Ground Water, v. 46, no. 3, p. 489-501. (F2, H2)

Moyer, D.L., Anderholm, S.K., Hogan, J.F., Phillips, F.M., Hibbs, B.J., Witcher, J.C., Matherne, A.M., and Falk, S.E., 2013, Knowledge and understanding of dissolved solids in the Rio Grande–San Acacia, New Mexico, to Fort Quitman, Texas, and plan for future studies and monitoring: U.S. Geological Survey Open-File Report 2013–1190, 55 p.

National Ocean Sciences Accelerator Mass Spectrometry Facility, 2015, General statement of ^{14}C procedures at the National Ocean Sciences AMS Facility: National Ocean Sciences Accelerator Mass Spectrometry Web page, accessed July 2019 at http://www.whoi.edu/nosams/generalstatement-of-14c-procedures.

Nickerson, E.L., 2006, Description of piezometers and ground-water-quality characteristics at three new sites in the lower Mesilla Valley, Texas, and New Mexico: U.S. Geological Survey Scientific Investigations Report, 2005-5248, 27 p.

Nickerson, E.L., and Myers, R.G., 1993, Geohydrology of the Mesilla ground-water basin, Doña Ana County, New Mexico, and El Paso County, Texas: U.S. Geological Survey Water-Resources Investigations Report 92–4156, 96 p.

Oeschger, H., and Wahlen, M., 1975, Low level counting techniques: Annual Review of Nuclear Science, v. 25, no. 1, p. 423-463.

Östlund, H., Dorsey, H.G., and Rooth, C.G., 1974, GEOSECS North Atlantic radiocarbon and tritium results: Earth and Planetary Science Letters, v. 23, no. 1, p. 69-86.

Östlund, H.G., Rinkel, M.O., and Rooth, C., 1969, Tritium in the equatorial Atlantic current system: Journal of Geophysical Research, v. 74, no. 18, p. 4535-4543.

Parkhurst, D.L, and Appelo, C.A.J, 2013, PHREEQC Version 3: A Computer Program for Speciation, Batch-reaction, One dimensional Transport, and Inverse Geochemical Calculations, U.S. Geological Survey, Denver, Colorado.

Phillips, F.M., Hogan, J.F., Mills, S.K., and Hendrickx, J.M.H., 2003, Environmental tracers applied to quantifying causes of salinity in arid-region rivers Preliminary results from the Rio Grande, southwestern USA, in Alsharhan, A.S., and Wood, W.W., eds., Water Resources Perspectives— Evaluation, Management, and Policy: Amsterdam, Elsevier, Developments in Water Science, v. 50, p. 327–334.

Piper, A.M., 1944, A graphic procedure in the geochemical interpretation of water analyses: Transactions, American Geophysical Union, v. 25, p. 914–923.

Plummer, L.N., Bexfield, L.M., Anderholm, S.K., Sanford, W.E., and Busenberg, Eurybiades, 2004, Geochemical characterization of ground-water flow in the Santa Fe Group aquifer system, Middle Rio Grande Basin, New Mexico: U.S. Geological Survey Water-Resources Investigation Report 03–4131, 414 p.

QGIS Development Team, 2019, QGIS Geographic Information System: Open Source Geopspatial Foundation. http://qgis.osgeo.org

Reiter, M., 2001, Using precision temperature logs to estimate horizontal and vertical groundwater flow components: Water Resources Research, v. 37, no. 3, p. 663-674.

Reiter, M., 2005, Possible ambiguities in subsurface temperature logs: Consideration of ground-water flow and ground surface temperature change: Pure and Applied Geophysics, v. 162, no. 2, p. 343-355.

Révész, Kinga, and Coplen, T.B., 2008A, Determination of the δ^2H of water: RSIL lab code 1574, chap. C1 of Révész, Kinga, and Coplen, T.B., eds., Methods of the Reston Stable Isotope Laboratory: U.S. Geological Survey Techniques and Methods, book 10, chap. C1, 27 p.

Révész, Kinga, and Coplen, T.B., 2008B, Determination of the $\delta^{18}O$ of water: RSIL lab code 489, chap. C2 of Révész, Kinga, and Coplen, T.B., eds., Methods of the Reston Stable Isotope Laboratory: U.S. Geological Survey Techniques and Methods, book 10, chap. C2, 28 p.

Richards, L.A., ed., 1954, Diagnosis and improvement of saline and alkali soils: U.S. Department of Agriculture, Agriculture Handbook 60, 160 p.

Ritterbusch, F., S. Ebser, J. Welte, T. Reichel, A. Kersting, R. Purtschert, W. Aeschbach-Hertig, and M. K. Oberthaler, 2014, Groundwater dating with Atom Trap Trace Analysis of ^{39}Ar, Geophysical Research Letters, 41, p. 6758–6764, doi:10.1002/2014GL061120.

Seager, W. R., 1981, Geology of the Organ Mountains and southern San Andres Mountains, New Mexico: New Mexico Bureau of Mines and Mineral Resources, Memoir 36, 97 p.

Seager, W. R., 1995, Geology of southwest quarter of Las Cruces and northwest El Paso 1º x 2º sheets: New Mexico Bureau of Mines and Mineral Resources, Geologic Map 60, scale 1:125,000.

Seager, W. R. and Mack, G. H., 1994, Geology of the East Potrillo Mountains and vicinity, Doña Ana County, New Mexico: New Mexico Bureau of Mines and Mineral Resources, Bulletin 113, 27 p.

Seager, W. R. and Morgan, P., 1979, Rio Grande rift in southern New Mexico, west Texas and northern Chihuahua, *in* Riecker, R. E., ed., Rio Grande rift, tectonics and magmatism: Washington D.C., American Geophysical Union, p. 87-106.

Seager, W. R., Hawley, J. W., Kottlowski, F. E. and Kelley, S.A., 1987, Geologic map of east half of Las Cruces and northeast El Paso 1º x 2º sheets, New Mexico: New Mexico Bureau of Mines and Mineral Resources, Geologic Map, GM-57, scale 1:125,000, 3 sheets.

Sheng, Z., 2013, Impacts of groundwater pumping and climate variability on groundwater availability in the Rio Grande Basin: Ecosphere, v. 4, no. 1, p. 1-25.

Šrámek, O., Stevens, L., McDonough, W. F., Mukhopadhyay, S., & Peterson, R. J., 2017. Subterranean production of neutrons, ^{39}Ar and ^{21}Ne: Rates and uncertainties. Geochimica et Cosmochimica Acta,v. *196*, p. 370-387.

Sweetkind, D.S., 2017, Three-dimensional hydrogeologic framework model of the Rio Grande transboundary region of New Mexico and Texas, USA, and northern Chihuahua, Mexico: U.S. Geological Survey Scientific Investigations Report 2017-5060, 49 p.

Szynkiewicz, A., Borrok, D.M., Ganjegunte, G.K., Skrzypek, G., Ma, L., Rearick, M.S., and Perkins, G.B., 2015, Isotopic studies of the Upper and Middle Rio Grande. Part 2—Salt loads and human impacts in south New Mexico and west Texas: Chemical Geology, v. 411, p. 336-350.

Szynkiewicz, A., Ewing, R.C., Moore, C.H., Glamoclija, M., Bustos, D., and Pratt, L.M., 2010, Origin of terrestrial gypsum dunes—Implications for Martian gypsum-rich dunes of Olympia Undae: Geomorphology, v. 121, no. 1-2, p. 69-83.

Szynkiewicz, A., Newton, B.T., Timmons, S.S., and Borrok, D.M., 2012, The sources and budget for dissolved sulfate in a fractured carbonate aquifer, southern Sacramento Mountains, New Mexico, USA: Applied geochemistry, v. 27, no. 8, p. 1451-1462.

Szynkiewicz, A., Witcher, J.C., Modelska, M., Borrok, D.M., and Pratt, L.M., 2011, Anthropogenic sulfate loads in the Rio Grande, New Mexico (USA): Chemical Geology, v. 283, no. 3-4, p. 194-209.

Tetra Tech EM Inc., 2004, Final Report for Well Installation Activities Within the Mesilla Valley Lower Rio Grande Basin: Consultant's report for New Mexico Interstate Stream Commission, 8 p.

Teeple, A.P., 2017, Geophysics- and geochemistry-based assessment of the geochemical characteristics and groundwater-flow system of the U.S. part of the Mesilla Basin/Conejos-Médanos aquifer system in Doña Ana County, New Mexico, and El Paso County, Texas, 2010–12: U.S. Geological Survey Scientific Investigations Report 2017–5028, 183 p.

Toth, J., 1963, A theoretical analysis of groundwater flow in small drainage basins, Journal of Geophysics Research, 68, p. 4795-4812.

Tucker, B.J., and Workman, S.M., 2013, Evaluation of Uranium Measurements in Water by Various Methods-13571: Waste Management Symposia, Tempe, AZ, 11 p.

U.S. Geological Survey, variously dated, National field manual for the collection of water-quality data: U.S. Geological Survey Techniques of Water-Resources Investigations, book 9, chaps. A1–A9.

U.S. Geological Survey, 2019, USGS water data for the Nation: U.S. Geological Survey National Water Information System database, accessed March 20, 2019, at https://doi.org/10.5066/F7P55KJN.

United States Environmental Protection Agency, 2007, Method 3051A Microwave Assisted Acid Digestion of Sediments, Sludges, Soils, and Oils, 30 p.

Williams, A.J., Crossey, L.J., Karlstrom, K.E., Newell, D., Person, M., and Woolsey, E., 2013, Hydrogeochemistry of the Middle Rio Grande aquifer system—Fluid mixing and salinization of the Rio Grande due to fault inputs: Chemical Geology, v. 351, p. 281-298.

Williams, R.T., Goodwin, L.B., Mozley, P.S., Beard, B.L., and Johnson, C.M., 2015, Tectonic controls on fault zone flow pathways in the Rio Grande rift, New Mexico, USA: Geology, v. 43, no. 8, p. 723-726.

Wilson, C.A., White, R.R., Orr, B.R., and Roybal, R.G., 1981, Water resources of the Rincon and Mesilla Valleys and adjacent areas: New Mexico State Engineer Technical Report 43, 514 p.

Witcher, J.C., King, J.P., Hawley, J.W., Kennedy, J.F., Williams, J., Cleary, M., and Bothern, L.R., 2004, Sources of salinity in the Rio Grande and Mesilla Basin groundwater: New Mexico Water Resources Research Institute Technical Completion Report 330, 184 p.

Yokochi, R., Sturchio, N., Purtschert, R., Jiang, W., Lu, Z.-T., Mueller, P., Yang, G.-M., Kennedy, B., and Kharaka, Y., 2013, Noble gas radionuclides in Yellowstone geothermal gas emissions: A reconnaissance: Chemical Geology, v. 339, p. 43-51.

Zappala, J.C., 2017, Atom Trap Trace Analysis: Developments & Applications: Chicago, IL, The University of Chicago, PhD Dissertation, 173 p.

Zappala, J.C., 2019, Email correspondence regarding krypton separation methodology, Argonne National Laboratory.

10. Appendices

10.1 Appendix A Data Tables

Table 5. Well site ID and well screen information. Data collected by the U.S. Geological Survey (USGS) for this study are available in the National Water Information System (https://doi.org/10.5066/F7P55KJN; U.S. Geological Survey, 2019) using the USGS Site ID. [m, meters]

Well Cluster	Well Site	USGS Site ID	Sample Date (mm/dd/yyyy)	Longitude	Latitude	Hole Depth (m)	Depth to top of screen interval (m)	Depth to bottom of screen interval (m)
ISC-1	ISC-1A	315940106372301	09/18/2016	-106.623056	31.994444	30.48	18.29	24.38
	ISC-1B	315940106372302	09/19/2016	-106.623056	31.994444	420.62	85.34	91.44
	ISC-1C	315940106372303	09/19/2016	-106.623056	31.994444	420.62	237.74	243.84
	ISC-1D	315940106372304	09/21/2016	-106.623056	31.994444	420.62	390.14	396.24
ISC-4	ISC-4A	314817106325801	09/20/2016	-106.549989	31.804829	23.77	15.24	21.34
	ISC-4B	314817106325802	09/20/2016	-106.549989	31.804829	54.86	41.06	47.15
ISC-7	ISC-7A	315245106380601	02/27/2017	-106.635547	31.879271	152.4	50.96	57.059
	ISC-7B	315245106380602	02/27/2017	-106.635547	31.879271	152.4	120.73	126.83
LC-2	LC-2A	315754106372401	09/13/2016	-106.823061	32.295927	95.71	91.44	92.96
	LC-2B	315754106372402	09/15/2016	-106.823061	32.295927	36.27	30.48	32.00
	LC-2C	315754106372403	09/12/2016	-106.823061	32.295927	12.19	9.14	10.67
	LC-2F	315754106372404	09/18/2016	-106.823061	32.296205	278.89	192.02	195.07
LMV-2	LMV-2A	320141106390601	02/25/2017	-106.652216	32.028156	701.04	207.26	210.31
	LMV-2B	320141106390602	03/01/2017	-106.652216	32.028156	701.04	566.93	569.98
M-2	M-2A	321241106461601	02/24/2017	-106.771669	32.211485	97.54	94.18	95.71
	M-2B	321241106461602	02/24/2017	-106.771669	32.211485	37.19	33.53	35.05
	M-2C	321241106461603	02/23/2017	-106.771669	32.211485	15.85	12.19	13.72
None	ISC-2A	315754106372401	03/25/2009	-106.6239	31.965083	24.38	15.24	21.34
	Afton Power Plant Well	320654106504201	07/31/2018	-106.845358	32.115215	333.76	210.31	327.66
	Well 68	322526106423101	10/30/2018	-106.708583	32.423833	313.94	Unknown	Unknown

Table 6. Temperature, pH, alkalinity, total dissolved solids, and specific conductance of groundwater samples. Data collected by the USGS in 2016, 2017, and 2018 (see table 5 for sample dates) are available in the National Water Information System (U.S. Geological Survey, 2019).

Well Site	Temperature, water (degrees Celsius)	pH, water, unfiltered, field (standard units)	Alkalinity, water, filtered, inflection-point method, field (mg/L as CaCO3)	Total Dissolved Solids (mg/L)	Specific Conductance, field (µS/cm at 25 degrees Celsius)
ISC-1A	20.5	7.5	448	2,040	3,080
ISC-1B	23.5	7.4	283	1,160	1,980
ISC-1C	23.8	8.4	61	282	441
ISC-1D	24.5	8.5	70	291	470
ISC-4A	21.5	7.3	432	16,300	22,100
ISC-4B	21.5	7.3	194	29,700	42,600
ISC-7A	24.6	7.3	865	1,500	2,290
ISC-7B	30.0	7.1	816	3,390	5,550
LC-2A	20.2	7.5	173	634	1,020
LC-2B	22.8	7.6	164	577	920
LC-2C	25.0	7.6	161	498	801
LC-2F	22.5	7.7	132	288	469
LMV-2A	20.3	8.0	227	541	815
LMV-2B	20.2	8.7	138	949	1,640
M-2A	17.4	7.9	152	405	662
M-2B	19.0	7.5	191	715	1,110
M-2C	21.2	7.8	165	569	906

Table 7. $^{87}Sr/^{86}Sr$, $\delta^{13}C$, $\delta^{34}S$ of groundwater samples. Data collected by the USGS in 2016, 2017, and 2018 (see table 5 for sample dates) are available in the National Water Information System (U.S. Geological Survey, 2019). $\delta^{34}S$ data provided by Szynkiewcz et al. (2011). [nd, no data]

Well Site	$^{87}Sr/^{86}Sr$, water, filtered	$\delta^{13}C$, water, unfiltered (per mil)	$\delta^{34}S$, water, filtered (per mil)	Sample date for $\delta^{34}S$ (mm/dd/yyyy)
ISC-1A	0.7114	-13.55	2.28	02/09/2007
ISC-1B	0.7100	-5.65	5.76	02/09/2007
ISC-1C	0.7105	-8.70	2.89	02/09/2007
ISC-1D	0.7105	-7.90	3.83	02/09/2007
ISC-4A	0.7100	-13.74	12.36	02/13/2007
ISC-4B	0.7096	-11.58	12.46	02/13/2007
ISC-7A	0.7089	-3.88	8.01	02/12/2007
ISC-7B	0.7086	-6.35	9.52	02/12/2007
LC-2A	0.7098	-7.79	nd	nd
LC-2B	0.7099	-7.81	nd	nd
LC-2C	0.7105	-7.89	nd	nd
LC-2F	0.7096	-7.30	nd	nd
LMV-2A	0.7095	-6.45	nd	nd
LMV-2B	0.7106	-4.73	nd	nd
M-2A	0.7098	-9.61	nd	nd
M-2B	0.7095	-8.67	nd	nd
M-2C	0.7105	-7.60	nd	nd

Table 8. Interpreted depth from bedrock and alluvial thickness of Mesilla Valley wells based on Hawley (2020, Fig. 21). [m, meters]

Well Site	Depth Difference from bottom of Well Screen to Bedrock (m)	Alluvial Thickness (m)
ISC-1A	730	754
ISC-1B	663	754
ISC-1C	511	754
ISC-1D	358	754
ISC-4A	52	73
ISC-4B	26	73
ISC-7A	345	402
ISC-7B	276	402
LC-2A	486	579
LC-2B	547	579
LC-2C	568	579
LC-2F	384	579
LMV-2A	668	878
LMV-2B	308	878
M-2A	563	658
M-2B	623	658
M-2C	645	658

Table 9. Interpreted depth from bedrock and alluvial thickness of additional northern Mesilla Valley wells. [m, meters; mg/L, milligrams per liter]

Well Site	Latitude	Longitude	Source	Depth Difference from Well Screen to Bedrock (m)	Alluvial Thickness (m)	Total Dissolved Solids (mg/L)
Leasburg State Park Well	32.4917	-106.9184	Witcher et al. (2004)	40	12	2330
Fort Seldon State Park Well	32.4827	-106.9213	Witcher et al. (2004)	40	12	510
22S.01E.05.142 322537106515201	32.427	-106.865	USGS (2019)	220	134	529

Table 10. Sample locations of gypsum samples analyzed for $\delta^{34}S$. [VCDT, Vienna-Canyon Diablo Troilite]

Sample Formation	Latitude	Longitude	$\delta^{34}S$, Gypsum (VCDT)
Rincon Valley Formation	32.6773	-106.0734	7.9
Mesilla Valley Shale	31.795	-106.5450	-24.1
Lake Lucero	32.6974	-106.4496	12.5

Table 11. $\delta^{18}O$, δD, ^{14}C, and tritium of groundwater samples. Negative tritium values are a result of analytical error and are equivalent to zero pCi/L. Data collected by the USGS in 2016, 2017, and 2018 (see table 5 for sample dates) are available in the National Water Information System (U.S. Geological Survey, 2019).
[pMC, percent modern carbon; pCi/L, picocuries per liter; R, nondetect]

Well Site	δD, water, unfiltered (per mil)	$\delta^{18}O$, water, unfiltered (per mil)	^{14}C, non-normalized, water, filtered (pMC)	Tritium water, unfiltered (pCi/L)
ISC-1A	-69.27	-8.26	102	11.0
ISC-1B	-83.50	-11.08	11.0	R 0.10
ISC-1C	-84.19	-11.29	8.20	R -0.03
ISC-1D	-84.83	-11.36	8.41	R 0.08
ISC-4A	-64.16	-8.06	89.9	2.39
ISC-4B	-68.76	-8.18	68.3	0.24
ISC-7A	-88.30	-11.96	0.890	R 0.02
ISC-7B	-71.96	-9.44	0.090	R 0.10
LC-2A	-65.87	-7.69	96.7	13.1
LC-2B	-65.46	-7.70	96.8	11.9
LC-2C	-68.41	-8.30	96.7	13.5
LC-2F	-89.25	-11.71	74.8	R 0.15
LMV-2A	-86.78	-11.32	15.3	R -0.15
LMV-2B	-88.28	-11.83	0.170	R 0.16
M-2A	-87.37	-11.28	88.0	1.37
M-2B	-71.06	-8.47	113	18.4
M-2C	-67.86	-7.98	112	12.4

Table 12. U-Series of groundwater samples. Data collected by the USGS in 2016, 2017, and 2018 (see table 5 for sample dates) are available in the National Water Information System (U.S. Geological Survey, 2019).
[pCi/L, picocuries per liter; µg/L, micrograms per liter; R, nondetect; nd, no data]

Well Site	^{238}U, water, filtered (pCi/L)	^{234}U, water, filtered (pCi/L)	^{235}U, water, filtered (pCi/L)	Uranium, water, filtered (µg/L)	^{234}U/^{238}U
ISC-1A	0.41	0.72	R 0.016	1.12	1.8
ISC-1B	0.65	1.94	0.053	2.08	3.0
ISC-1C	0.08	0.08	0.013	0.100	1.0
ISC-1D	nd	nd	nd	0.11	nd
ISC-4A	1.46	2.4	0.12	4.65	1.6
ISC-4B	38	60	2.1	112	1.6
ISC-7A	6.2	9.5	0.31	17.7	1.5
ISC-7B	9.1	11.9	0.43	28.2	1.3
LC-2A	0.40	0.47	R 0.008	0.820	1.2
LC-2B	0.12	0.12	0.026	0.350	1.0
LC-2C	0.033	0.22	R 0.011	0.250	6.7
LC-2F	0.028	0.12	R 0.007	0.060	4.3
LMV-2A	0.08	0.32	R 0.007	0.188	4.0
LMV-2B	R 0.003	0.019	0.013	nd	6.3
M-2A	0.73	2.1	0.05	2.33	2.9
M-2B	0.24	0.57	R 0.006	0.653	2.4
M-2C	0.10	0.22	0.017	0.334	2.2

Table 13. Noble gas concentrations of groundwater samples. Data collected by the USGS in 2016, 2017, and 2018 (see table 5 for sample dates) are available in the National Water Information System (U.S. Geological Survey, 2019). [ccSTP/gH2O, cubic centimeters at standard temperature and pressure per gram of water; CO2 INF, Nitrogen could not be accurately measured due to excess carbon dioxide; <, less than]

Well Site	Kr 10^{-8} ccSTP/g (H2O)	Xe 10^{-9} ccSTP/g (H2O)	N_2 10^{-2} ccSTP/g (H2O)	^{4}He 10^{-8} ccSTP/g (H2O)	Ne 10^{-7} ccSTP/g (H2O)	Ar 10^{-4} ccSTP/g (H2O)	CH_4 10^{-5} ccSTP/g (H2O)
ISC-1A	6.797	8.962	1.897	6.767	2.015	3.105	< 1.0
ISC-1B	6.792	9.327	1.202	76.29	1.677	2.961	< 1.0
ISC-1C	7.022	9.621	1.153	12.94	1.701	3.029	< 1.0
ISC-1D	6.918	9.675	1.181	10.48	1.704	3.005	< 1.0
ISC-4A	6.192	8.271	CO2 INF	107.9	1.714	2.796	< 1.0
ISC-4B	5.663	7.380	1.087	95.1	1.578	2.524	< 1.0
ISC-7A	6.783	9.494	CO2 INF	330.0	1.814	3.039	< 1.0
ISC-7B	3.796	5.159	CO2 INF	1,900	1.088	1.803	< 1.0
LC-2A	6.357	8.483	1.271	4.642	1.868	2.890	< 1.0
LC-2B	6.789	8.749	1.349	5.893	2.309	3.224	< 1.0
LC-2C	6.633	8.624	1.380	6.906	2.600	3.179	< 1.0
LC-2F	7.129	9.829	1.252	4.144	1.664	3.049	< 1.0
LMV-2A	6.913	9.480	1.114	8.862	1.686	3.059	< 1.0
LMV-2B	6.961	9.431	1.220	318.9	1.778	3.094	< 1.0
M-2A	6.866	9.485	1.156	4.340	1.759	3.076	< 1.0
M-2B	7.138	9.639	1.574	5.095	2.068	3.294	< 1.0
M-2C	6.038	7.680	1.271	5.854	2.307	2.953	< 1.0

Table 14. Noble gas ratios of groundwater samples. Data collected by the USGS in 2016, 2017, and 2018 (see table 5 for sample dates) are available in the National Water Information System (U.S. Geological Survey, 2019).
[R/Ra, the 3He/4He signatures of the groundwater sample and atmosphere]

Well Site	R/Ra	$^{20}Ne/^{22}Ne$	$^{40}Ar/^{36}Ar$	$^{86}Kr/^{84}Kr$	$^{130}Xe/^{132}Xe$
ISC-1A	1.284	9.876	303.3	0.306	0.145
ISC-1B	1.759	9.795	296.2	0.304	0.146
ISC-1C	1.375	9.840	295.8	0.305	0.146
ISC-1D	1.264	9.799	296.5	0.305	0.146
ISC-4A	0.365	9.819	296.7	0.305	0.146
ISC-4B	0.246	9.776	295.5	0.306	0.145
ISC-7A	2.945	9.816	297.8	0.306	0.147
ISC-7B	2.917	9.913	319.9	0.305	0.151
LC-2A	1.093	9.842	296.7	0.306	0.147
LC-2B	1.026	9.790	296.2	0.306	0.148
LC-2C	0.988	9.805	296.1	0.304	0.146
LC-2F	1.210	9.793	296.0	0.305	0.147
LMV-2A	1.242	9.851	295.9	0.305	0.149
LMV-2B	0.263	9.845	296.6	0.306	0.150
M-2A	1.070	9.827	295.8	0.306	0.147
M-2B	2.929	9.822	296.2	0.305	0.149
M-2C	0.999	9.813	295.6	0.305	0.150

Table 15. Major cations of groundwater samples. Data collected by the USGS in 2016, 2017, and 2018 (see table 5 for sample dates) are available in the National Water Information System (U.S. Geological Survey, 2019).
[mg/L, milligrams per liter]

Well Site	Calcium, water, filtered (mg/L)	Magnesium, water, filtered (mg/L)	Sodium, water, filtered (mg/L)	Potassium, water, filtered (mg/L)
ISC-1A	113	46.5	536	23.7
ISC-1B	78.7	26.1	292	9.38
ISC-1C	13.4	0.573	76.8	2.84
ISC-1D	10.1	0.231	88.2	2.12
ISC-4A	593	288	4,590	24.5
ISC-4B	987	805	8,480	37.0
ISC-7A	27.0	42.6	487	8.25
ISC-7B	58.8	23.5	1,190	6.98
LC-2A	86.1	13.1	110	4.98
LC-2B	69.6	11.8	109	5.27
LC-2C	62.1	11.9	86.9	7.60
LC-2F	42.1	6.71	45.8	2.90
LMV-2A	26.5	6.71	150	3.83
LMV-2B	7.72	0.912	332	3.00
M-2A	58.2	9.67	66.4	3.98
M-2B	121	18.3	89.4	5.12
M-2C	64.0	10.4	114	5.07

Table 16. Major anions of groundwater samples. Data collected by the USGS in 2016, 2017, and 2018 (see table 5 for sample dates) are available in the National Water Information System (U.S. Geological Survey, 2019). [mg/L, milligrams per liter; <, less than; E, estimated]

Well Site	Bicarbonate, water, filtered, inflection-point titration method, field (mg/L)	Chloride, water, filtered (mg/L)	Sulfate, water, filtered (mg/L)	Fluoride, water, filtered (mg/L)	Bromide, water, filtered (mg/L)
ISC-1A	540	393	614	0.46	0.456
ISC-1B	344	339	202	0.58	0.255
ISC-1C	73	44.0	72.6	0.82	0.064
ISC-1D	83	43.9	77.0	0.73	0.062
ISC-4A	523	5,390	5,090	< 0.25	3.78
ISC-4B	236	14,100	5,100	< 0.50	8.81
ISC-7A	1,050	74.1	274	0.70	0.249
ISC-7B	992	703	854	0.65	0.640
LC-2A	210	109	178	0.41	0.211
LC-2B	199	97.8	157	0.51	0.145
LC-2C	195	68.1	140	0.71	E 0.127
LC-2F	160	38.4	46.9	0.45	0.058
LMV-2A	274	47.3	124	0.43	0.067
LMV-2B	160	240	259	4.85	0.274
M-2A	184	57.0	93.0	0.33	0.090
M-2B	231	117	223	0.32	0.195
M-2C	201	88.2	159	0.61	0.147

Table 17. Trace ions of groundwater samples. Data collected by the USGS in 2016, 2017, and 2018 (see table 5 for sample dates) are available in the National Water Information System (U.S. Geological Survey, 2019).
[µg/L, micrograms per liter; <, less than; nd, no data]

Well Site	Thallium, water, filtered (µg/L)	Molybdenum, water, filtered (µg/L)	Vanadium, water, filtered (µg/L)	Selenium, water, filtered (µg/L)	Barium, water, filtered (µg/L)	Beryllium, water, filtered, (µg/L)	Boron, water, filtered (µg/L)	Cadmium, water, filtered (µg/L)	Chromium, water, filtered (µg/L)	Cobalt, water, filtered (ug/L)
ISC-1A	< 0.040	17.0	< 0.20	< 0.10	34.0	< 0.020	514	0.060	<1.0	0.110
ISC-1B	< 0.060	17.9	< 0.30	< 0.15	27.9	< 0.030	297	< 0.090	< 1.5	0.360
ISC-1C	< 0.020	4.90	< 0.10	< 0.05	15.8	< 0.010	80	< 0.030	< 0.50	< 0.030
ISC-1D	< 0.020	5.70	< 0.10	< 0.05	3.83	< 0.010	86	< 0.030	< 0.50	0.040
ISC-4A	< 0.300	22.9	< 1.5	< 0.75	15.3	< 0.150	3,070	< 0.450	< 7.5	< 0.450
ISC-4B	< 0.400	2.78	5.1	< 1.0	12.5	< 0.200	2,810	< 0.600	< 10.0	0.680
ISC-7A	nd	nd	nd	nd	nd	nd	980	nd	nd	nd
ISC-7B	< 0.080	19.7	<1.2	< 0.60	16.7	< 0.040	1,680	< 0.120	< 6.0	< 0.360
LC-2A	< 0.060	7.35	< 0.30	< 0.15	130	< 0.030	213	< 0.090	< 1.5	< 0.090
LC-2B	< 0.060	7.24	< 0.30	< 0.15	111	< 0.030	200	< 0.090	< 1.5	0.380
LC-2C	< 0.060	6.84	< 0.30	< 0.15	98.6	< 0.030	138	< 0.090	< 1.5	0.090
LC-2F	< 0.020	3.19	< 0.10	< 0.05	89.7	< 0.010	75	< 0.030	< 0.50	< 0.030
LMV-2A	< 0.020	13.2	< 0.10	< 0.05	51.2	< 0.010	139	< 0.030	0.50	0.561
LMV-2B	nd	nd	nd	nd	nd	nd	790	nd	nd	nd
M-2A	< 0.020	5.58	0.30	0.15	49.7	< 0.010	81	< 0.030	< 0.50	0.041
M-2B	< 0.020	6.51	< 0.10	< 0.05	114	< 0.010	98	< 0.030	< 0.50	0.080
M-2C	< 0.020	8.37	0.17	0.05	89.3	< 0.010	186	< 0.030	< 0.50	0.103

Table 17 (continued). Trace ions of groundwater samples. Data collected by the USGS in 2016, 2017, and 2018 (see table 5 for sample dates) are available in the National Water Information System (U.S. Geological Survey, 2019). [µg/L, micrograms per liter; mg/L, milligrams per liter; <, less than; nd, no data]

Well Site	Copper, water, filtered (µg/L)	Iron, water, filtered (µg/L)	Lead, water, filtered (µg/L)	Man-ganese, water, filtered (µg/L)	Nickel, water, filtered (µg/L)	Silver, water, filtered (µg/L)	Stron-tium, water, filtered (µg/L)	Zinc, water, filtered (µg/L)	Anti-mony, water, filtered (µg/L)	Alu-minum, water, filtered (µg/L)	Lith-ium, water, filtered (µg/L)	Silica, water, filtered (mg/L as silica)
ISC-1A	< 0.40	437	< 0.040	370	0.83	< 2.00	2,920	4.2	0.07	< 6.0	419	41.7
ISC-1B	< 0.60	68.6	< 0.060	31.8	< 0.60	< 3.00	2,150	< 6.0	< 0.090	< 9.0	275	43.5
ISC-1C	< 0.20	8.5	< 0.020	7.51	< 0.20	< 1.00	174	< 2.0	0.04	< 3.0	33.2	34.3
ISC-1D	< 0.20	6.5	0.02	4.38	< 0.20	< 1.00	80.3	< 2.0	0.03	7.4	42.4	26
ISC-4A	< 3.0	2,090	< 0.300	1,760	< 3.0	< 15.0	16,600	< 30.0	< 0.450	< 45.0	1,340	41.2
ISC-4B	5.4	487	< 0.400	3,030	5.8	< 20.0	24,600	< 40.0	< 0.600	< 60.0	2,280	16
ISC-7A	nd	101	nd	36.5	nd	nd	1,070	nd	nd	nd	nd	70.6
ISC-7B	< 2.4	224	0.487	23.8	< 2.4	< 4.00	1,230	49.8	< 0.120	< 12.0	1,040	63.5
LC-2A	< 0.60	12.2	0.13	520	0.63	< 3.00	1,030	< 6.0	< 0.090	< 9.0	88.4	26.6
LC-2B	< 0.60	7.2	< 0.060	463	1.3	< 3.00	803	< 6.0	< 0.090	< 9.0	91	25.6
LC-2C	< 0.60	412	< 0.060	383	< 0.60	< 3.00	771	< 6.0	< 0.090	< 9.0	97.7	22.7
LC-2F	< 0.20	50.1	0.02	102	< 0.20	< 1.00	412	< 2.0	< 0.030	< 3.0	71.1	24.3
LMV-2A	< 0.20	406	< 0.020	92.3	4.8	< 1.00	628	3.8	0.035	< 3.0	113	45.2
LMV-2B	nd	334	nd	119	nd	nd	470	nd	nd	nd	nd	18.8
M-2A	0.55	< 5.0	0.119	18.5	1.2	< 1.00	623	< 2.0	0.056	< 3.0	51.6	25
M-2B	0.25	11.2	< 0.020	385	0.64	< 1.00	1,300	2.9	< 0.030	< 3.0	67.8	25.4
M-2C	< 0.20	141	< 0.020	459	0.67	< 1.00	609	< 2.0	< 0.030	< 3.0	81.2	27.6

Table 18. ^{81}Kr, ^{85}Kr, and ^{39}Ar of groundwater samples.
[dpm/ccKr, decays per minute per cubic centimeter of Krypton at standard temperature and pressure; nd, no data; <, less than]

Date Sampled	Well Site	^{85}Kr Bern (dpm/ccKr)	Error	^{85}Kr Argonne (dpm/ccKr)	Error	^{39}Ar (pM)	Error
Fall 2016	LC-2A	52.2	2.2	nd	nd	103	8
Fall 2016	LC-2F	0.5	0.2	nd	nd	79	15
8/30/2017	ISC-1C	2.6	0.3	1.01	0.22	55	7
10/26/2017	ISC-4A	1.9	0.4	0.55	0.12	134	12
1/10/2018	ISC-7A	4.6	0.4	2.54	0.29	74	9
1/10/2018	LMV-2A	2	0.4	0.37	nd	66	9
6/5/2018	ISC-1D	nd	nd	0.63	nd	33	6
6/6/2018	ISC-4B	nd	nd	0.81	nd	132	13
8/1/2018	Afton Power Plant Well	< 1.2	nd	< 0.61	nd	< 8	nd
10/30/2018	Well 68	< 1.5	nd	nd	nd	48	7
10/30/2018	Well 68 (duplicate)	<1.3	nd	nd	nd	55	10

Table 19. PHREEQC saturation indices (SI) of groundwater samples.
[Percent error calculated as 100*(Cation-|Anion|)/(Cation+|Anion|); g, gas]

Well Site	Percent error	Anhy-drite	Arago-nite	Cal-cite	CH4(g)	Chalced-ony	Chryso-tile	CO2(g)	Dolo-mite	Fluo-rite	Gyp-sum	H2S(g)
ISC-1A	1.81	-1.20	0.31	0.46	-67.46	0.45	-3.46	-1.88	0.82	-1.75	-0.97	-67.31
ISC-1B	-0.12	-1.66	0.02	0.17	-67.15	0.43	-4.08	-1.94	0.18	-1.59	-1.44	-67.19
ISC-1C	1.25	-2.56	-0.23	-0.08	-76.81	0.31	-2.87	-3.56	-1.20	-1.83	-2.34	-77.50
ISC-1D	1.49	-2.67	-0.19	-0.05	-77.74	0.17	-3.64	-3.60	-1.40	-2.08	-2.44	-78.58
ISC-4A	-2.70	-0.22	0.44	0.58	-65.9	0.47	-2.97	-1.78	1.17	-2.14	0.00	-64.90
ISC-4B	-2.45	-0.16	0.28	0.43	-66.29	0.10	-2.25	-2.18	1.11	-1.54	0.06	-65.07
ISC-7A	5.55	-2.06	-0.11	0.03	-65.92	0.63	-3.66	-1.36	0.61	-1.99	-1.84	-66.24
ISC-7B	4.55	-1.43	-0.09	0.05	-64.89	1.47	-3.59	-1.19	0.10	-1.95	-1.23	-64.63
LC-2A	1.25	-1.59	-0.04	0.11	-67.8	0.25	-5.08	-2.26	-0.31	-1.72	-1.35	-67.69
LC-2B	0.81	-1.70	0.00	0.15	-69.07	0.21	-4.30	-2.36	-0.15	-1.64	-1.47	-69.13
LC-2C	0.76	-1.77	-0.01	0.14	-69.37	0.13	-4.09	-2.35	-0.10	-1.42	-1.55	-69.50
LC-2F	1.12	-2.31	-0.12	0.02	-70.00	0.19	-4.29	-2.54	-0.43	-1.86	-2.08	-70.54
LMV-2A	0.68	-2.17	0.11	0.26	-72.17	0.48	-2.43	-2.62	0.21	-2.15	-1.94	-72.80
LMV-2B	-0.58	-2.49	-0.05	0.10	-78.71	0.08	-1.87	-3.57	-0.44	-0.68	-2.26	-79.49
M-2A	1.31	-1.95	0.16	0.31	-71.05	0.26	-3.34	-2.71	0.09	-1.97	-1.70	-71.48
M-2B	0.15	-1.39	0.11	0.26	-67.6	0.25	-4.89	-2.23	-0.04	-1.81	-1.15	-67.43
M-2C	0.51	-1.73	0.16	0.30	-70.64	0.26	-3.40	-2.56	0.11	-1.50	-1.49	-70.87

Table 19 (continued). PHREEQC SI of groundwater samples. [d, disorganized; a, amorphous]

Well Site	Halite	O2(g)	Quartz	Sepiolite	Sepiolite(d)	SiO2(a)	Sulfur	Talc
ISC-1A	-5.32	-38.74	0.87	-1.6	-4.38	-0.41	-50.25	1.08
ISC-1B	-5.62	-38.1	0.84	-2.16	-5.02	-0.41	-50.29	0.46
ISC-1C	-7.03	-34	0.72	-1.57	-4.44	-0.54	-58.6	1.42
ISC-1D	-6.97	-33.36	0.58	-2.33	-5.22	-0.67	-59.47	0.4
ISC-4A	-3.4	-39.19	0.89	-1.29	-4.09	-0.38	-48.22	1.62
ISC-4B	-2.74	-39.2	0.52	-1.43	-4.24	-0.75	-48.39	1.6
ISC-7A	-6.08	-38.12	1.04	-1.59	-4.48	-0.21	-49.52	1.29
ISC-7B	-4.78	-37.13	1.86	-0.33	-3.36	0.65	-48.25	3.12
LC-2A	-6.51	-38.84	0.68	-3	-5.77	-0.6	-50.62	-0.94
LC-2B	-6.56	-37.54	0.62	-2.65	-5.5	-0.64	-51.83	-0.22
LC-2C	-6.81	-36.79	0.53	-2.73	-5.63	-0.71	-52.18	-0.14
LC-2F	-7.32	-37.24	0.6	-2.67	-5.5	-0.66	-53.05	-0.25
LMV-2A	-6.72	-36.81	0.9	-0.85	-3.63	-0.38	-54.73	2.17
LMV-2B	-5.7	-34.04	0.5	-1.15	-3.93	-0.78	-60.03	1.91
M-2A	-6.98	-38.23	0.69	-1.72	-4.42	-0.61	-53.65	0.77
M-2B	-6.57	-39.26	0.68	-2.83	-5.57	-0.61	-50.39	-0.78
M-2C	-6.58	-37.29	0.68	-1.91	-4.71	-0.6	-53.19	0.76

10.2 Appendix B Temperature Profiles

Plots and lithology provided by Dr. Shari Kelley (New Mexico Institute of Mining and Technology)

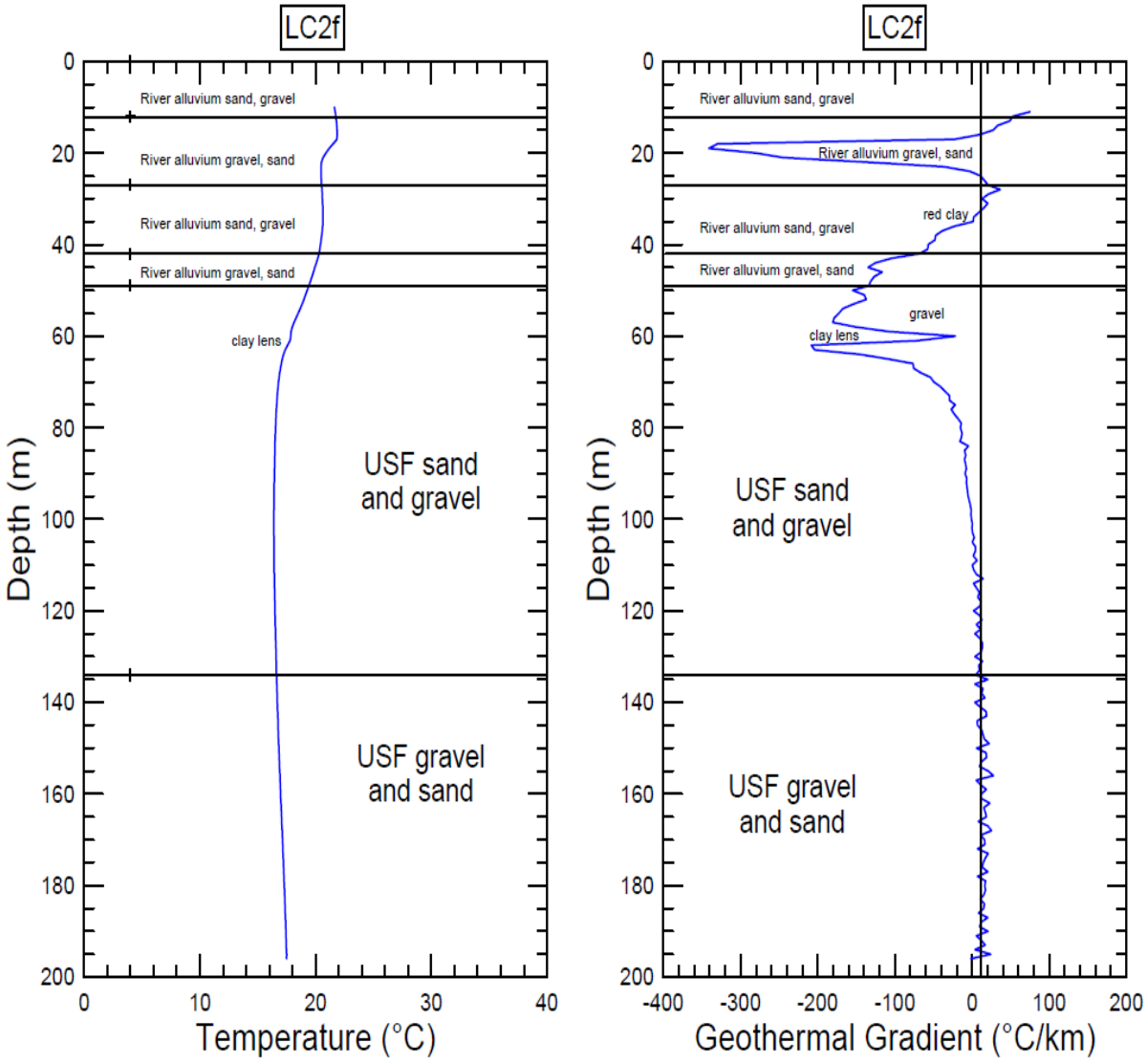

Figure 19. Temperature profile and temperature gradient of LC-2F
[USF, upper Santa Fe Group deposits]

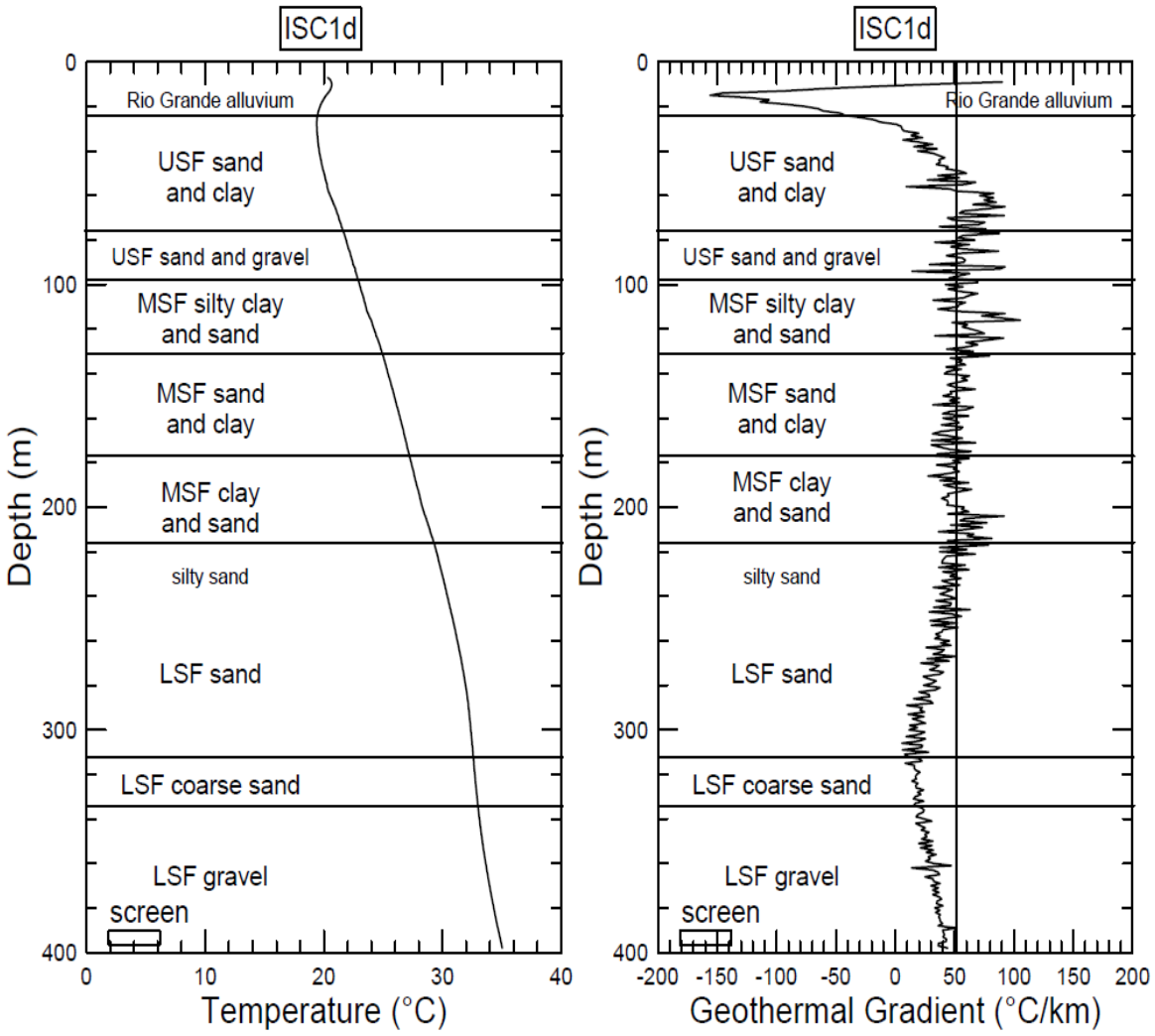

Figure 20. Temperature profile and temperature gradient of ISC-1D
[USF, upper Santa Fe Group deposits; MSF, middle Santa Fe Group deposits; LSF, lower Santa Fe Group deposits]

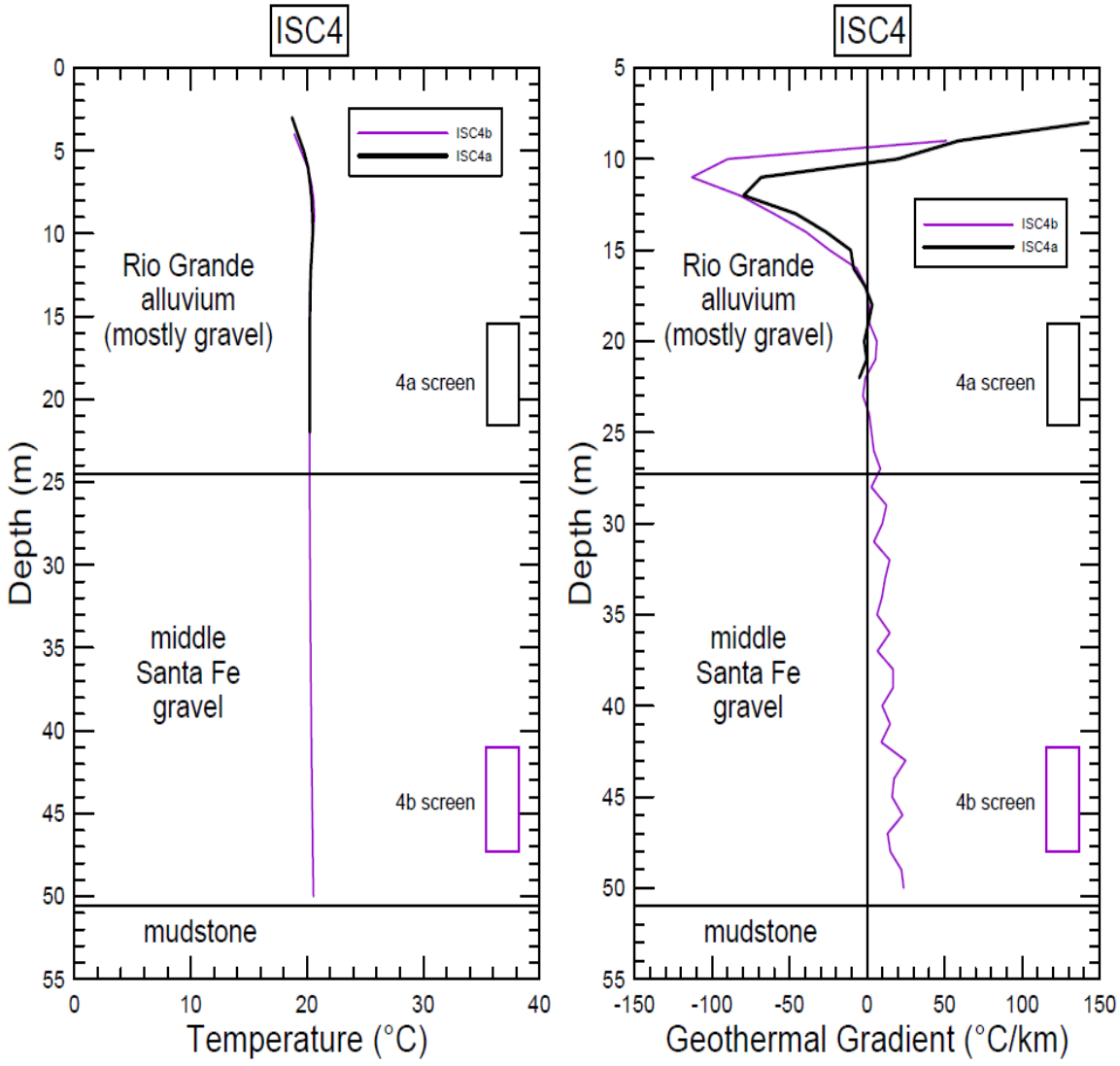

Figure 21. Temperature profile and temperature gradient of ISC-4A and ISC-4B

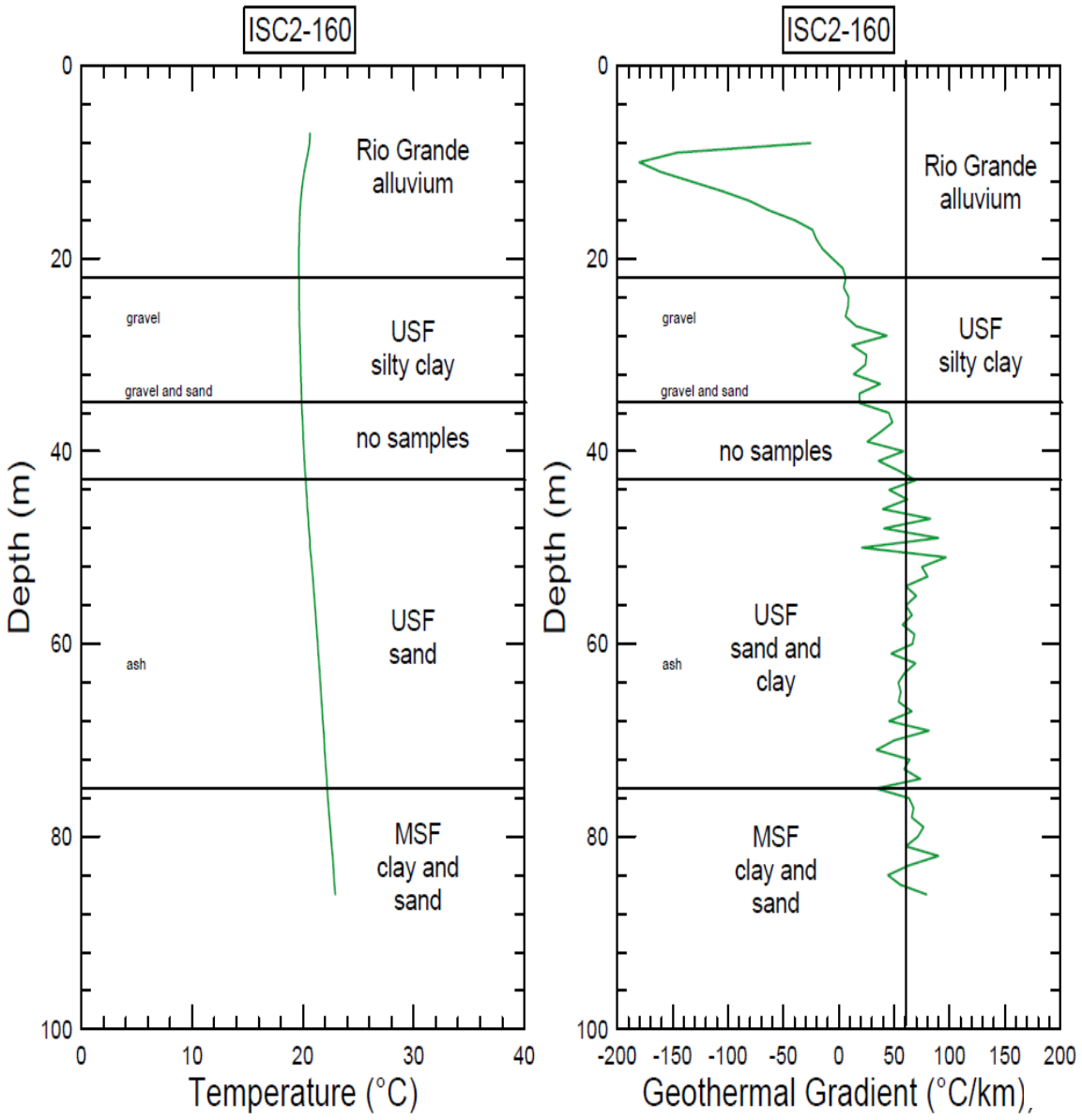

Figure 22. Temperature profile and temperature gradient of ISC-2A (also labeled 160)
[USF, upper Santa Fe Group deposits; MSF, middle Santa Fe Group deposits]

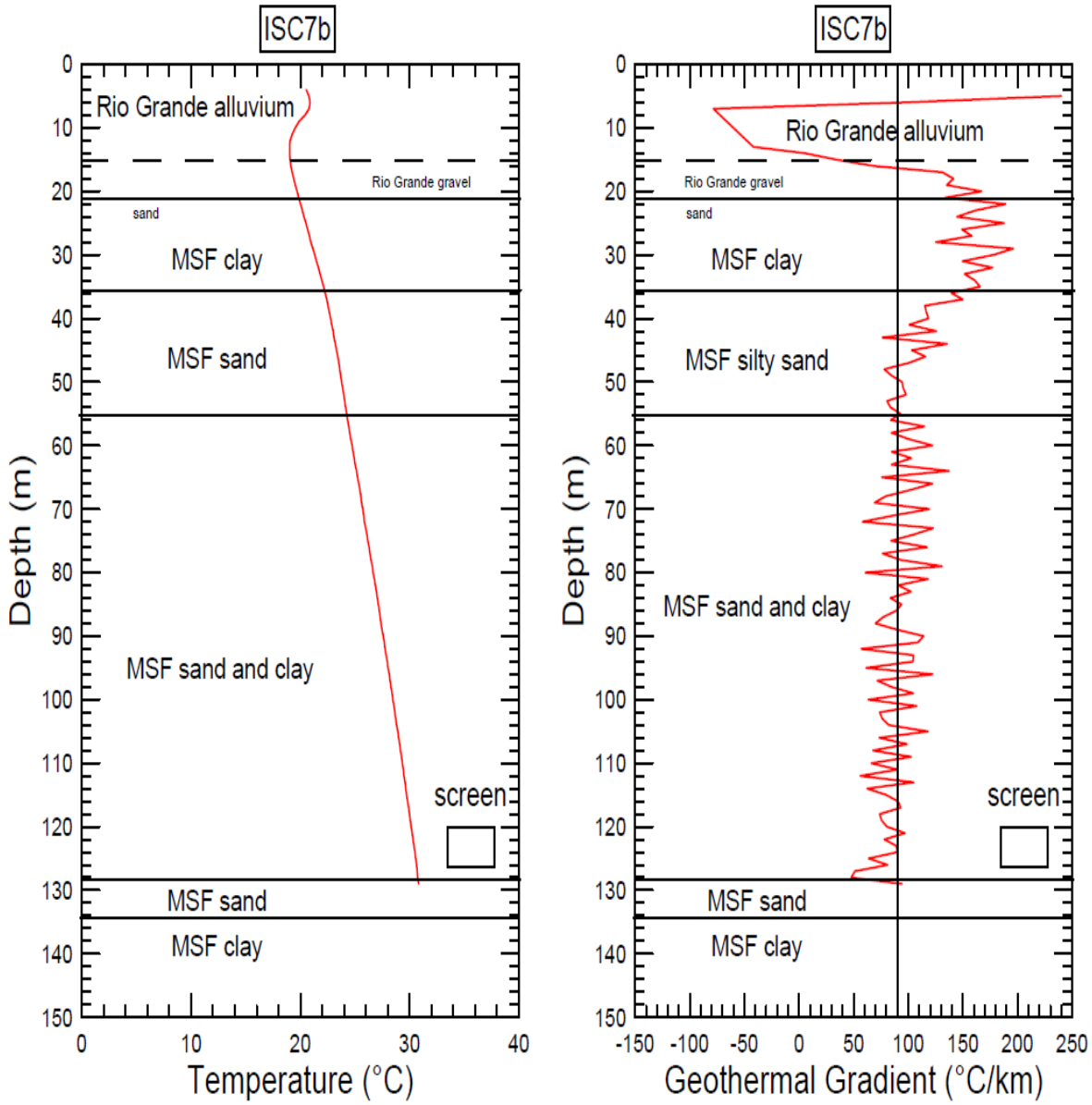

Figure 23. Temperature profile and temperature gradient of ISC-7B
[MSF, middle Santa Fe Group deposits]

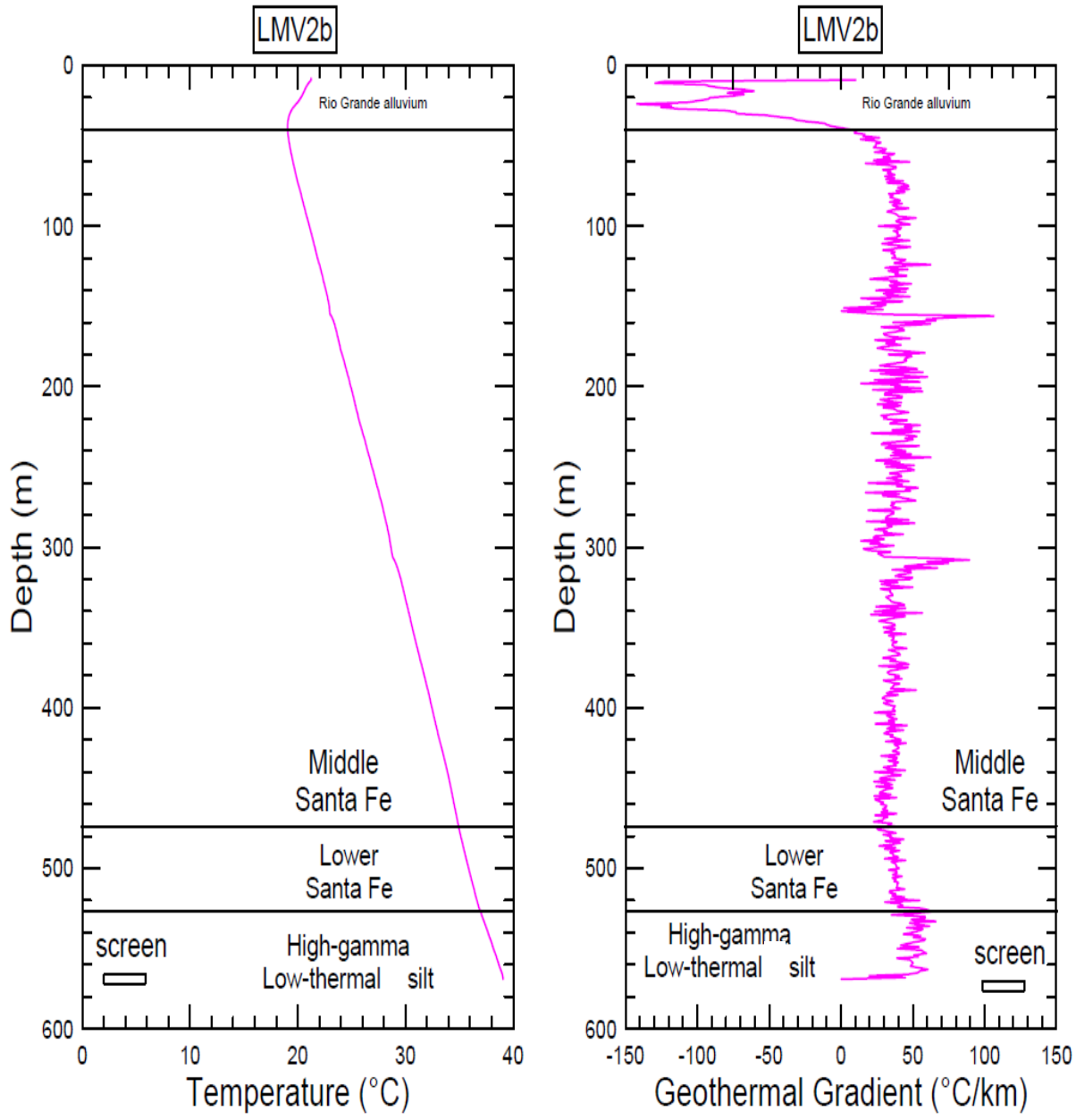

Figure 24. Temperature profile and temperature gradient of LMV-2B

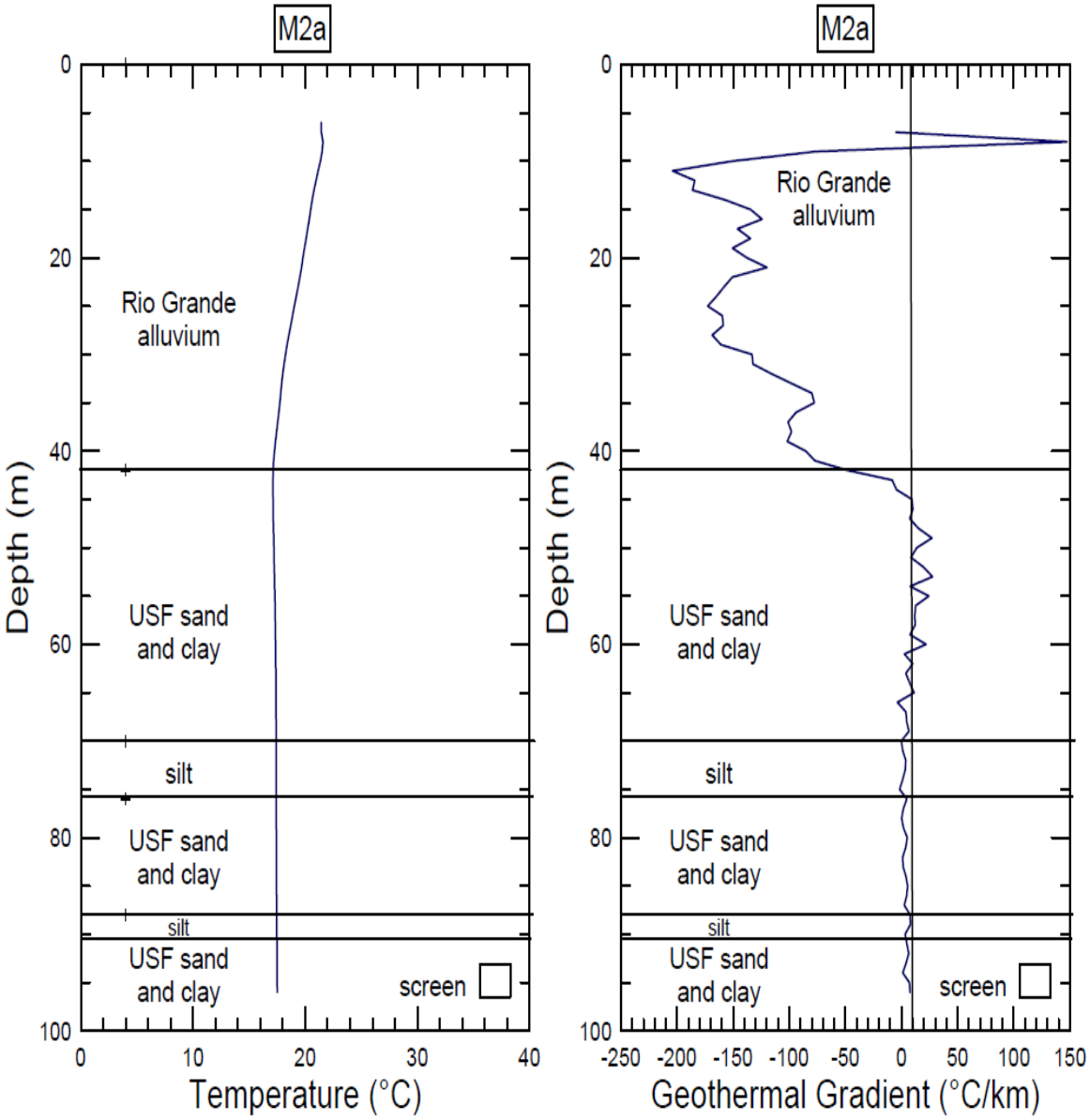

Figure 25. Temperature profile and temperature gradient of M-2A
[USF, upper Santa Fe Group deposits]

10.3 Appendix C Expanded Methodology

Between 2016 and 2018, standard USGS water quality constituents were measured in groundwater samples collected from various wells (Appendix A Table 5) throughout the Mesilla Valley, Mesilla basin, and the Jornada del Muerto (Fig. 1). The wells were used to obtain representative samples from different depths, zones, and lithologies of the inset Rio Grande fluvial aquifer and Santa Fe Group aquifer system. Many of the wells were nested (with negligible lateral distance between boreholes and substantial vertical variation between screen elevations; Appendix A Table 5). The nested monitor wells allow for vertical profiling at a few locations in the basin interior near the Rio Grande where unconsolidated sediments have the greatest thicknesses (Hawley and Kennedy, 2004).

^{81}Kr, ^{85}Kr, and ^{39}Ar Groundwater Sampling and Analysis

Noble gas radioisotopes can provide complementary chronometric and geochemical source and mixing information to groundwater investigations (Yokochi et al., 2013). Because noble gases are inert, corrections for geochemical processes are generally not necessary (Clark and Fritz, 1997). The low abundance and solubility of the radioisotopes of krypton and argon have required impractical sampling volumes in the past. With the advent of low-level analysis techniques such as Atom Trap Trace Analysis (ATTA; Chen et al., 1999) and Low-Level Counting (LLC; Oeschger and Wahlen, 1975), the noble gas isotopes krypton-81 (^{81}Kr), krypton-85 (^{85}Kr), and argon-39 (^{39}Ar) have become practical tracers for age-dating groundwater. The isotope ^{39}Ar is particularly valuable, as the argon system is the only isotopic system that will effectively bridge the groundwater age gap in the important intermediate range of 50 to 1,000 years (Fig. 26).

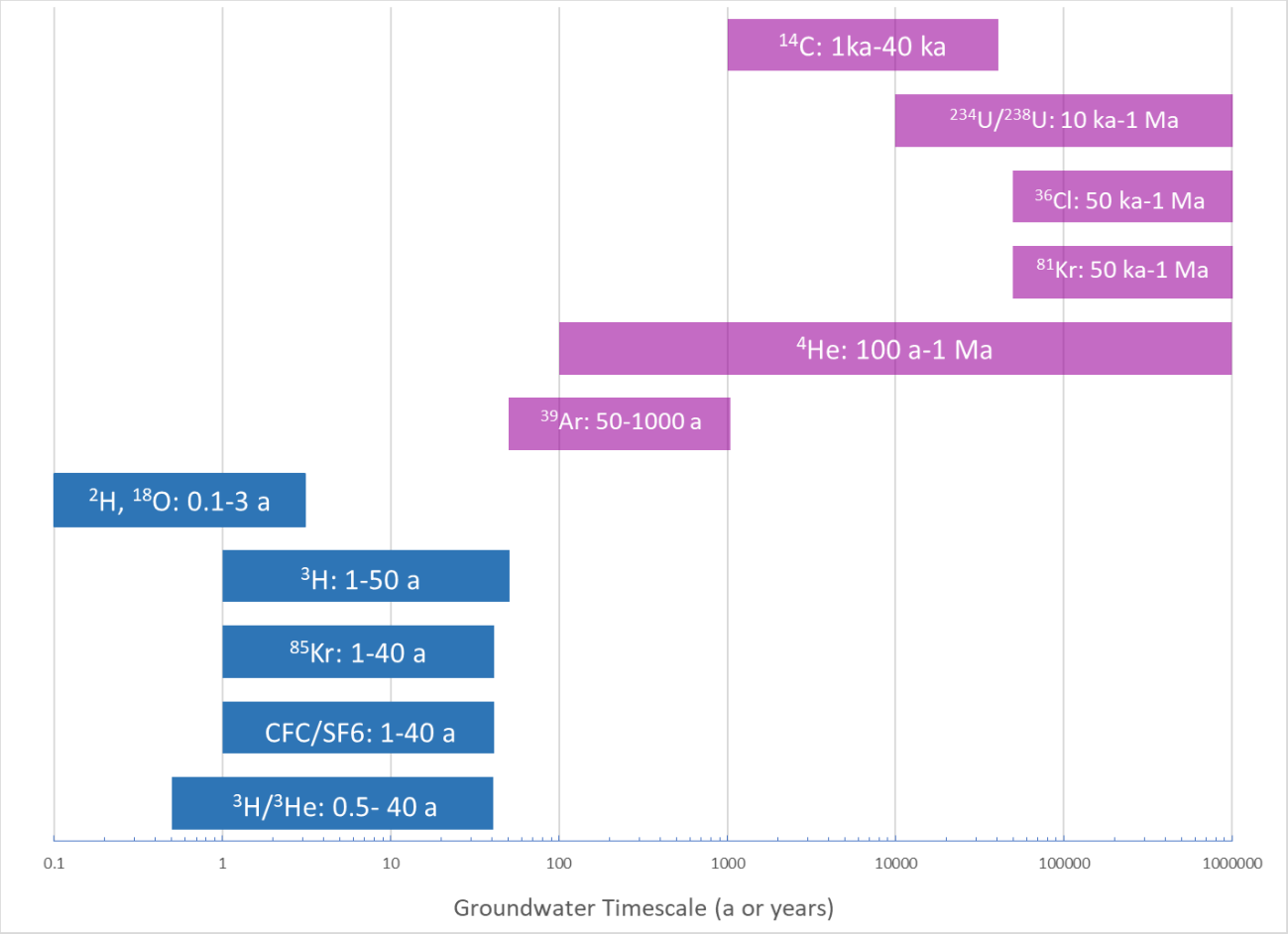

Figure 26. Isotope and chemical tracer groundwater age dating ranges (adapted from IAEA, 2013). The notation a refers to years.

Dissolved gas samples were collected from various wells and then analyzed for argon and krypton gas at Argonne National Laboratory and the Radionuclides Laboratory at the University of Bern, Switzerland. Field sample collection of dissolved gas samples is as follows: Static water level was measured prior to pumping using a Solinst depth-to-water meter or electric tape "E-Tape". Measurements were made from a documented measuring point and recorded to the nearest 0.01 ft. At least three well volumes of water were purged from the well casing to remove resident water and allow sufficient replacement of groundwater prior to sample collection. Field water-quality properties, including water temperature, pH, specific conductance, alkalinity, turbidity, and dissolved oxygen were monitored during well purging and sampling (U.S. Geological Survey, variously dated). Water quality field properties were monitored with an YSI Exo multi-parameter sonde. Groundwater was pumped using an installed pump if present, or a Grundfos portable submersible pump appropriately sized to the well dimensions. Once field properties stabilized and three well volumes of groundwater had been purged, groundwater was then pumped into a gas separation apparatus (Fig. 27). Inside the gas separation apparatus, water was pumped through two American Plumber® W5P 5µm filters, and then drawn through two Liqui-Cel® Extra-Flow 2.5 X 8 (X40) membrane contactors that separated gas by means of a 115 V Dia-

Vac® vacuum pump. Gas was then pumped into a 10.7 L N060 Luxfer Gas Cylinder fitted with a Luxfer CGA 346 valve, and compressed to a pressure between 50 and 65 psi. Once the sample cylinder had reached the appropriate pressure, the cylinder valve was closed and the cylinder was capped with a 3/4th inch brass fitting. The pump was decontaminated by placing it in a carboy with 0.1% v/v Liquinox solution and flushed with a minimum of 5 gallons of Liquinox solution. The pump was then removed from the solution, rinsed with deionized water, and then placed in a carboy with tap water and flushed with 5 gallons of tap water. Finally, the pump was rinsed and placed into a carboy with deionized water and flushed with 5 gallons of deionized water.

Dissolved gas samples were shipped to Argonne National Laboratory and the Radionuclides Laboratory at the University of Bern to be analyzed for ^{39}Ar ,^{81}Kr, and ^{85}Kr. ^{81}K and ^{85}Kr were analyzed at Argonne National Laboratory using the laser-based atom counting method known as the atom trap trace analysis (ATTA) method. ^{39}Ar and ^{85}Kr were analyzed at the University of Bern Switzerland using low level counting or LLC.

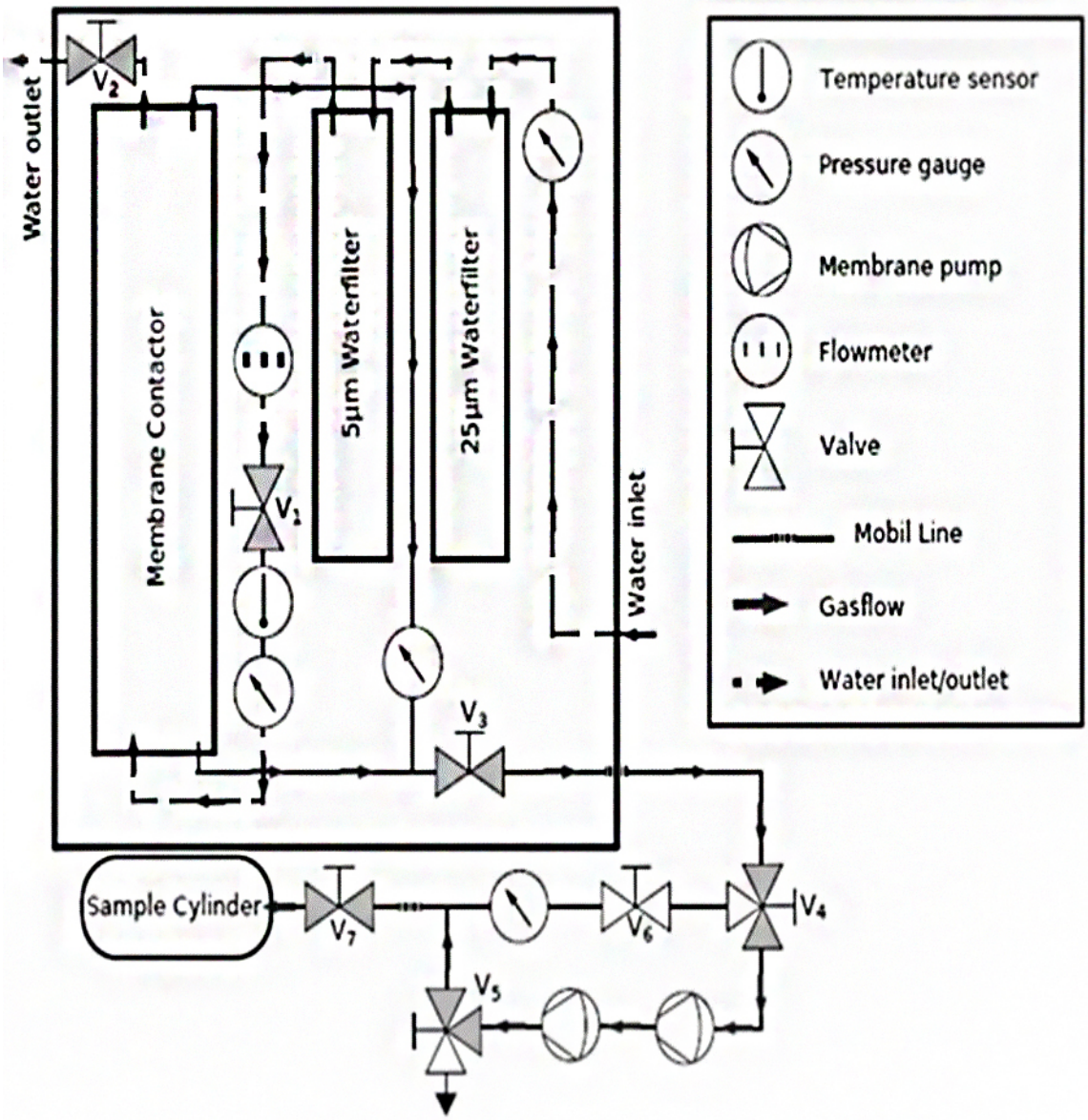

Figure 27. Schematic of dissolved gas sampling apparatus

Groundwater Sulfur Isotope Sampling and Analysis

Approaches such as the use of sulfur isotopes for distinguishing between anthropogenic and geological sources of SO_4^{2-} have been effective in identifying sources of salt in other geochemical investigations (Szynkiewcz et al., 2011; Miao et al., 2013). SO_4^{2-} is a major contributor of salt from both geological sources (e.g., gypsum ($CaSO_4$)) and fertilizers (e.g., H_2SO_4) found in irrigation waters (Szynkiewcz et al., 2011). To supplement aqueous geochemical data, we compared previously collected stable sulfate isotopes ($^{34}S/^{32}S$) of dissolved sulfate collected in 2007 by Szynkiewcz et al. (2011) to $\delta^{34}S$ of gypsum samples collected in this study (Table 10, Appendix 10.1). $\delta^{34}S$ for groundwater samples was only collected from wells in the ISC-4, ISC-7, and ISC-1 well clusters by Szynkiewcz et al. (2011; Appendix A Table 7.).

Lithologic and Geophysical Sampling and Analysis

Well Cutting Sampling and Analysis

To evaluate whether evaporite minerals were located in close proximity to well screens throughout the Mesilla Valley, seven well cutting samples were selected for XRD analysis of gypsum and halite. Two samples were selected from well cuttings of a central Mesilla Valley borehole (LMV-2), and five samples were selected from well cuttings from a southern Mesilla Valley well (ISC-4B).

To target well cuttings that were likely to test positive for halite and gypsum, individual well cuttings (bags of sediment collected for every ~3 m drilled) were analyzed for Cl, Ca, Na, and SO_4^{2-} concentrations. Microwave digestion (U.S. Environmental Protection Agency 3051A, 2007) was used to determine total Ca and Na, and a soil paste extract (Richards, 1954) was used to determine water-extractable SO_4^{2-} and Cl. Chemical analysis was completed for each well cutting between 15.2 m and 55 m below the surface in ISC-4B and every well cutting between 27 m and 80 m below the surface for the LMV-2 borehole. Well cuttings from LMV-2 and ISC-4B were selected because of water elevation maps and well drilling logs (Nickerson et al., 2006; Tetra Tech, 2004) indicating that the well cuttings selected were generally located along the same flow path in the Middle Santa Fe Group (Hawley and Kennedy, 2004; Teeple, 2017).

Analysis for total Ca and Na was completed using a Perkin Elmer Optima 4300 DV (Dual View) ICP-OES (Inductively Coupled Plasma-Optical Emission Spectrometer). Analysis for chloride concentration was completed on the Technicon AutoAnalyzer (Technicon Industrial Systems Tarrytown, New York USA). Analysis for SO_4^{2-} was completed using the Spec 20 Spectrophotometer (Thermo Spectronic Rochester, New York, USA).

Well cuttings that had total salinity concentrations (Cl+Na+SO_4+Na) greater than the 3rd quartile (75%) of all the samples were selected for XRD analysis. For ISC-4B the cuttings were 33.53 m to 36.58 m, 36.58 m to 39.62 m, 45.72 m to 48.77 m, and 48.77 m to 51.82 m below land surface. For LMV-2 the cuttings were 57.91 m to 60.96 m, and 60.96 m to 64 m below land surface.

For XRD analysis, samples were ground into a fine powder (similar to talcum powder) using a mortar and pestle and mounted onto a silicon zero-background holder. Scans were conducted with stepwise increases of 0.017° between 6°and 69° 2θ positions on a Panalytical X'Pert Pro X-Ray Diffraction diffractometer. Peak intensity and position were compared with diffractograms of gypsum and halite, the main constituents of evaporite deposits. The minimum detection for gypsum and halite was 2% by volume within the sample.

Temperature Log Sampling and Analysis

Temperature logs of unscreened or perforated wells can be used to determine the vertical rate of groundwater flow (Bredehoeft and Papadopulos, 1965; Haenel et al., 1988; Reiter, 2001; Reiter, 2005). The heat flow in the crust is usually low, so that a vertically flowing groundwater

component may systematically change the conductive temperature gradient via convective heat transport (Bredehoeft and Papadopulos, 1965). These changes in the natural temperature gradient can be observed and quantified to determine the vertical groundwater flow component as upflow (discharge) or as downflow (recharge), and also the vertical component of velocity (Fig. 28).

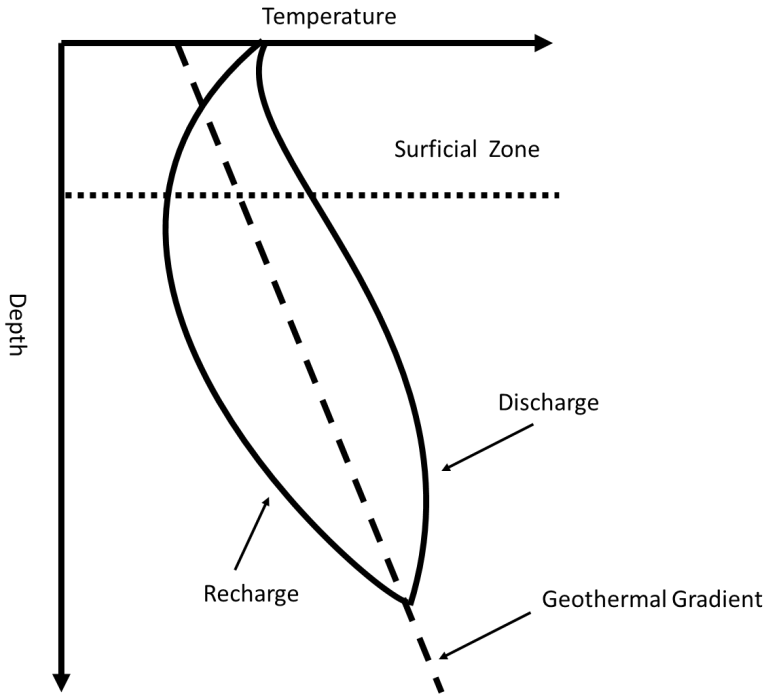

Figure 28. Temperature log schematic adapted from Anderson (2005)

In March 2018, eight temperature profiles were measured by staff and students from New Mexico Institute of Mining and Technology and NMSU from the deepest well within the various well clusters and also ISC-2A (Fig. 1). Temperature profiles were measured by lowering a thermistor to the bottom of each well. A digital multimeter and a computer were used to record resistance every meter at a 2 meters/minute rate. Resistance was then converted to temperature using a laboratory calibration derived from a platinum thermistor (Kelley et al., 2016). All wells were capped and cased and had not been pumped for at least two months prior to sampling.

Gypsum Mineral Sulfur Isotope Sampling and Analysis

To constrain geologic endmembers of groundwater $\delta^{34}S$, $\delta^{34}S$ of gypsum was analyzed from various rock formations in southern New Mexico. Gypsum samples were collected from an outcrop of the Mesilla Valley Shale at Cerro de Cristo Rey, a roadcut of the Rincon Valley Formation near Rincon, New Mexico and Lake Lucero of White Sands, New Mexico (Appendix A Table 10.). Gypsum samples were ground to a fine powder using a mortar and pestle and then poured into 250 mL – 450 mL of deionized water to dissolve. Solutions were stirred on low heat for five hours and then decanted into 1L high density polyethylene bottles. Once prepared, solutions were filtered and precipitated into ~1 g samples of $BaSO_4$ using methods outlined in Szynkiewicz and others (2011; Table 1). Analysis for $\delta^{34}S$ was completed using methods outlined in Kelly and others (2018) at Isotech Laboratories.

Data Analysis

Isometric Log Ratio Analysis

Conservative ions such as Cl^-, Br^-, B^-, and Li^+ are highly soluble, biologically inert, and do not easily adsorb onto clays (Clark and Fritz, 1997). For these reasons, Cl^-, Br^-, and Na^+ ratios are common diagnostic tools for determining sources of salinity in sedimentary basins (Clark and Fritz, 1997). Common geological sources of solutes include: gypsum dissolution ($CaSO_4{:}2H_2O$), halite dissolution (NaCl), and weathering of feldspars and amphiboles (contributing Na^+, K^+, Ca^{2+}, Mg^{2+}, and SiO_2; Witcher et al., 2004). If Ca^{2+} concentrations in groundwater increase significantly enough, calcite ($CaCO_3$) will precipitate, and buffer Ca^{2+} concentrations in groundwater (Witcher et al., 2004).

Despite the widespread use of elemental concentration plots (Cl:Br) and elemental ratio plots (Cl/Br:Na/Br), these comparisons have been shown to result in spurious mathematical relationships because of the lack of independence among variables (Engle and Rowan, 2012). For example, increasing the chloride concentration in groundwater will increase the solubility of other ions, resulting in mixing relationships that may be unrealistic; these issues are exacerbated in high salinity waters (Engle and Rowan, 2012; Engle et al., 2016). Engle and Rowan (2012) suggest adjusting molar concentration data using isometric log ratios, which can avoid the numerical issues associated with traditional methods.

In isometric log ratio plots, concentrations are equally weighed within a coordinate system. For example, when plotting Na/Cl on an X axis using an isometric log ratio, a 1:1 ratio of Na/Cl would plot at zero. A Na/Cl ratio greater than one would plot positively and a Na/Cl ratio less than one would plot negatively, such that each direction in the coordinate is equally weighed. This allows for a better understanding of the balance between ions. For comparison, an elemental ratio plot of Na/Cl on an X axis has the following properties: an even ratio of Na/Cl is equal to 1, Na/Cl ratios greater than one are given an infinite amount of space to occupy, but Na/Cl ratios less than one 1 can only occupy space on the X coordinate between 1 and zero. The skew of the elemental concentration ratio grid can easily result in misinterpretation of data (Engle and Rowan, 2012).

Isometric log ratio balances were developed using sequential binary partitions. Sequential binary partitions are series of non-overlapping groups of parts (Engle, 2016). Once concentrations are converted into isometric log ratios, they can be interpreted with standard Euclidean geometry (Engle et al., 2016). Previously reported balances were used to interpret halite (NaCl) and gypsum ($CaSO_4$) dissolution in high salinity groundwaters (Engle and Rowan, 2012; Engle et al., 2016).

Geochemical Modeling Analysis and Mapping

The geochemical software PHREEQC, version 3.3.12 (Parkhurst and Appelo, 2013), was used to calculate saturation indices for a selected mineral that is a relative comparison to the thermodynamic dissolve precipitation equilibrium between water solutions and solid minerals. A

positive saturation index indicates oversaturation that leads to precipitation; a negative value indicates undersaturation, which indicates potential for dissolution of the mineral, and a value of zero marks equilibrium between water and a mineral (Parkhurst and Appelo, 2013). Water sample chemistry from all wells was input into the program with common rock forming minerals selected for comparison.

A previously published data set from Hiebing and others (2018) was used to create a total dissolved solids contour map using the program Surfer® 14 from Golden Software, LLC (www.goldensoftware.com). Kriging was used to contour maximum TDS for each point location. Faults and dikes reported in Sweetkind (2017) were overlaid onto the map using the program QGIS (QGIS, 2015).

Corrections for ^{14}C ages of groundwater are often necessary (Clark and Fritz, 1997). Processes that can affect ^{14}C ages include calcite dissolution, dolomite dissolution, exchange with the aquifer matrix, oxidation of organics, and diffusion of ^{14}C into the aquifer matrix (Clark and Fritz, 1997). $\delta^{13}C$ has been shown to be an effective tracer for determining how open or closed a system is along a groundwater flow path (Clark and Fritz, 1997). When a system is open, exchange with the atmosphere occurs, resulting in young ^{14}C ages and $\delta^{13}C$ comparable to soil CO_2. When a system is closed, ^{14}C ages will be older and the degree of carbonate dissolution may be determined by how closely groundwater $\delta^{13}C$ signatures resemble carbonates in the subsurface and the molality of dissolved carbonate species in groundwater. To correct for carbonate dissolution, the predominant cause of shifted ^{14}C ages in most aquifers, a revised Fontes and Garnier model was used (Clark and Fritz, 1997; Han and Plummer, 2013). This simplified model requires inputs for $\delta^{13}C$ of both soil and carbonates in the subsurface. Input parameters for $\delta^{13}C$ of soil CO_2 was -20 and -2.73 per mil for calcite/carbonates; these values were based off of $\delta^{13}C$ values reported by Witcher and others (2004) of southern New Mexico calcite/carbonate (-2.2 to -5.5 per mil) and soil gas (-15.7 to -25 per mil). The assigned pMC (percent modern carbon) of soil CO_2 was 100 and 0 for calcite/carbonate; these values are commonly used to represent the transition between an open and closed system in most aquifers (Han and Plummer, 2013). Required inputs for estimating the corrected ^{14}C age of a groundwater sample are molality of carbonate species, observed ^{14}C concentration, $\delta^{13}C$ signature, and temperature. Model corrections were only applied to groundwaters with an initial concentration of less than 50 pMC; groundwaters with concentrations less than 50 pMC are assumed to exist in a closed system where $\delta^{13}C$ signatures of groundwater are dictated solely by reactions between calcite and soil CO_2 (Han and Plummer, 2013). Additionally, corrections for groundwater in the unsaturated zone would likely be inaccurate due to influences from surface caliche layers that are enriched in $\delta^{13}C$ (-0.6 to -11 per mil; Witcher et al., 2004). The revised Fontes and Garnier model has been used in other southwestern basins with success (Hagedorn, 2015).